Spin-Polarized Transport and Spin Filtering in Organic Nanostructures

by

Kazi Mohammad Monirul Alam

A thesis submitted in partial fulfillment of the requirements for the degree of

Doctor of Philosophy

in

Micro-Electro-Mechanical Systems (MEMS) and Nanosystems

Department of Electrical and Computer Engineering
University of Alberta

Abstract

Electrons, the fundamental charge carriers in solid-state devices, possess three intrinsic properties: mass, charge and spin. Spin is a quantum mechanical property, but can be loosely visualized as a tiny "intrinsic" magnetic dipole moment attached to an electron. In conventional electron devices, spin magnetic moments point along random directions in space and play no significant role in device operation. In the emerging field of "spintronics" the central theme is to harness the spin degree of freedom of charge carriers to realize novel data storage and information processing technologies. Spintronic devices are already ubiquitous in state-of-the-art hard disks with large storage densities. A concerted global effort is underway to explore various spin-based information processing concepts, which can potentially be more energy-efficient than traditional charge-based electronics.

In recent years, substantial research has been devoted to understanding carrier spin dynamics in metallic multilayers, tunnel junctions and inorganic semiconductors such as silicon, germanium and various III-V compounds. On the other hand, π-conjugated organic semiconductors that play a crucial role in organic electronics and displays are relatively new materials in the area of spintronics. Organic semiconductors offer several advantages (such as mechanical flexibility, chemical tunability of physical properties, low-cost and low-temperature processing) compared to their inorganic counterparts. The ability to control carrier spin dynamics in organic materials will open up possibility of new devices such as flexible non-volatile memories, spin-based organic light emitting diodes and spin filters.

In this work, we have explored two key spin related phenomena in organic semiconductor nanostructures: (a) spin-polarized transport and (b) spin filtering. In the first sub-project, we explore spin transport in “nanowire” geometry instead of commonly studied thin film devices. Such experiments shed light on the spin relaxation mechanisms in organics and indicate ways to minimize such effects. Fabrication of organic nanowires with well-controlled geometry in the sub-100 nm range is a non-trivial task, and in this subproject we have developed a novel technique for this purpose. Spin transport in rubrene nanowires has been studied, which indicates significant suppression of spin relaxation in nanowire geometry compared to rubrene thin films. Our experimental data indicates that spin-orbit coupling is the dominant spin relaxation mechanism in rubrene nanowires. In the second sub-project, we explore spin filtering (transmission of one particular type of spin) through an organic nanostructure in which single wall carbon nanotubes (SWCNT) are wrapped with single stranded DNA (ssDNA) molecules. Efficient spin filtering has been observed in this system, which may enable magnetless spintronic devices in the future.

Acknowledgements

I would like to express my deep gratefulness to my thesis advisor, Prof. Dr. Sandipan Pramanik who made the whole work possible. His stimulating suggestions and encouragement helped me throughout my research and writing of this thesis. My experience of working as a student of Prof. Sandipan Pramanik is an invaluable treasure, which will benefit my entire life. I also would like to extend my thanks to my supervisory committee members, Dr. Steve Dew and Dr. Vien Van, for their advice and opinions. I am thankful to TRTech and NSERC (Natural Sciences and Engineering Research Council), Canada for support and the entire Electrical and Computer Engineering department for providing an excellent work environment.

It was my pleasure to work with my research group members; Srikrishna, Abhay, and Ryan who have given help and valuable hints. I particularly enjoyed our group meetings. My stay in University of Alberta was peaceful and interesting. I found the departmental activities very conducive to gain knowledge and build up social networks.

Finally, I would like to be thankful to my family members whose continuous support and encouragement helped complete this work.

Table of Contents

List of Tables

List of Figures

Chapter 1[*]

Introduction.

1.1 Spintronics: General Overview.

Solid-state electronics has played a key role in shaping today's information-based society. What lies in the heart of this information technology revolution is the ability to process and store binary information using solid-state devices. These functions are often implemented by manipulating the charge degree of freedom of carriers (electrons and holes) in solid-state systems. For example, realization of the classical binary logic bits ("0" and "1") requires two physically distinguishable states. In computer memories, such states are realized by different amounts of charge stored on a capacitor (dynamic random access memory or DRAM) or by two distinct voltage levels at some circuit node (static random access memory or SRAM). Processing of charge-based logic bits is performed by circuits comprised of switching devices such as transistors. An emerging technology named "spintronics" [2], [3] or "spin-based electronics", on the other hand, aims to harness the spin degree of freedom of carriers in lieu of charge to realize these core data storage and information processing functionalities [4]–[7]. This technology offers unprecedented data storage density and immense potential for realizing "universal memory" and energy-efficient computing as described below.

1.1.1 Spintronics in Data Storage.

The discovery of the giant magnetoresistance (GMR) effect in the late 1980s [8], [9] is the first major milestone in the history of spintronics [10], [11] and has revolutionized the data-storage industry. The GMR effect, observed in ferromagnetic/nonmagnetic metallic multilayers, offers an efficient and scalable method of sensing very weak magnetic fields. This has enabled significant reduction of bit size on hard discs without sacrificing the quality of signal detection. This development has also resulted in hard drives of smaller form factors, which are now ubiquitous in virtually all mobile appliances such as ultra-light netbooks, portable multimedia players, digital cameras and camcorders.

---

[*] Parts of this chapter have been published in ref. [1].

Spintronic memory (magnetic random access memory or MRAM) chips [12] are emerging as a strong contender in the race for "universal memory" [13], which aims to achieve high bit density, fast access speed, non-volatility and durability at a low cost. The primitive memory cell (also known as the "magnetic tunnel junction" or MTJ) consists of a tunnel barrier of aluminum oxide [14] or magnesium oxide [15] separating two ferromagnetic electrodes. The tunneling current is "spin-polarized" due to the ferromagnetic electrodes. The tunneling probability (and hence the tunneling current) is spin-dependent, and can be controlled by the relative magnetization orientations of the ferromagnetic electrodes. Thus the MTJ cell can be in either of two well-separated states ("high-resistance" or "low-resistance"), which can therefore be utilized to encode binary data. This method of storage is nonvolatile since the resistance depends on the relative magnetization orientations of the contacts, which remain unaffected when the power is switched off. In this respect, MRAMs are similar to flash memories but offer superior read-write speed and endurance. Apart from memory cells, MTJs are also finding application in developing logic gates [16].

1.1.2 Spintronics in Information Processing.

The application of spintronics in the realm of information processing is a relatively new endeavor and is motivated by the belief that spintronics may offer a more power-efficient route compared to the traditional transistor-based paradigm [17]. Since the inception of silicon-based integrated circuits ("chips") over four decades ago, the integration density of transistors on a chip has roughly doubled in every 18 months with concomitant increase in clock speed and computational prowess. This trend, commonly referred to as Moore's law, has been sustained by the combined effect of classical Dennard scaling [18] of transistors and gradual introduction of non-traditional materials (e.g. high κ dielectric, metal gate) in the fabrication process [19]. A fundamental problem associated with the device shrinkage is the issue of power dissipation [5], [20]. This constitutes the so-called "Red Brick Wall" [21] on the International Technology Roadmap for Semiconductors (ITRS) and calls for ingenious designs to reduce power dissipation. This is where spintronics is expected to offer a solution. Spintronic information processing can be achieved in three conceptually different ways:

(*a*) Classical information processing using a monolithic [22] (or "all-spin") approach [5], (*b*) Classical information processing using a hybrid [22] (or “charge *augmented with* spin”) approach and

(*c*) Quantum information processing using spin qubits [23].

In the monolithic approach [22], charge does not play any direct role in information coding and processing. These tasks are performed by spins. The single spin logic (SSL) paradigm [4], [22] is an example of this monolithic approach and utilizes the fact that in the presence of an external magnetic field, an electron spin can either be parallel (“upspin”) or antiparallel (“downspin”) to the magnetic field. This bistable nature of spin is exploited to encode classical logic bits “0” and “1”. Processing of this information is performed by applying a local magnetic field and controlling spin-spin interactions. Since this paradigm employs stationary charges and does not involve any physical movement of charge carriers (and hence no current), it eliminates the I^2R type dissipation that accompanies every MOSFET with channel resistance R carrying a current of I during switching. Still, a finite amount of energy is dissipated during the bit (spin) flip, but this is significantly smaller compared to the MOSFETs [4], [22]. Similar proposals have been made which encode logic bits in the magnetizations of nanomagnets i.e. binary data is now encoded by a collection of spins instead of a single spin [24], [25]. Here spin manipulation is performed via spin torque effect [24] or local magnetic fields [25]. By suitable design, power dissipation associated with a bit (magnetization) flip can be reduced to only few k_BT [24].

In the so-called “hybrid” approach [22] the goal is to realize transistor switches in which the device current is turned on and off by controlling the spin orientations of the charge carriers in the channel. The logic operation is otherwise the same as the classical charge-based schemes. The first proposal of such device was made in ref. [26]. Since then, many spin transistor models have been proposed [4]. Experimental progress in this area has been slow due to poor spin injection efficiency and lack of efficient gate control of channel spin polarization.

Finally, the third approach proposes to use spin as a quantum bit (qubit) instead of a classical bit as in the single spin logic approach. Spin qubits can be manipulated by an external ac magnetic field of specified duration. Universal logic operations can be performed by appropriate choice of the external magnetic field. Such computational schemes, commonly known as "quantum computation", in theory offer immense computational prowess and zero energy dissipation [27].

1.2 Key Elements of Spintronics.

The basic elements of spintronics are (a) spin injection, (b) transport of injected spins and associated spin relaxation and finally (c) spin detection. While extensively studied in the context of technologically important inorganic semiconductors such as Si, Ge and III-V compounds [28], these phenomena are still relatively poorly understood in organic semiconductors [1]. In this section we briefly discuss these key processes, which are closely related to this thesis.

1.2.1 Spin Injection.

Creation of a non-equilibrium population of spin-polarized charge carriers within an otherwise nonmagnetic material is generally termed as "spin injection". There exist different methods such as optical or electrical spin injections [28] that create this non-equilibrium population of spins. In case of organics, due to their inherently weak spin-orbit coupling, the optical method is not a viable route for spin injection. Therefore, we will restrict the discussion of this phenomenon to the electrical case only.

In an all-electrical spin transport experiment, spin injection is achieved by using ferromagnetic (transition metals, half-metals or dilute magnetic semiconductors) contacts, commonly described as "spin injectors". In ferromagnets, the carriers at the Fermi level are spin-polarized (in ideal half-metals, they are 100% spin polarized). Therefore, carriers injected from a ferromagnet to a nonmagnet are expected to be spin-polarized as well. This is the basis of electrical spin injection and is illustrated in Figure 1.1 [1]. The nonmagnet can be a metal or a semiconductor. The carriers' ensemble density of states (DOS) spin polarization (P_{DOS}) can be defined as,

$$P_{\mathrm{DOS}} = (N_1 - N_2)/(N_1 + N_2) \qquad (1)$$

where N_1 and N_2 are the density of states at the Fermi level of carriers with spin magnetic moments parallel and antiparallel to the magnetization of the ferromagnet, respectively.

1.2.2 Spin Transport and Spin Relaxation.

In a typical spintronic device, after injection, the spin polarized carriers travel through the nonmagnetic material under the influence of a transport-driving electric field. During their transit, different spins interact with their environments differently (spin-orbit, hyperfine and carrier-carrier interactions) and their original orientations get changed by various amounts. Thus the magnitude (*P*) of the ensemble spin polarization decreases with time (*t*) as well as with distance (*x*) measured from the injection point.

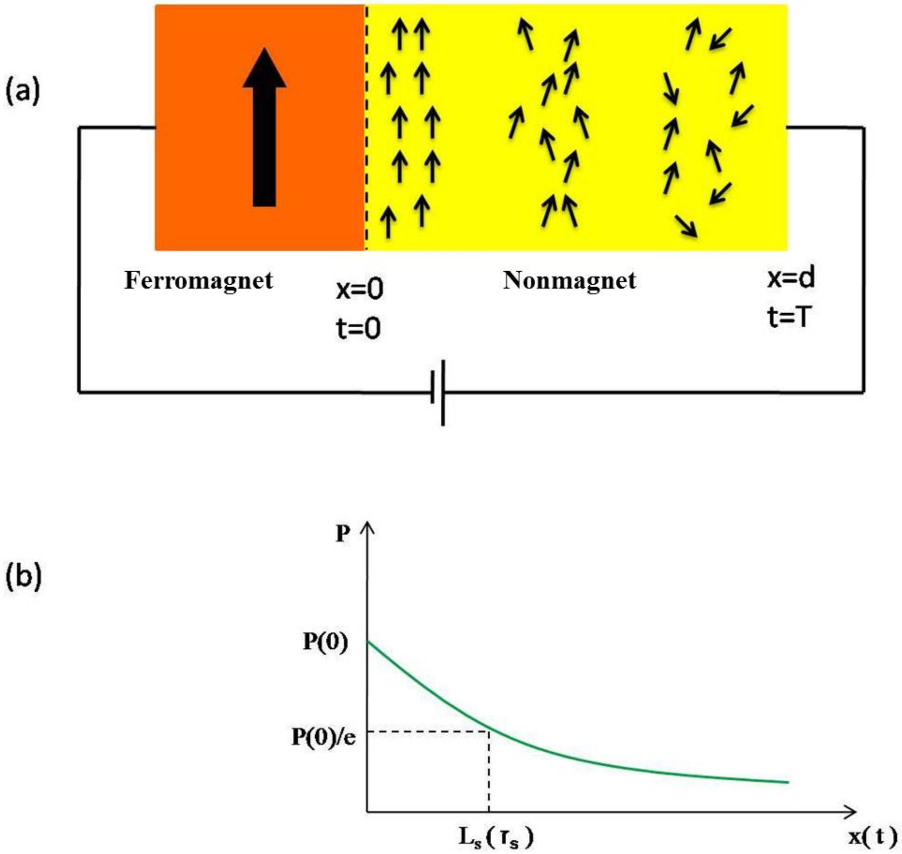

Figure 1.1 Illustration of electrical spin injection (a) and spin relaxation (b). The magnitude of the ensemble spin polarization decreases with time and distance implying spin relaxation.

This gradual loss in magnitude of the injected spin polarization is termed spin relaxation. Assuming an exponential decay, spin relaxation (or diffusion) length L_S (or spin relaxation/diffusion time τ_S) is defined as the distance (duration) over which the spin polarization reduces to 1/*e* times its initial value. For $L >> L_S$ (or $t >> \tau_S$), $P \approx 0$, implying a complete loss of spin polarization. In other words, spin relaxation phenomena in the nonmagnet tends to bring the non-equilibrium spin polarization back to an equilibrium unpolarized state. In spintronics, since the underlying philosophy is to exploit the non-zero spin polarization, one always attempts to suppress spin relaxation *i.e*. enhance spin relaxation length and time in the nonmagnetic material. We note that if the spins of all carriers change in unison, then the magnitude of the ensemble spin polarization will remain the same but its orientation will change. In this case, spin relaxation is suppressed.

There are several mechanisms in solid that are responsible for spin relaxation [22], [29] such as (*a*) Elliott-Yafet, (*b*) D'yakonov-Perel', (*c*) Bir-Aronov-Pikus and (*d*) hyperfine interaction with nuclei [28], [29]. Among these, the first two mechanisms originate from spin-orbit interaction. The third one originates from coupling between electron and hole spins, and the last one is due to interaction between carrier spins and nuclear spins. It is not clear which of these mechanisms plays the most dominant role in organic semiconductors. We briefly discuss these processes in the following paragraphs.

(a) *Elliott-Yafet Mechanism*: In the presence of spin-orbit coupling, Bloch states of a real crystal are not pure spin-up or spin-down (with respect to some fixed spin quantization axis) states. Instead, they can be represented as an admixture of both spin-up and spin-down states. The degree of admixture is a function of the electronic wave vector. As a result, when a momentum relaxing scattering event causes a transition between two states with different wave vectors, it will also reorient the spin and contribute to spin relaxation. This is the basis of the Elliott-Yafet mode [28], [30] of spin relaxation [Figure 1.2 (a)] [1].

(b) *D'yakonov-Perel' Mechanism*: The D'yakonov-Perel' mechanism of spin relaxation is dominant in systems which lack inversion symmetry. Examples of such (inorganic) solids are III-V semiconductors (e.g. GaAs) or II-VI semiconductors (e.g. ZnSe) where inversion symmetry is broken by the presence of two distinct atoms in the Bravais lattice. Such kind of asymmetry is known as bulk inversion asymmetry [22]. In a disordered organic semiconductor, bulk inversion symmetry is absent. Inversion symmetry can also be broken by an external or built-in electric field, which makes the conduction band energy profile inversion asymmetric along the direction of the electric field. Such asymmetry is called structural inversion asymmetry. In a disordered organic semiconductor, structural inversion asymmetry typically arises from microscopic electric fields due to charged impurities and surface states (e.g. dangling molecular bonds). Both types of asymmetries result in effective electrostatic potential gradients (or electric fields) that a charge carrier experiences. In the rest frame of a moving carrier, this electric field Lorentz transforms to an effective magnetic field B_{eff} whose strength depends on the carrier's velocity v. A carrier's spin in an inversion asymmetric solid undergoes continuous Larmor precession about B_{eff} between two consecutive scattering events. Since the magnitude of B_{eff} is proportional to the magnitude of carrier velocity v, it is different for different carriers. Thus, collisions randomize B_{eff} and therefore the orientations of the precessing spins. As a result, the ensemble averaged spin polarization decays with time. This is the D'yakonov-Perel' mode [28], [31] of spin relaxation [Figure 1.2 (b)].

(c) *Bir-Aronov-Pikus Mechanism*: The Bir-Aronov-Pikus mechanism of spin relaxation is dominant in bipolar semiconductors. The exchange interaction between electrons and holes is described by the Hamiltonian $H = AS.J\,\delta(r)$, where A is proportional to the exchange integral between the conduction and valence states, J is the angular momentum operator for holes, S is the electron spin operator and r is the relative position of the electron and the hole. Now, if the hole spin flips (owing to strong spin-orbit interaction in the valence band), then electron-hole coupling will make the electron spin flip as well, resulting in spin-relaxation of electrons [28], [32].

(d) *Hyperfine Mechanism*: Hyperfine interaction is the magnetic interaction between the spin magnetic moments of the electrons and the nuclei. This is the dominant spin relaxation mechanism for quasi-static carriers, i.e. when carriers are strongly localized in space and have no resultant momentum [28], [33]. In that case, they are virtually immune to Elliott-Yafet or D'yakonov-Perel' relaxations since these, as discussed above, require carrier motion. We can view the hyperfine mechanism as caused by an effective hyperfine magnetic field (B_{H}), created by an ensemble of nuclear spins, which interacts with electron spins and results in dephasing [Figure 1.2 (c)].

As mentioned before, spin relaxation is detrimental to the operation of any spintronic device, and hence extensive care must be taken to minimize such effects. The active region of the device must be smaller than the spin relaxation length in order to observe any spin-related effect. During transport of spin-polarized charge carriers, their spin orientations can be changed controllably (assuming the absence of any spin relaxation events) by external gate electric fields via spin-orbit interactions. Such schemes are the basis of many spintronic devices including the celebrated spin field effect transistor (spin-FET) [26].

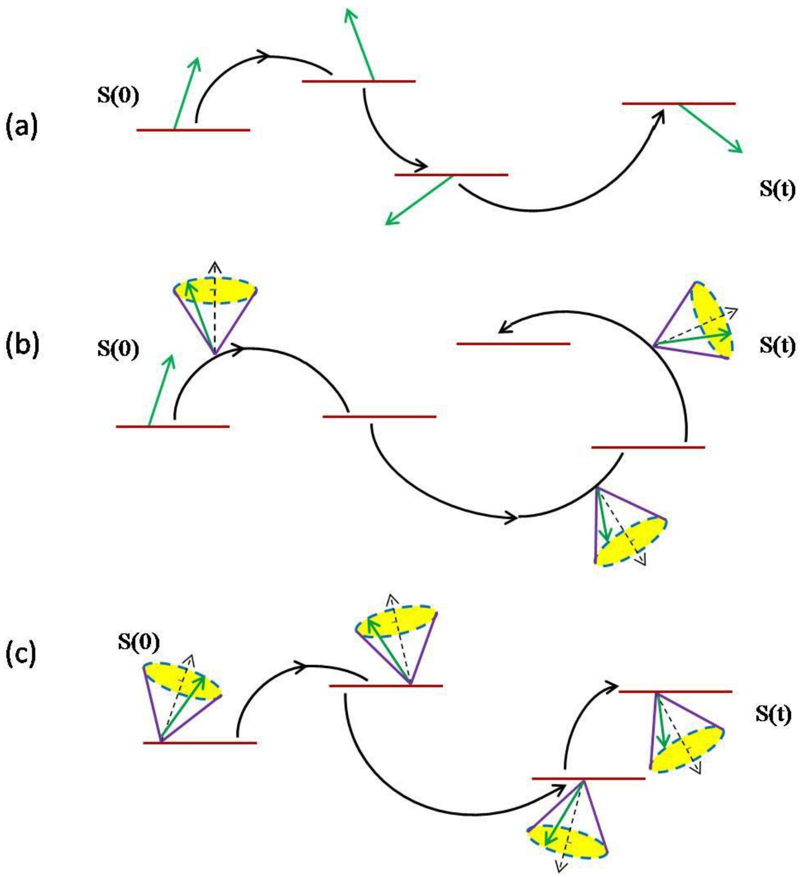

Figure 1.2 Schematic description of various spin relaxation mechanisms in the context of organic semiconductors. Carrier hopping between localized states has been shown. Spin relaxation via (a) Elliott-Yafet, (b) D'yakonov-Perel' and (c) Hyperfine interaction.

1.2.3 Spin Detection.

Spin detection is essentially the inverse of spin injection process. Ferromagnets can be used as "electrical" spin detectors since they offer different transmission probabilities to different spin polarizations. Device resistance depends on the relative angle between carrier spin polarization and the magnetization of the ferromagnetic detector.

1.2.4 Spin Valve Experiment.

Spin relaxation length (L_S) and spin relaxation time (τ_S) in a nonmagnetic material can be extracted by performing a spin-valve experiment. A spin-valve is a trilayered construct, in which the nonmagnetic material of interest is sandwiched between two ferromagnetic electrodes of different coercivities [Figure 1.3] [1]. Unlike giant magnetoresistive devices, these ferromagnets are not magnetically coupled with each other. As a result, their magnetizations can be independently switched by a global magnetic field. One of these ferromagnets acts as an "electrical" spin injector *i.e.* under an applied electrical bias it injects spins (from the quasi-Fermi level) into the nonmagnet. Electrical spin injection from a ferromagnet has been discussed before in section 1.2.1. The second ferromagnet also provides unequal spin-up and spin-down DOS at the (quasi) Fermi level and preferentially transmits spins of one particular orientation. For the simplicity of discussion, let us assume that the detector ferromagnet transmits (blocks) completely the spins that are parallel to its own majority (minority) spins or the magnetization of the detector. The transmission probability (T) of an electron through the detector is then proportional to $\cos^2\theta/2$ where θ is the angle between the spin orientation of the electron arriving at the detector interface and the magnetization of the detector ferromagnet [4]. This means that if (*a*) the magnetizations of the ferromagnets are parallel, (*b*) the injector injects majority spins and (*c*) there is no spin flip or spin relaxation in the spacer or the interfaces, the transmission coefficient should be unity (since $\theta = 0$) which will result in a small device resistance. Similarly, when the magnetizations are antiparallel (and other two conditions remain same as before), the transmission coefficient should be zero (since $\theta = \pi$), and in this case one should observe large device resistance. In a real device, there is always some spread in the value of θ since both majority and minority spins are injected, and different electrons undergo different degrees of spin relaxation before arriving at the detector interface. This makes θ different for different electrons. As a result, ensemble averaging over all the electrons makes the resistance finite even when the magnetizations of the two ferromagnetic contacts are antiparallel. Nonetheless, if the length of the nonmagnetic spacer is smaller than the spin relaxation length, then the resistance is measurably larger when the contacts are in antiparallel orientation than when they are in parallel orientation.

From the above discussion it follows that, if one of the ferromagnets preferentially transmits (either injects or detects) minority spins, then resistance of the spin valve will be large (small) in a parallel (antiparallel) configuration. This is sometimes referred to as the "inverse spin valve" effect. In a spin-valve experiment, resistance of the device is measured as a function of the applied magnetic field (H). The change in resistance between the parallel and antiparallel configurations allows one to extract the spin relaxation length (L_S) and time (τ_S) in the nonmagnetic spacer. For the following discussion, we will assume a regular spin valve effect i.e. low (high) resistance in the parallel (antiparallel) configuration. We will also assume that the coercive fields of the two ferromagnets (spin injector and detector) are given by $|H_1|$ and $|H_2|$ with $|H_1| < |H_2|$.

First, the spin valve device shown in Figure 1.3 is subjected to a strong saturating magnetic field (say $|H_{sat}| >> |H_2|$) which magnetizes both the ferromagnets along the direction of the field. In this case, the resistance of this device is R_P where the subscript (P) indicates "parallel" magnetization configuration. Next, the field is decreased, swept through zero and reversed. At this stage, when the magnetic field strength (H) just exceeds $|H_1|$ in the reverse direction (i.e. $-|H_2| < H < |H_1|$), the ferromagnet with the lower coercivity (i.e. $|H_1|$) flips magnetization. Now the two ferromagnetic contacts have their magnetizations antiparallel to each other and the device resistance is R_{AP} where the subscript (AP) indicates "antiparallel" magnetization configuration. For a regular spin valve effect as described above, at $H = -|H_1|$ a jump (increase) in the device resistance should occur due to a decrease in spin-dependent transmission probability. As the magnetic field is made stronger in the same (i.e. reverse) direction, the coercive field of the second ferromagnet will be reached ($H = -|H_2|$). At this point the second ferromagnet also flips its magnetization direction, which once again places the two ferromagnets in a configuration where their magnetizations are parallel. Thus, the resistance drops again to R_P at $H = -|H_2|$. Therefore, during a single scan of magnetic field from H_{sat} to $-H_{sat}$, a spin valve device shows a resistance peak between the coercive fields of the two ferromagnets (i.e. between $-|H_1|$ and $-|H_2|$). Similarly if the magnetic field is varied from $-H_{sat}$ to H_{sat}, an identical peak will be observed between $|H_1|$ and $|H_2|$. The spin-valve response is pictorially explained in Figure 1.4 [1]. The relative change in device resistance between the parallel and antiparallel configurations is the signature of spin injection, transport and detection and is quantified by the "spin valve magnetoresistance ratio", $\Delta R/R = (R_{AP} - R_P) / R_P$.

For the special case when the spacer is a tunnel barrier, this ratio is expressed by the famous Julliere formula [34],

$$\frac{\Delta R}{R} = \frac{R_{\mathrm{AP}} - R_{\mathrm{P}}}{R_{\mathrm{P}}} = \frac{2P_1P_2}{1-P_1P_2} \tag{2}$$

where P_1 and P_2 are the spin polarizations of the density-of-states (DOS) at the Fermi level of the two ferromagnetic electrodes. Julliere's model assumes (a) spins are conserved (no spin reorientation/flip occurs) during tunneling and therefore tunneling of up and down spin electrons can be viewed as two independent processes and (b) tunneling probability is spin independent and conductance for a particular spin species (up/down) is solely determined by the appropriate density of states at the two ferromagnets. The quantities P_1 and P_2 are often equated to the spin polarizations of the tunneling current which are independently determined via Meservey-Tedrow experiments using an alumina tunnel barrier [35]. It is to be noted that the spin polarization of the tunnel current not only depends on the DOS, but also depends on tunnel probability which is barrier-dependent and may be different for different electronic states in the ferromagnet. The importance of the barrier has been shown in ref. [36]. According to this report, Co exhibits a negative spin polarization of tunneling electrons for SrTiO3 barriers but a positive spin polarization for alumina barriers.

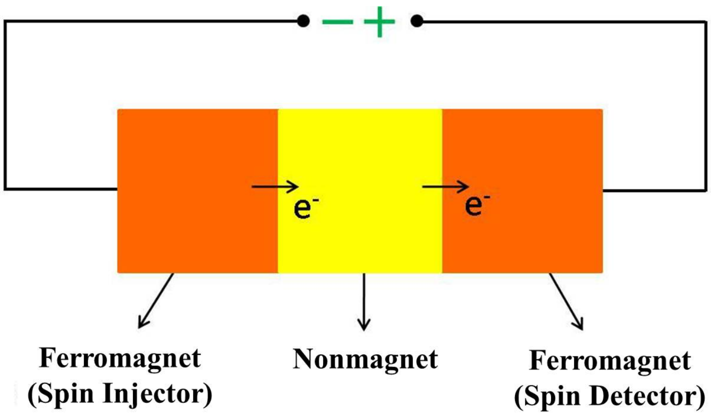

Figure 1.3 Schematic depiction of a spin valve. The spin valve is a trilayered structure where the nonmagnetic spacer material is sandwiched between two ferromagnets of different coercivities. One of the ferromagnets acts as a spin injector and the other one acts as the spin detector.

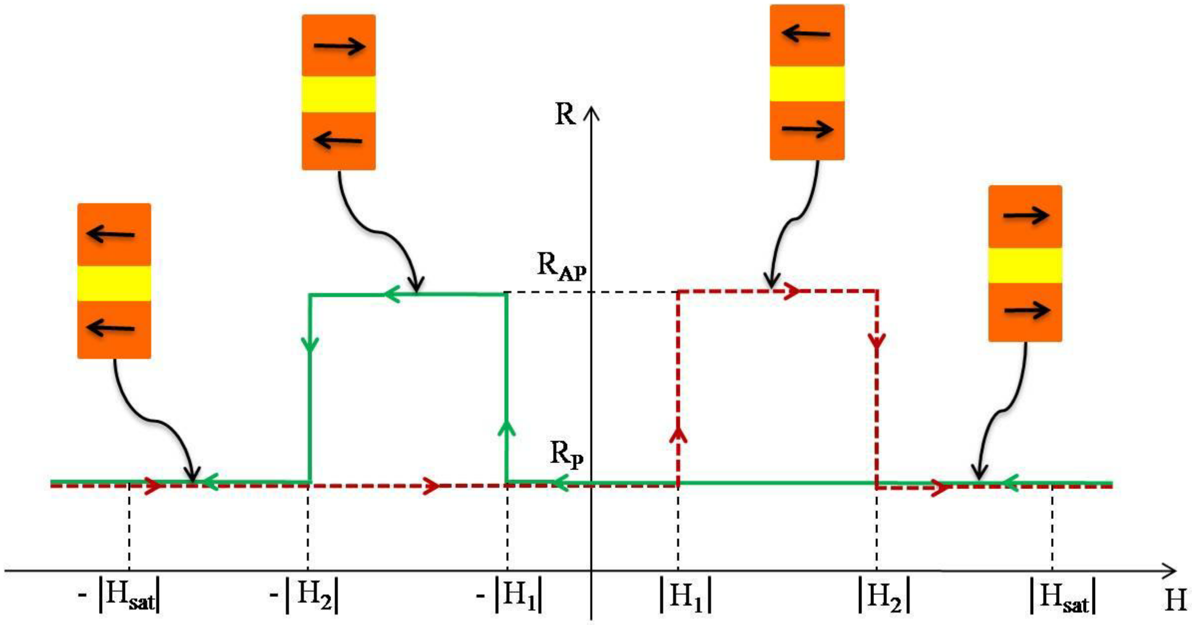

Figure 1.4 Pictorial representation of a spin valve response. The coercivities of the two ferromagnets are |H_1| and |H_2|. This is an example of the positive (or normal) spin valve effect since resistance corresponding to antiparallel (AP) magnetization is higher than that of parallel (P) configuration.

Julliere's formula can be extended for thicker nonmagnetic spacers in which spin transport occurs via drift-diffusion (crystalline solids) or multiple hopping (disordered solids) instead of direct tunneling between the contacts. However, the injector and detector interfaces are assumed to have a tunneling (Schottky) barrier, which occurs in many metal/semiconductor interfaces. In this situation, spin polarized electrons are injected via the tunnel barrier into the nonmagnet. Let us assume that the spin polarization of the injected carriers is P_1, which can be determined exactly by the Meservey-Tedrow technique. Once in the nonmagnet, these carriers will drift and diffuse (or hop) towards the detector contact, under the influence of a transport-driving electric field. The spin polarization of the injected carriers (P) decreases with distance (measured from the injection point) due to various spin relaxing processes. Assuming an exponential decay, spin relaxation process can be modeled as

$$P(x) = P_1 \exp\left(-\frac{x}{L_S}\right) \qquad (3)$$

where L_S is the spin relaxation (or diffusion) length as described before. Exponential decay of spin polarization with distance has also been confirmed experimentally [37]. Thus when the carriers arrive at the detector interface, their spin polarization becomes $P(d) = P_1 \exp(-\frac{d}{L_S})$, where d is the distance between the injector and the detector. Now we apply the Julliere formula on the tunnel barrier at the detector interface which separates the two spin polarizations $P(d)$ and P_2. In this case, using equation (2) we have

$$\frac{\Delta R}{R} = \frac{2P(d)P_2}{1-P(d)P_2} = \frac{2P_1P_2\exp(-\frac{d}{L_S})}{1-P_1P_2\exp(-\frac{d}{L_S})} \tag{4}$$

This is the so-called "modified Julliere formula" which is widely used to estimate L_S [38], [39]. In almost all applications of this model, the quantities P_1 and P_2 are taken directly from literature [35] and may not represent the exact values of spin polarization relevant for a particular experiment. For purely organic or organic-inorganic hybrid barriers, spin polarizations of the ferromagnets have been found to be less [37] than the tabulated values [35]. Further, any surface contamination of the ferromagnets can also reduce P_1 and P_2. To include these effects, P_1 and P_2 can be replaced by α_1P_1 and α_1P_2 respectively where α_1, $\alpha_2 < 1$. To determine α_1P_1 and α_1P_2 one needs to carry out spin dependent tunneling [40], muon spin rotation [41] or two photon photoemission experiments [42]. It is straightforward to show that $L_{S,\mathrm{actual}} > L_{S,\mathrm{Julliere}}$ where $L_{S,\mathrm{actual}}$ ($L_{S,\mathrm{Julliere}}$) is the L_S value without (with) the assumption $\alpha_1 = \alpha_2 = 1$. Since α_1 and α_2 are generally unknown, the estimated L_S (i.e. $L_{S,\mathrm{Julliere}}$) provides a *lower bound* of the actual value and should be interpreted accordingly. In spite of this inherent limitation, this model provides valuable insight and can be used to obtain a rough estimate of L_S. Dependence of L_S on temperature and bias can be used to shed light on the spin dynamics in the nonmagnet.

1.3 Organic Spintronics.

As mentioned before, most of the studies in spintronics have been performed on metallic systems, tunneling insulators and inorganic semiconductors (e.g. silicon, germanium, gallium arsenide, indium arsenide etc.). Organic semiconductors are relatively new entrants in the domain of spintronics. Organic semiconductors can be classified in two broad categories: (*a*) low molecular weight compounds and (*b*) long chain polymers. These materials have some attractive features such as inherent structural flexibility, availability of low-cost bulk processing techniques, integrability with inorganic materials and possibility of chemical modification of the molecular structure to obtain tailor-made optical and electrical properties. Consequently organic materials have found a niche in the silicon dominated electronics market. These materials have been used extensively to realize devices such as organic light emitting diodes [43], photovoltaic cells [44], field effect transistors [45] and even flash memories [46].

Organic materials are mostly hydrocarbons with a π-conjugated structure (alternating single and double bonds). The p_Z orbitals of the sp^2 hybridized carbon atoms overlap to form a delocalized π electron cloud. The electrons in this region do not belong to a single atom or bond, but belong to the entire conjugated molecule or polymer chain. Spin injection from ferromagnet to organic occurs via an interfacial tunnel barrier. The transport inside the organic occurs either via the highest occupied molecular orbital/lowest unoccupied molecular orbital (HOMO/LUMO) levels or by hopping among the defect states within the HOMO-LUMO gap or by a combination of both. For inorganic semiconductors, femtosecond optical spectroscopy has been employed for quantitative analysis of spin injection and transport [47]. Unfortunately, such methods are not viable in organics due to the intrinsic weakness of spin-orbit interaction (SOI) in these materials [48]. Therefore, the vast majority of work in the area of "organic spintronics" has employed spin valve structures to investigate spin injection and transport in organics. Alternative methods that have been developed for organics include (a) Meservey-Tedrow spin polarized tunneling [37], (b) muon spin rotation [41], and (c) two-photon photoemission spectroscopy [42]. The first method is only applicable at low temperatures, whereas the remaining two methods are significantly complex, require access to sophisticated experimental setups and facilities and are not "table-top" type techniques. As a result, spin-valve measurement still remains the most commonly used technique for studying spin injection and transport in organics.

1.3.1 Motivation of This Work.

From a spintronic perspective, organics are important due to two main reasons: (1) First, organic semiconductors exhibit very weak spin-orbit interaction and hyperfine coupling, which results in long spin lifetimes in such systems [49]. Long spin lifetime is desirable for both single spin logic and spin based quantum computing. Spin lifetime can be further enhanced by employing a nanowire geometry [39]. However, such studies are rare due to a lack of organic nanowire fabrication techniques. The first part of this thesis (Chapters 2 and 3) addresses this issue. (2) Second, spin filtering, which includes injection and detection of spins of specified orientation (or polarization), is a key operation in spintronics. As discussed before, electrical spin injection/detection (or filtering) is generally achieved by ferromagnetic materials. Unfortunately, spin filtering efficiencies of ferromagnets are typically <50%, which limits the overall performance of any spintronic device. There exists a growing amount of evidence (mostly theoretical) that chiral organic molecules can potentially offer significant improvement in spin filtering efficiency [50]–[52]. The second part (Chapters 4 and 5) of this thesis explores spin filtering via single wall carbon nanotubes (SWCNTs) wrapped with the organic molecule single stranded deoxyribonucleic acid (ssDNA).

1.3.2 Work Completed and Summary of Contributions.

This section contains a synopsis of our completed work to date. The original contributions throughout the different stages of our work are highlighted below.

(1) For fabrication of the nanowire organic spin valve device, we have used anodic aluminum oxide (AAO) templates. The AAO template contains an array of well-ordered cylindrical nanopores. Formation of nanopores is an outcome of an electrochemical self-assembly process. It is essential to create a highly polished aluminum substrate with surface roughness of only a few nanometers, in order to obtain well-ordered nanopores of uniform dimension. In the first stage of our work (for details, please see Chapter 2 of this thesis and ref. [53]), we have developed a novel "chemical polishing" method that results in the desired surface quality. This method has several advantages over the conventional electropolishing method [53].

(2) In the second stage (for details, please see Chapter 2 of this thesis), we have fabricated organic nanowires within the nanopores of the AAO template. There are very few reports in literature on fabrication of small-molecular organic nanowires in AAO templates. These works used a special organic evaporator with the facility of a carrier gas inside the deposition chamber. This method, however, does not allow growth of nanowires of arbitrary dimensions. We have developed a novel "centrifugation-assisted" technique that allows organic nanowire growth within the nanopores of AAO templates [54].

(3) In the third stage (for details, please see Chapter 2 of this thesis), we have extensively characterized the organic nanowires grown by the above-mentioned technique. In addition to field emission scanning electron microscope (FESEM) studies, we have performed X-Ray diffraction (XRD), photoluminescence (PL) and Fourier transform infrared spectroscopy (FTIR) characterization of these nanowires [54].

(4) In the fourth stage (for details, please see Chapter 3 of this thesis), we have successfully combined the above-mentioned techniques to fabricate rubrene *nanowire* spin valve devices. Rubrene has been selected since based on recent reports this material is expected to show a large spin relaxation length [37]. Both electrical and spin transport measurements have been performed on rubrene nanowire spin valves. The magnetoresistance data clearly shows the spin valve signal, indicating successful spin injection, transport and detection in these devices. Suppression of spin relaxation is observed in rubrene nanowires compared to thin films. This experiment also sheds light on the possible spin relaxation mechanism in rubrene nanowires. Control experiments have been performed to confirm the physical origin of the observed effect [55].

(5) In the fifth stage (for details, please see Chapter 4 of this thesis), we have synthesized and dispersed single wall carbon nanotubes wrapped with single-stranded deoxyribonucleic acid (ssDNA). We have also characterized these hybrid nanotubes through FESEM, atomic force microscopy (AFM), Raman spectroscopy and photoluminescence (PL). We have observed a spontaneous alignment of these hybrids on bare SiO_2.

(6) In the sixth stage (for details, please see Chapter 5 of this thesis), we have performed electrical transport measurements on the CNT-DNA hybrid nanotubes synthesized in stage five. Our experimental results indicate that these hybrid nanotubes can act as efficient spin filters. Control experiments have been performed to confirm the physical origin of the observed effect.

1.3.3 Future Directions.

As mentioned before, organic materials can act as efficient spin filters and hence improve spin injection and detection efficiencies. Based on our experimental results on CNT-DNA hybrids (stage six) and previous works reported by other groups [50]–[52], few attempts could be made to explore the spin filtering properties of the following organic systems in a magnetic tunnel junction (MTJ) configuration: (1) Double-stranded deoxyribonucleic acid (dsDNA), and (2) Single wall carbon nanotube wrapped with single-stranded DNA (ssDNA). Details of these possible future projects have been discussed in the last chapter of this thesis.

Chapter 2*

Fabrication and Characterization of a Highly Ordered Array of Rubrene Nanowires.

In this chapter, we will briefly describe the first, second and third stages of our work. We start with a brief overview of the existing methods of organic nanowire fabrication and the limitations of these methods. Then we introduce our approach and furnish the experimental results. The spin valve measurements on these structures (fourth stage of work) will be presented in the next chapter.

2.1 Introduction.

π-conjugated organic semiconductors have been studied extensively over the last few decades due to their unconventional attributes such as tunability of electrical and optical properties by chemical modification, structural flexibility, amenability to low-cost bulk processing techniques and integrability with inorganic materials [43], [56]. Organic semiconductors can be broadly divided into the classes of macromolecular polymers and small molecular weight compounds. Nanowires of organic semiconductors are recently attracting increasing interest since this geometry often offers enhanced device performance. For example, in case of organic solar cells, a promising method of improving efficiency is to achieve nanometer scale interpenetrating networks of donor and acceptor materials, with an interfacial distance smaller than the exciton diffusion length (~10–20 nm) in the organic. An ideal configuration that has been proposed for these cells consists of an array of vertically aligned donor organic nanowires attached to an electrode and surrounded by an acceptor type organic connected to another electrode [57]–[62]. Similarly, electrical properties of organic nanowires can be tuned by varying the nanowire geometry [63] and can potentially be exploited to develop high-performance transistors that rival the performance of amorphous silicon [64]. Finally organic nanowires have recently emerged as a promising candidate in the relatively new field of "organic spintronics" [1], [49], [65]. Organic materials, due to their weak spin-orbit and hyperfine interactions offer an attractive platform in

---

*Parts of this chapter have been published in refs. [53], [54].

which spin memory of a carrier can be preserved for sufficiently long time [39], [66]. This makes organics a suitable host for spin-based classical and quantum bits [39], [66]. The chemical composition of the organics and molecular packing can be changed to control the strengths of these interactions [67]–[69] and hence spin lifetime is tunable in such systems. Further, nanowire geometry allows identification of the dominant spin relaxation mode in organics [39] and investigation of spin-phonon coupling [70], a knowledge of which is a crucial ingredient for room-temperature organic spintronics [71].

Despite all the above-mentioned potentials, fabrication of organic molecular semiconductors in nanowire shape with controllable geometry and aspect ratio remains a significant challenge. The commonly used techniques include submicron lithography, electrospinning, supramolecular self-assembly in solution and at interfaces, physical vapor transport and template assisted synthesis [72]. For the fabrication of high-density arrays of *vertically aligned and segmented* nanowires, template based approaches appear to be more promising. This method offers tight control over the geometry of the nanowires and inter-nanowire spacing and can be easily integrated with additional fabrication steps to produce functional optical, electronic, optoelectronic and spintronic devices [53], [73]. In this work, we use an anodic aluminum oxide (AAO) template for the synthesis of organic molecular nanowires. Compared to polymer track etched membranes, anodic alumina templates offer better pore ordering and higher pore density. Anodic alumina templates also allow a wider range of pore length and diameter and higher thermal and mechanical stability compared to soft templates such as block copolymers.

In the past, several groups have reported AAO-based synthesis of long chain polymer nanowires. For example, refs. [74], [75] synthesized nanorods and nanotubes of poly(*p*-phenylene vinylene) (PPV) within the pores of AAO template. Polypyrrole (PPy) nanowires have been grown using electropolymerization [76], [77]. Arrays of PEDOT nanowires hosted in AAO template have been reported in ref. [78]. Among other polymers that have been grown within AAO are PFO [79]–[83], F8T2 [82] (solution assisted template wetting), Poly(3-hexylthiophene) [84], regioregular polythiophene [85], and P3MT [86] (electrochemical polymerization). The work cited above represents a small cross-section of the huge amount of research that has been performed to date on polymer nanowire synthesis in AAO template. Refs. [72], [87] provide a comprehensive review of this area. However synthesis of *small molecular weight organic semiconductors* in AAO templates has received limited success in the past [87] in spite of the huge technological potential of such materials. Refs. [39], [71], [88], [89] performed evaporation of small molecular weight organics within the pores. For small pore diameter (∼50 nm), only a very thin layer (∼30 nm) of organic can be deposited [39], [71], [88] within the pore. Prolonged evaporation tends to clog the pores and halts the nanowire growth process [54]. For longer nanowires it is necessary to employ larger diameter pores (∼200 nm), [89] which is unfortunately too wide to provide any significant functional advantage for many device applications, and this method therefore does not offer any structural tunability. Refs. [90]–[92] reported fabrication of fullerene nanowires within the nanopores via a template wetting method. However, in most cases thick commercial templates (∼50 μm thick) with both side open pores and large diameter (∼200 nm) were used. Such a method has not produced nanowires in one-side closed pores presumably due to the presence of trapped air pockets within the pores. We note that one-side open pores are more common in device applications where short nanowires are required and hence the template is synthesized on a suitable substrate, which provides necessary mechanical stability to the fragile template. The ability to fabricate nanowires of molecular organics with controllable geometry in the sub-100 nm regime would be an important advance since it would allow us to exploit the diverse benefits of nanoscale features in various optical, electronic, optoelectronic and spintronic applications where organic materials such as rubrene or Alq_3 play a pivotal role.

In this chapter, we describe our work on small-molecular organic nanowire growth within the cylindrical nanopores of AAO templates. We have successfully synthesized nanowires of four different molecular organics [54] that are commonly used in organic photovoltaics, light-emitting diodes, transistors and spin valves: (a) rubrene (5,6,11,12-tetraphenylnaphthacene), (b) tris-8 hydroxyquinoline aluminum (Alq_3), (c) fullerene (C_{60}) and (d) PCBM ([6,6]-phenyl- C_{61}-butyric acid methyl ester). The cylindrical nanopores of the AAO template are of small diameter (~20-80 nm), short length (~1 μm) and the templates are supported on a substrate. In the next section we describe the synthesis of a nanoporous AAO template.

2.2 Synthesis of Hexagonally Ordered Nanopores in AAO (1st Stage of Work).

AAO templates containing hexagonally ordered nanopores have been widely used over the last decade for the development of numerous functional nanostructures such as nanoscale sensors, computing networks and memories [73], [93]. The long-range pore order requires the starting aluminum surface to be extremely smooth. Electropolishing is the most commonly used method for surface planarization prior to anodization. While prevalent, this method has several limitations in terms of throughput, polishing area and requirement of special experimental setups, which introduce additional speed bottlenecks in the intrinsically slow AAO-based nanofabrication process. In the first stage of this work, we have developed [53] a new **"**chemical polishing**"** approach, which circumvents these stumbling blocks in the pretreatment phase and offers a viable, simpler, safer and faster alternative to electropolishing.

AAO is characterized by a homogeneous morphology of parallel pores which grow perpendicular to the template surface with a narrow distribution of diameter, length and interpore spacing, all of which can be easily controlled by suitably choosing the anodization parameters such as pH of the electrolyte, anodization voltage and duration of anodization [73], [93]. A wide range of materials can be deposited (or grown) selectively within the pores using various techniques such as electrodeposition [94], [95], sputtering [96], thermal evaporation [97], pulsed laser deposition [98], [99], chemical vapor deposition [100], sol–gel molding [101], filtration [102] and high temperature impregnation [103]. Such templates can also be used in conjunction with other top-down or self-assembly techniques to produce higher order nanofabrication protocols [104]. The steady state pore formation (and their self-assembly in a hexagonal pattern) results from a balance between two competing processes [73], [93]: (a) electric field assisted dissolution of aluminum oxide (or alumina) at the oxide/electrolyte interface and (b) formation of alumina at the oxide/aluminum interface. The pore formation process can be made spatially periodic by patterning an extremely smooth aluminum substrate prior to anodization. Long range pore ordering is desirable for myriad applications such as nanoscale memories and photonic crystals. Lack of surface smoothness prevents self-organization of the pores, and hence virtually all experiments that employ AAO start from a pretreatment step in which the aluminum substrate is first polished to attain a desired degree of surface smoothness. This smooth surface is then either subjected to (a) multiple anodization-and-etching steps [105] or (b) a pre-patterning stage followed by a single step anodization [106]–[109] to achieve long-range pore order. The former method results in a quasi-monodomain structure whereas the latter produces a perfectly ordered nanopore lattice. In literature, electropolishing is the most commonly used surface planarization technique (see, for example, [105]–[119]. The so-called L1 solution (a mixture of 62 cm^3 perchloric acid, 700 cm^3 ethanol, 100 cm^3 butyl cellusolve and 137 cm^3 distilled water) has been studied extensively since it produces different nanoscale patterns under different electropolishing conditions [110], [111]. Several other electrolytes such as a perchloric acid–ethanol mixture [105], [107], [108], [112], [113], [115], [116], [119] and a mixture of phosphoric acid, sulphuric acid, water (or chromic oxide) [114], [117], [118] have also been reported. Interestingly, perchloric acid is a common ingredient in most cases and produces better smoothness compared to the solutions that do not contain perchloric acid [110], [117].

While popular, electropolishing (with a solution that contains perchloric acid) comes with several practical disadvantages. All of these originate from the fact that hot perchloric acid is a hazardous chemical, which requires special handling. For example, during electropolishing the electrolyte gets heated and hot perchloric acid is well known for its notoriously strong oxidizing properties and its potential to become unstable. This requires continuous cooling of the electrolyte during polishing. Even storing of these electrolytes requires a special **"**perchloric acid fume hood**"** with self-contained wash-down units to inhibit formation of metallic perchlorate crystals on the walls of the fume hood and the exhaust ductwork. These crystals are highly unstable and shock-sensitive and may ignite or detonate under certain conditions. We note that electropolishing is mainly a serial process and with commercial electropolishers (such as Buehler Electromet-4), only one sample can be electropolished at a given time resulting in a slow throughput. Using custom-built electropolishing setups, it is possible to simultaneously electropolish multiple aluminum substrates in parallel in an electrolyte, but again this generates larger amounts of heat (compared to the single substrate case) requiring highly efficient heat removal from the system [53]. Ultimately the maximum number of substrates that can be electropolished simultaneously will be limited by the cooling capacity of the system. The area of electropolishing is often limited in commercial electropolishers (e.g. the exposed diameter is ~2 cm for Buehler). Again, large area polishing can be achieved by custom-made setups but at the cost of higher current and concomitant evolution of larger amounts of heat. We note that one of the intrinsic drawbacks of AAO based nanofabrication is its slow processing speed. Recently a few approaches have been proposed for accelerating this process [113], [118]. However, the factors mentioned above indirectly introduce additional speed bottlenecks, which thwart large-scale production of high quality AAO templates. Thus an alternative fast polishing technique that will avoid these disadvantages and at the same time produce AAO templates of comparable quality is highly desirable.

In ref. [53] we have explored a **“**chemical polishing**”** process, which was originally invented in the 1930s [120]. This method has been rarely used in nanostructure fabrication even though it allows parallel processing of a large number of aluminum substrates with arbitrary areas and does not necessarily requires perchloric acid. One early work [121] employed a variation of this technique for structural investigation of alumina films. In this report, the chemical polishing process is characterized by the use of a mixture of nitric and phosphoric acid (note the absence of perchloric acid) and an elevated solution temperature. However, use of this process in the AAO literature is rare (if any), mostly because of difficulties in controlling the surface smoothness and poor quality of the AAO template. We note that ref. [122] studied a similar chemical polishing approach, albeit with different polishing reagents and conditions. In this study, the chemical polishing produced inferior surface smoothness as compared to the electropolished surface. Ref. [119] reported yet another chemical polishing approach which produced a disordered porous structures with adverse effects on the parallelism of the pores. In our work, we demonstrate the opposite behavior i.e. we first show that the chemical polished surface is more smooth compared to the electropolished surface, if the polishing parameters lie in a certain window. The maximum size of the aluminum substrate is only limited by the size of the bath, and we have successfully (chemical) polished substrates as large as 10 cm × 10 cm. After chemical polishing, the entire surface is shiny and mirror-like and appears almost identical to the electropolished surface. Next, we will show that after anodization of the chemically polished surface, the parallelism of the pores is preserved and the template quality is comparable to that of the electropolishing case. Thus, the proposed method is a viable, simpler, safer, faster alternative for fabrication of good quality AAO templates. Surprisingly, under certain polishing conditions, we observed self-assembly of highly ordered nanoridge patterns. Such morphologies can be used as mask to produce nanoscale interconnects in crossbar architecture.

We have used 2 cm × 2 cm coupons of high purity unpolished aluminum (99.997%, Alfa Aesar) with thicknesses of 250 μm. High purity aluminum is required to avoid potential breakdown phenomena and formation of cracks during the oxide formation (anodization) process. These unpolished samples have been subjected to the chemical polishing step. The etchant consists of 15 parts of 68% nitric acid and 85 parts of 85% phosphoric acid. This recipe completely avoids perchloric acid and the related hazards discussed before. The etching is performed for various durations (2 – 7 min. for the temperature range 45°C–95°C). After etching, the samples are neutralized in 1 M sodium hydroxide for 20 min. Surface topography for each polishing condition has been studied extensively by atomic force microscopy to determine the optimum conditions [53]. Next, we prepared standard electropolished specimens to compare the quality of surface finish with the above-mentioned chemical polish method. There exist numerous recipes of electropolishing (e.g. [105]–[119]). In this work, we choose the method of refs. [110], [111], which has been thoroughly characterized in literature. In this method, the etchant consists of 700 cm^3 ethyl alcohol, 100 cm^3 butyl cellusolve, 62 cm^3 perchloric acid and 137 cm^3 distilled water. We employ a commercial Buehler Electromet-4 polisher/etcher apparatus with a polishing area ~2 cm in diameter. In this setup, the aluminum foil acts as the anode and remains in contact with the L1 electrolyte. Electropolishing is carried out under a dc bias of 45 volts for 10 s. Under these conditions, electropolishing current density is ~3 A/cm^2 which results in evolution of considerable amounts of heat. The electrolyte is cooled down by passing cold water through the cooling coils, which are in physical contact with the electrolyte. Cooling the electrolyte is necessary for two reasons: (a) using hot electrolyte for polishing results in visible imperfections and defects on the surface; and more importantly (b) hot perchloric acid is potentially explosive and can cause safety hazards. The electrolyte is vigorously stirred during electropolishing in order to prevent material congregation on the aluminum substrate. It is to be noted that the above-mentioned parameter set for electropolishing has been chosen from early work in this area, which extensively characterized surface smoothness as a function of various electropolishing parameters. In these studies, longer electropolishing time did not show significant improvement in surface roughness [111]. However, in principle it may be possible to obtain better surface smoothness for a separate set of electropolishing conditions. Even in such a case, the purely chemical method we performed will still remain a simpler, safer and faster alternative.

Finally, we perform multistep anodization on the chemical polished samples to examine the quality of the porous structures. Multistep anodization is a standard process for fabrication of ordered nanopores on the alumina template and has been investigated by many authors (e.g. [105]). Briefly, a polished piece of aluminum is anodized for short time (~15 min, 3% oxalic acid and 40 V dc at room temperature), which results in a thin layer of nanoporous oxide on the metal. These pores are distributed somewhat randomly on the surface. This thin oxide is dissolved out in hot (60 °C) chromic-phosphoric acid. Then, the sample is re-anodized (under the same conditions) for a long time (10–12 h) to form a thick layer of nanoporous film on the surface. Long time anodization reduces the defects and dislocations in the sample. This oxide layer is again removed by dissolving in hot chromic–phosphoric acid. Removal of this oxide leaves an array of highly ordered "dimples" on the metal surface. For the subsequent (and final) anodization process, these dimples act as initiation sites for the pores. The final step of anodization is carried out for the appropriate duration (under same conditions as in the previous steps) to attain the desired film thickness. All anodization processes in this work have been carried out with a platinum mesh counterelectrode.

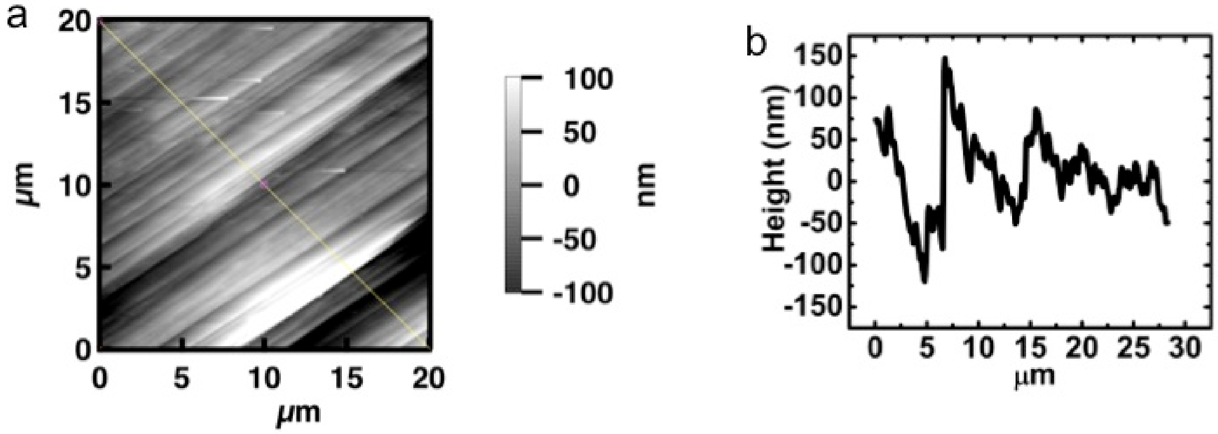

Figure 2.1 (a) Two dimensional AFM topographic image of an unpolished sample for 20 μm scan size. The maximum height variation and standard deviation (σ_0) over the entire surface are 378 nm and 47.5 nm, respectively. (b) Roughness profile along the diagonal line shown in (a). Along this line, the peak-to-peak height variation is ~275 nm. Such roughness makes these samples unsuitable for attaining long-range pore order after anodization.

The anodized area is typically composed of several μm^2 size “domains”. The defects and imperfections tend to accumulate at the domain boundaries. Near perfect pore ordering is obtained within each domain. The arrangement of pores varies slightly from one domain to another. Further improvement in pore ordering can be obtained via imprinting techniques. We show that after multistep anodization, it is possible to grow AAO templates with large area domains on chemically polished samples. The domain areas of these templates are comparable to those grown on electropolished substrates. Thus, using chemical polishing we are not sacrificing the template quality (as compared to electropolishing) but are able to avoid the speed bottlenecks associated with the electropolishing protocol. Thus chemical polishing approach is more appealing for fast fabrication of high quality AAO samples in a simple and less hazardous fashion.

The surface characterization has been performed using an Atomic Force Microscope (AFM). The typical values of scan rate, force constant and resonant frequency were 1 Hz, 42 N/m, and 300 kHz, respectively. The radius of curvature of the AFM tip is <10 nm including the aluminum reflex coating. Characterization of the nanopores after multistep anodization has been performed by a field emission scanning electron microscope (FESEM).

To characterize and compare the surface roughnesses under different polishing conditions, we use two statistical parameters [123]–[126]: (a) standard deviation (σ) of the distribution of surface heights and (b) height correlation length (l). The standard deviation is calculated using the formula [124], [127]:

$$\sigma = \langle \sigma_0 \rangle = \left\langle \left(\frac{1}{N^2 - 1} \sum_{i=1}^{N^2} \left(z_i - \overline{z} \right)^2 \right)^{\frac{1}{2}} \right\rangle \tag{1}$$

where N^2 is the total number of pixels in the image, z_i is the height of the i^{th} pixel, $\overline{z}$ is the average height of the image and $\langle\rangle$ indicates averaging over five non-overlapping areas of the same scan size. However, σ or the shape of the height distribution do not provide the information regarding spatial distribution of the heights. This can be obtained from the two-dimensional height autocorrelation function, which has the following (unnormalized) form:

$$C(p,q)=\sum_{i,j} z(i,j)z(i+p,j+q) \tag{2}$$

where (p, q) indicates the so-called lag vector β and (i, j) is the position vector in the xy plane. The correlation length l is defined as [125]

$$C(l/2)=\frac{1}{e}C(0,0) \tag{3}$$

Physically, the correlation length indicates the distance (or lag |β|) over which the "memory" of the initial height is retained. Beyond this distance, the two points on the surface can be considered as statistically independent. Computation of the normalized autocorrelation function (C_0) is performed by the following routine [53]:

$$C_0(p,q)=\frac{\sum_{i,j}\left[z(i,j)-\bar{z}\right]\left[z(i+p,j+q)-\bar{z}_{p,q}\right]}{\left\{\sum_{i,j}\left[z(i,j)-\bar{z}\right]^2\sum_{i,j}\left[z(i+p,j+q)-\bar{z}_{p,q}\right]^2\right\}^{\frac{1}{2}}} \tag{4}$$

where $z(i,j)$ represents the image height at (i, j), $\bar{z}$ is the image height as defined before, and $\bar{z}_{p,q}$ is the mean height of the shifted image $z(i+p, j+q)$. The correlation length is defined as in Eq. (3). Using these two parameters (σ, l), we determine the optimum conditions for chemical polishing and compare this result with the electropolished case. The AFM images are the raw data without any artificial filtering or smoothing.

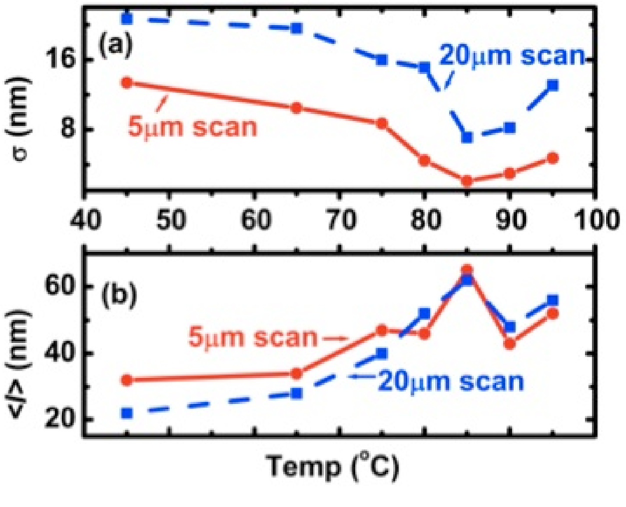

Figure 2.2 Dependence of (a) standard deviation (σ) of the height distributions and (b) correlation length (⟨l⟩) on polishing temperature. Each data point is the average of five non-overlapping areas of same scan size. Etching time is five minutes in each case. The lines through the data points are guides to the eye.

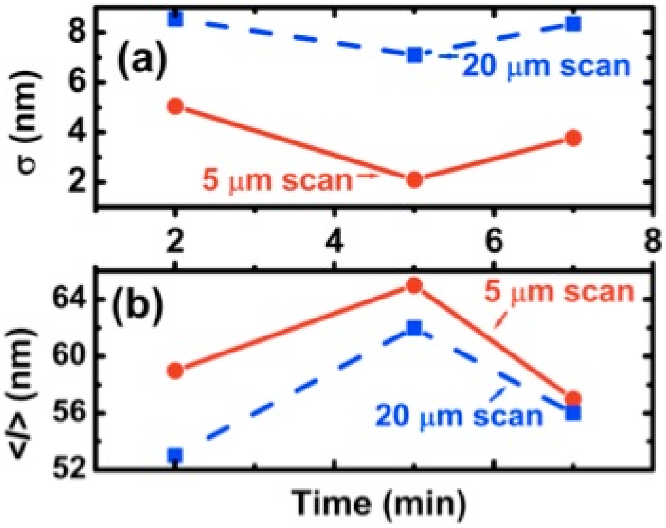

Figure 2.3 Dependence of (a) standard deviation of the height distributions (σ) and (b) correlation length ($\langle l \rangle$) on etching time. Each data point is the average of five non-overlapping areas of same scan size. Etching temperature is 85°C in each case. The lines through the data points are guides to the eye.

Figure 2.1 (a) shows the AFM image of a typical as-received unpolished aluminum foil. The parallel trenches are readily observed, which result from the rolling of the aluminum foil. The height variation over the entire surface is ~ 378 nm, and the standard deviation σ_0 is 47.5 nm. The depth profile along a direction transverse to the trenches is shown in Figure 2.1 (b). Such roughness makes these unpolished substrates unsuitable for attaining long-range order nanopores. This calls for a surface polishing step.

First, we employ the chemical polishing procedure as described earlier in this section. In contrast with the electropolishing case where polishing voltage (along with temperature and duration) plays a crucial role in determining surface features [110], [111], here we have only two parameters (etchant temperature and duration of etching) to optimize. Figure 2.2 shows the variation of σ and $\langle l \rangle$ with temperature. Etching time has been kept fixed for five minutes since for longer etching, the whole aluminum substrate is dissolved away at high temperatures. We observe that σ shows a pronounced minimum and $\langle l \rangle$ attains a maximum at 85°C, indicating that the best surface smoothness is obtained at 85°C. Similarly, we plot σ and $\langle l \rangle$ as a function of etching time (for a fixed temperature of 85°C) in Figure 2.3. The optimum etching time is five minutes. Longer etching tends to dissolve away the entire substrate whereas shorter etching leaves rough features on the surface. The σ values are typically bigger for larger scan sizes since larger areas contain more variations in height. The l (and $\langle l \rangle$) values are, however, relatively independent of scan size, as expected.

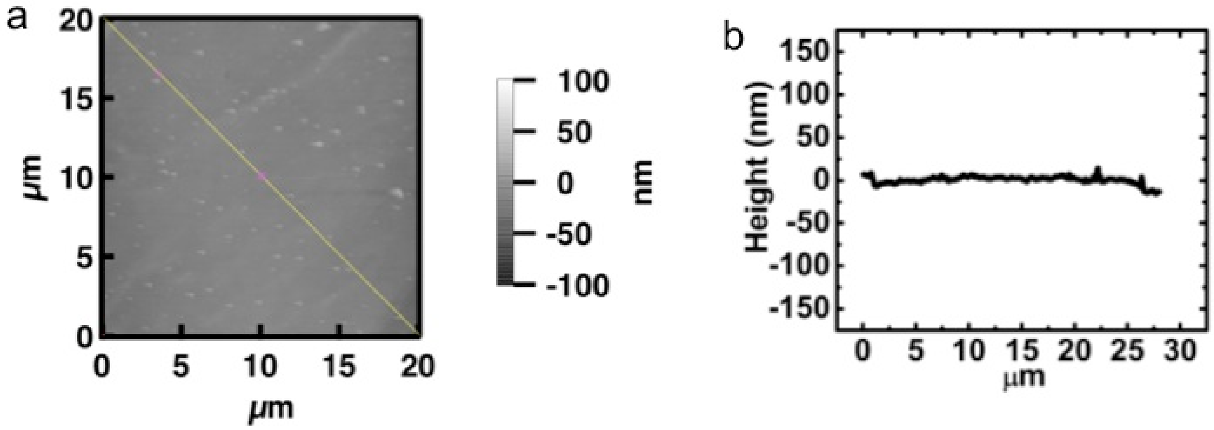

Figure 2.4 (a) Surface morphology of a chemical polished sample for polishing temperature of 85°C and duration of 5 min. The peak-to-peak height variation and the standard deviation (σ_0) over the entire surface (20 μm × 20 μm) are 66.5 nm and 4.93 nm, respectively. (b) Height trace along the diagonal line in (a). The peak-to-peak height variation along this line is ~28.52 nm. The height scales are identical to that in Figure 2.1.

Figure 2.4 shows the surface morphology of a chemical polished aluminum foil, polishing being performed for 5 min at 85°C. The parallel trenches of the unpolished specimen (Figure 2.1) are no longer visible and the peak-to-peak roughness (over the entire area) has reduced to ~ 66.5 nm and $\sigma_0 = 4.93$ nm. If we take σ_0 as a guide, this data indicates almost an order of magnitude improvement in surface smoothness over the unpolished case. Note that both images have the same scale for surface heights.

Next, we compare this method with the standard electropolishing results. Figure 2.5 shows the surface morphology of an electropolished aluminum foil. Electropolishing has been performed according to the process outlined previously in this section. The peak-to-peak roughness is ~ 83.74 nm and $\sigma_0 = 5.68$ nm over an area of 20 μm × 20 μm, which are significantly lower compared to the unpolished case but slightly higher than the chemical polished sample (Figure 2.4). To further confirm this dependence of surface roughness on polishing conditions, we compare the height histograms of a different set of samples which exhibit (a) $\sigma_0 = 68.4$ nm (unpolished), (b) $\sigma_0 = 6.9$ nm (electropolished) and (c) $\sigma_0 = 5.47$ nm (chemical polished) for the 20 μm scan size in Figure 2.6. The chemical polished sample clearly shows the smallest standard deviation and indicates most smooth surface, which is consistent with the previous set of samples, which correspond to Figures 2.1, 2.4 and 2.5. The difference in surface roughness can also be seen immediately from Figure 2.7, which compares the three-dimensional presentation of the AFM topographic images shown in Figures 2.1, 2.4 and 2.5. Polished specimens are observably smoother than the unpolished one. More importantly, the chemical polishing method reported above produces surfaces, which are comparable or slightly better than the electropolished surfaces.

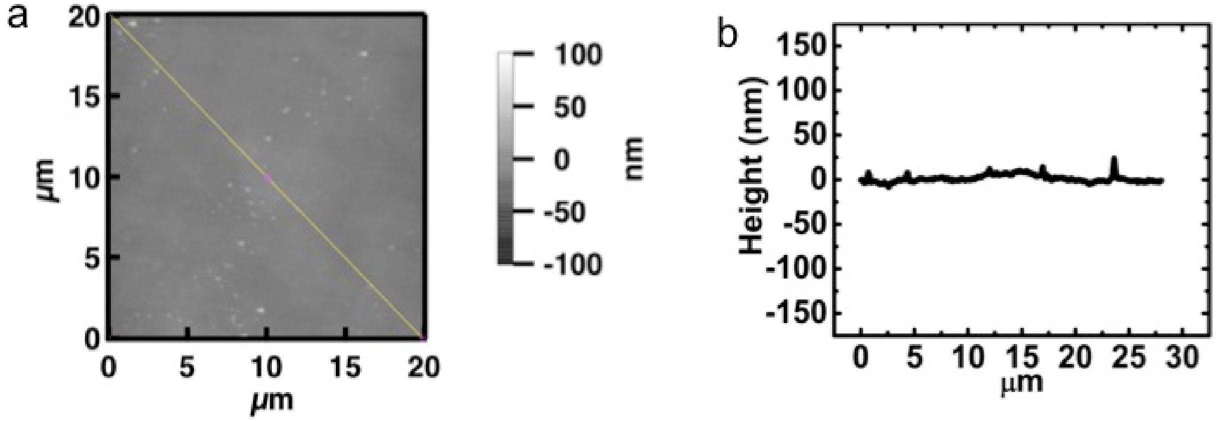

Figure 2.5 (a) Surface morphology of an electropolished sample. The polishing parameters are described in the text. The peak-to-peak variation and standard deviation (σ_0) over the entire surface (20 μm × 20 μm) are 83.74 nm and 5.68 nm, respectively. (b) Height trace along the diagonal line in (a). The peak-to-peak height variation along this line is ~31.83 nm. The height scales are identical to those in Figures 2.1 and 2.4.

In Figure 2.8 we compare the correlation lengths for these three surfaces. The unpolished aluminum shows a correlation length of 12 nm whereas electropolished and chemical polished samples have correlation lengths of 39 nm and 40 nm, respectively. This data is consistent with the observation made above regarding the surface quality of the chemical polished specimens.

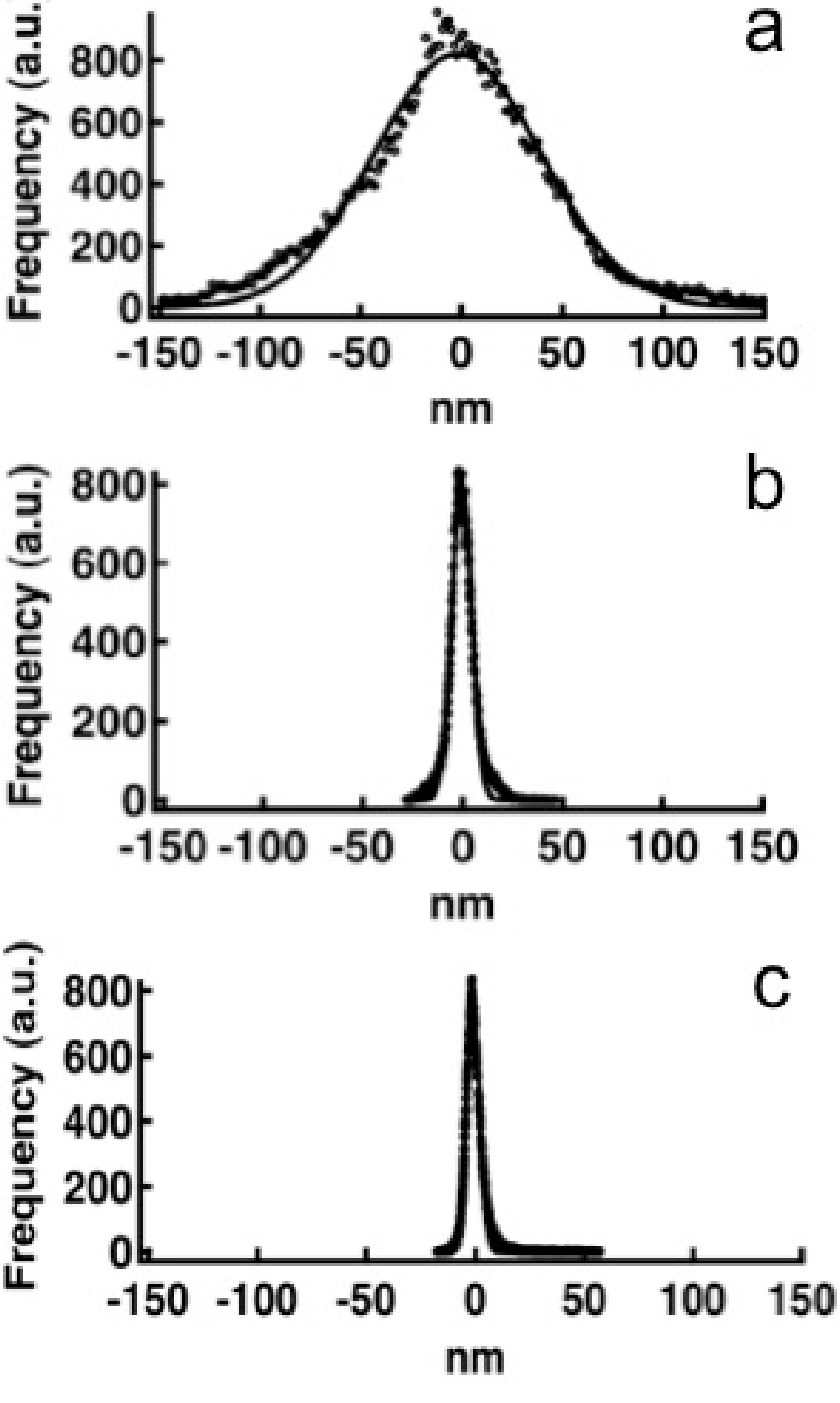

Figure 2.6 Height histograms for (a) unpolished, (b) electropolished and (c) chemical polished specimens for a scan size of 20 µm. The continuous curves represent Gaussian fits with standard deviations (σ_0) of 68.4 nm, 6.9 nm and 5.47 nm, respectively. The polishing conditions are the same as in previous figures.

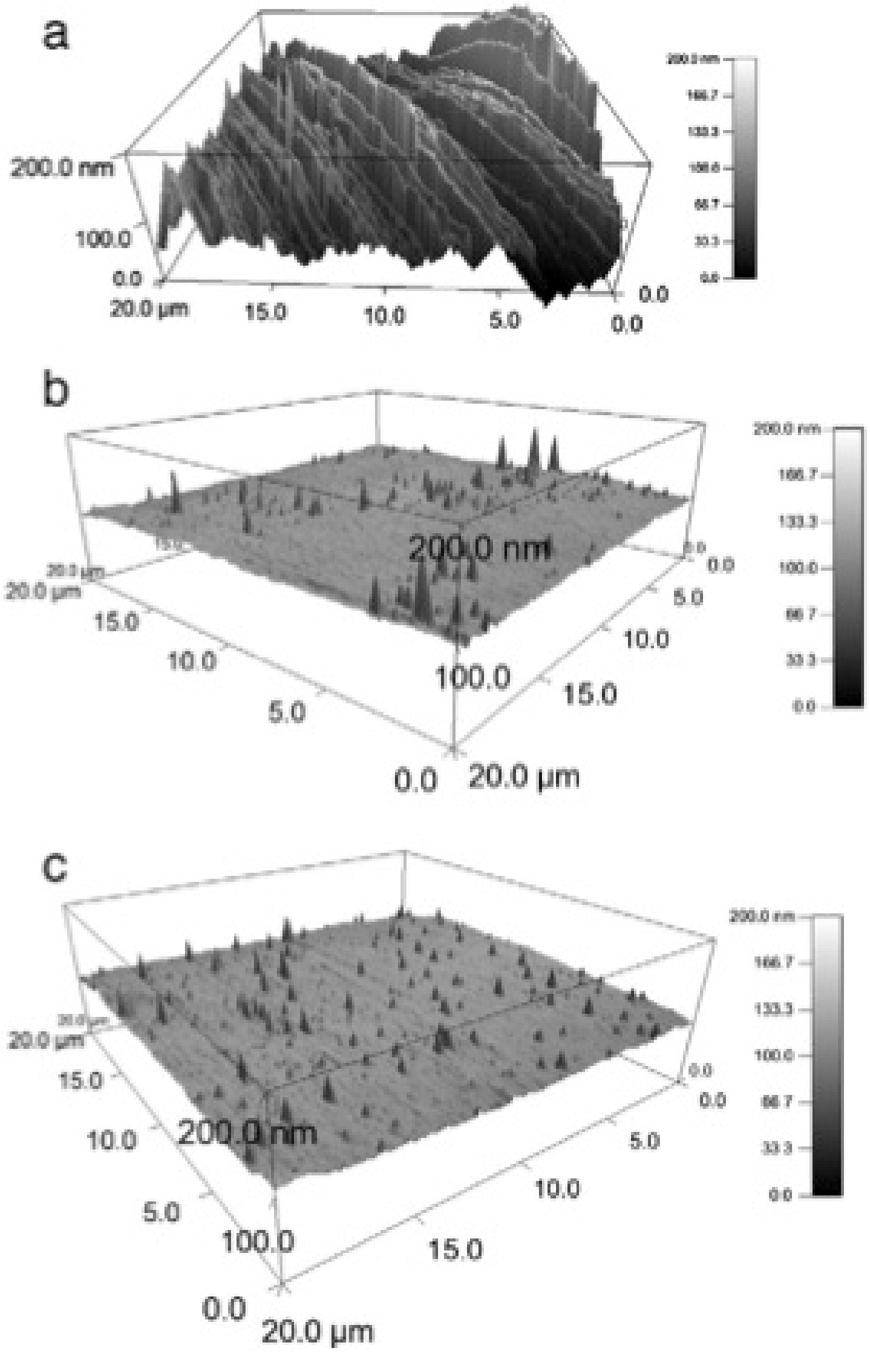

Figure 2.7 Three-dimensional representations of the AFM topographic data for (a) unpolished (Figure 2.1), (b) electropolished (Figure 2.5) and (c) chemical polished (Figure 2.4) samples.

Table 1 summarizes the average standard deviation ($\sigma = \langle \sigma_0 \rangle$) and average correlation length ($\langle l \rangle$) for unpolished, electropolished and chemical polished specimens. The average has been calculated over five different areas with the same scan size of 20 µm. For the electropolished surface, $\sigma = 8.92$ nm ($\langle l \rangle = 56$ nm) whereas σ ($\langle l \rangle$) for chemical polished samples is 7.1 (62) nm.

The σ ($\langle l\rangle$) for an unpolished sample has a much higher (lower) value of 70 (12) nm. Thus, we conclude that compared to electropolishing, chemical polishing can produce similar (or slightly better) surface smoothness under certain conditions. It now remains to be seen if chemical polishing has any adverse effect on pore formation and their regimentation.

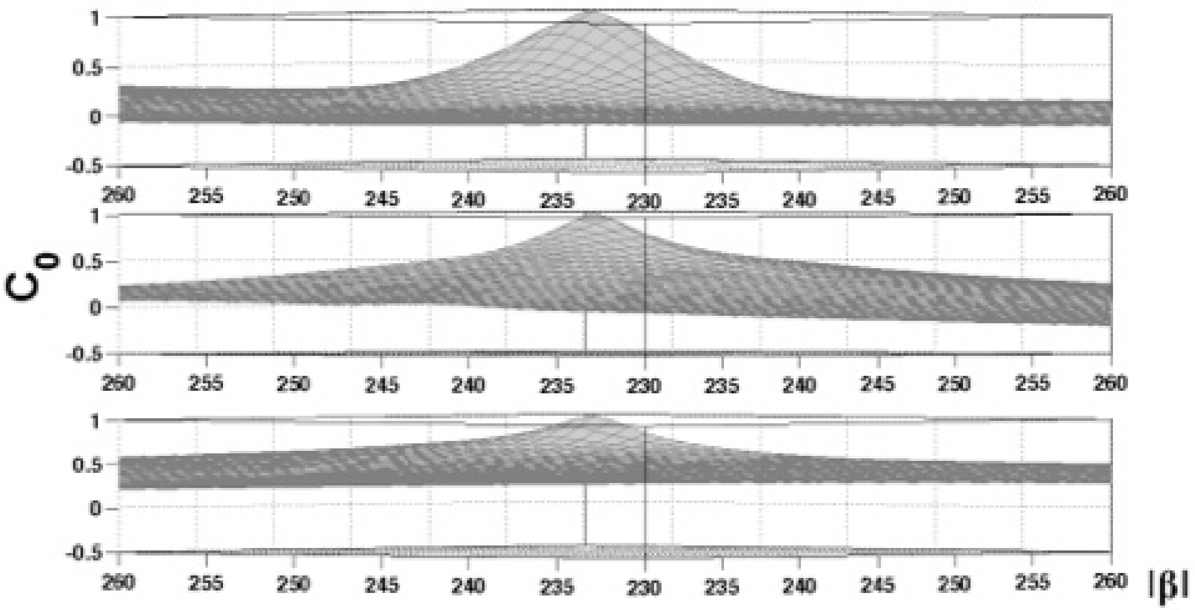

Figure 2.8 Normalized height autocorrelation functions for (top) unpolished (Figure 2.1), (middle) electropolished (Figure 2.5) and (bottom) chemical polished (Figure 2.4) samples. The correlation lengths (measured from C_0 = 1) are 12 nm, 39 nm and 40 nm, respectively. The lag vector (β) in the *xy* plane is in nm. The polishing conditions are the same as in previous figures.

Table 2.1
σ and $\langle l\rangle$ of the images for different polishing conditions. Chemical polishing has been done under the optimum conditions of 85°C and 5 min (ref. Figures. 2.2 and 2.3). Scan size is 20 μm × 20 μm.

Roughness parameters (nm)	Unpolished	Electropolished	Chemical polished
σ	70	8.92	7.1
$\langle l\rangle$	12	56	62

Figure 2.9 (a) and (b) show the top and cross-sectional view of an AAO template fabricated by multistep anodization on a chemical polished aluminum substrate. The pores are clearly visible and form a well-regimented array within domains separated by defects and imperfections. To quantify the area of the perfectly ordered domain, we follow the method used in [128]. Figure 2.10 (a) and (b) show the schematic description and FESEM image of perfect hexagonally ordered pores, respectively. One pore is chosen randomly as a reference and diagonal lines are drawn along three close packing directions. Within an ordered domain, the pores will lie on these diagonals. If the diagonals have *n* pores, the area of the regular hexagon will be given by

$$S=\frac{3\sqrt{3}}{8}D_0^2\left(n-1\right)^2, n=3,5,7,....... \qquad (5)$$

where S is the area of the regular hexagon and D_0 is the interpore separation (~110 nm in our samples). We use this formula to calculate the most probable domain size in our samples. For this calculation, we first determine the most probable value of *n*, following the steps described below [128].

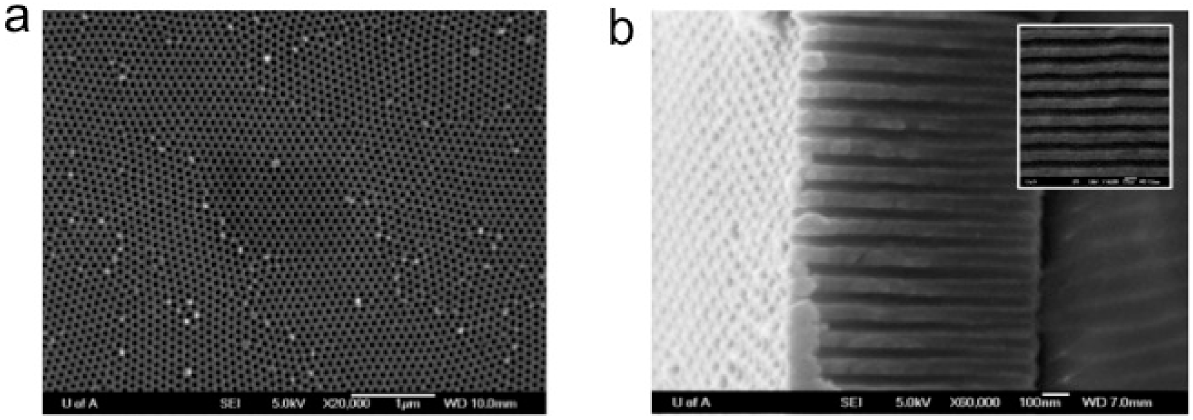

Figure 2.9 (a) FESEM image of the top surface after multistep anodization on a chemical polished (85°C, 5 min) sample. Before chemical polishing, the aluminum foil was annealed at 500°C for three hours. (b) A FESEM image of the cross section of the template. Pore ordering and pore straightness are simultaneously visible. The inset shows a magnified image of the cross-section.

First, we selected random pores on the 20 K magnification SEM images taken at different locations of the same sample. Next step was to draw three diagonal lines along three close packing directions. The diagonals are terminated at domain boundaries beyond which the pores no longer necessarily lie on the diagonal. We have repeated this process for 40 random pores in different locations on the sample. For each position, there are three different n values. Finally we plotted the histogram of all these *n* values (total 40 × 3 = 120) in Figure 2.10 (c) and performed a Gaussian fitting. The most probable value for *n* is 21.16, as determined from this distribution. The average domain area, using the formula mentioned above, turns out to be 3.19 μm^2 with a standard deviation of 0.064 μm^2.

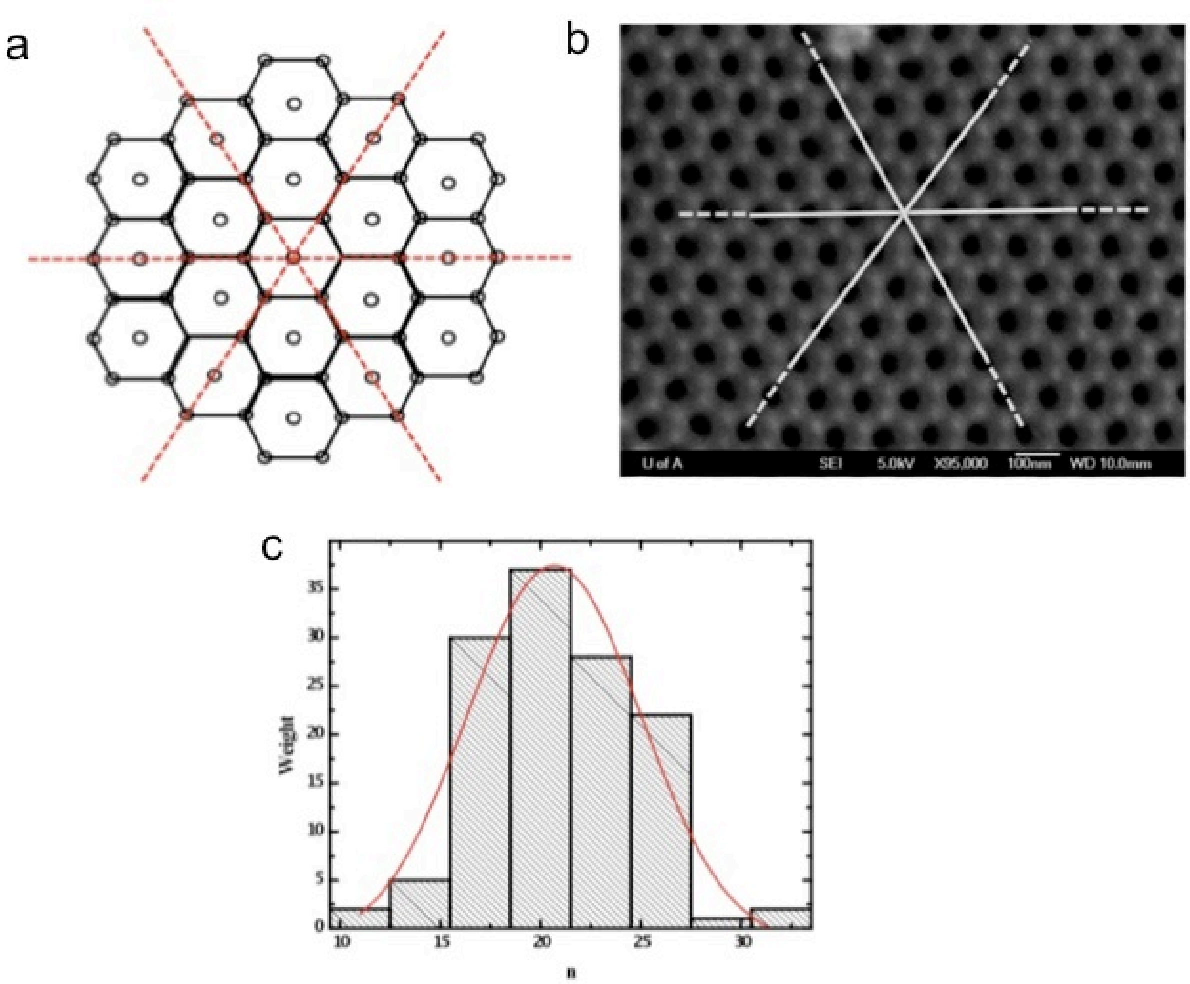

Figure 2.10 (a) Schematic representation of the hexagonal pore arrangement. A random pore at the center has been chosen as the reference and three diagonal lines along the close packing directions are shown. (b) A FESEM image of a part of a hexagonally ordered domain. (c) Distribution for *n* (the number of pores lying on a diagonal line).

These numbers are comparable with previous studies (e.g. [128]), which characterized domain sizes after multistep anodization on electropolished specimens. This study reported a maximum domain area of 2.6 ± 0.11 μm^2 after rigorous preprocessing that includes extensive annealing combined with both chemical and electropolishing. Here, we show that a comparable (or even better) porous structure can be obtained just by chemical polishing. This method is also faster and safer as described before. We also note that Figure 2.9 is in sharp contrast with previous studies (e.g. [119]), which reported disordered pore arrangement as a result of chemical polishing. The current-time transients during anodization (not shown) are nominally identical to the electropolished case and the pore initiation process starts within the first few seconds. Thus, the described chemical polishing method is a viable alternative for the standard electropolishing protocol. The domain size can be further improved by tuning the annealing parameters (temperature, time [128]) prior to the polishing step. Long-range pore order can be achieved by using prepatterning techniques [106]–[109] on the chemical polished surface.

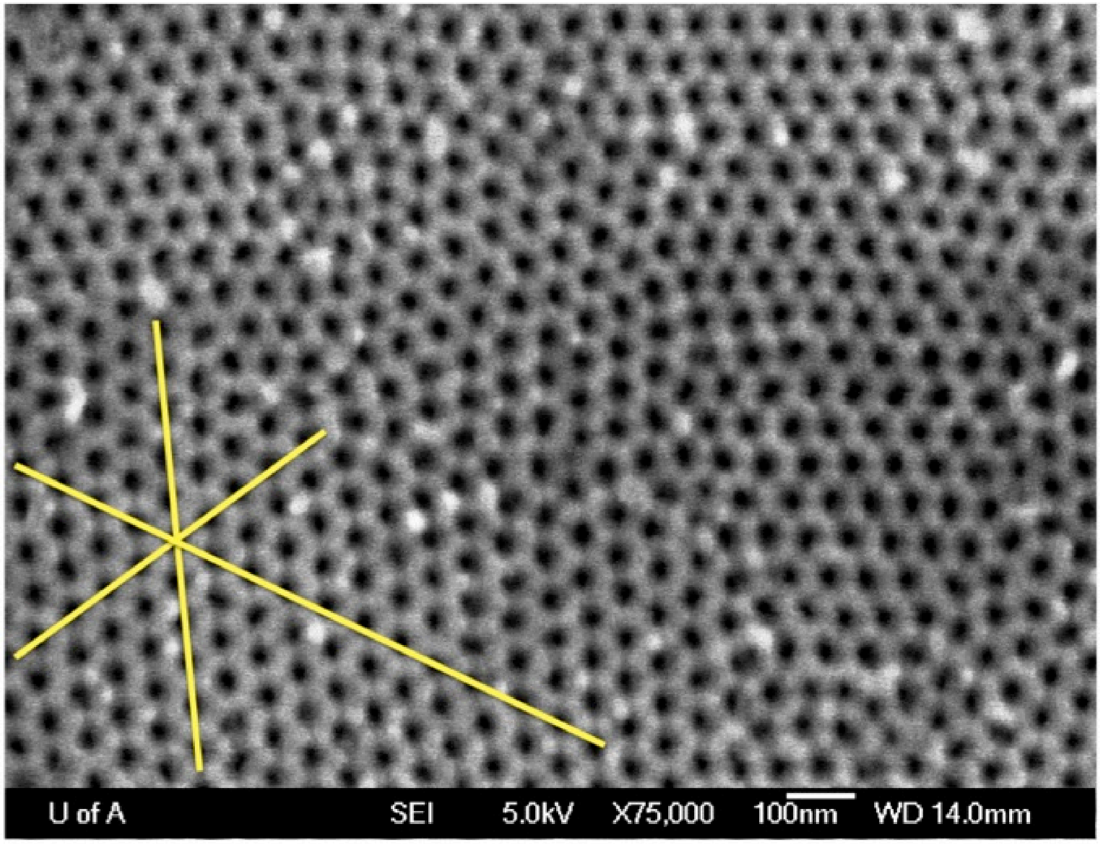

Figure 2.11 A FESEM image of nanopore arrays with nominal pore diameter of ~20 nm. The diagonal lines indicate the hexagonal close packing directions.

Highly ordered nanopores of different diameters were successfully synthesized on chemical polished surfaces. For example, anodization using 0.3 M sulphuric acid and 25 V dc results in nanopore arrays with nominal pore diameter of 20 nm (Figure 2.11). Similarly, anodization using 1.6 M malonic acid and 120 V dc produces nanopore arrays with nominal pore diameter of 200 nm. It is to be noted that chemical polishing is much more convenient than electropolishing especially when lateral anodization of aluminum substrate is required. This type of anodization has recently attracted significant attention since it opens the possibility of synthesizing three terminal devices using AAO technique [129], [130].

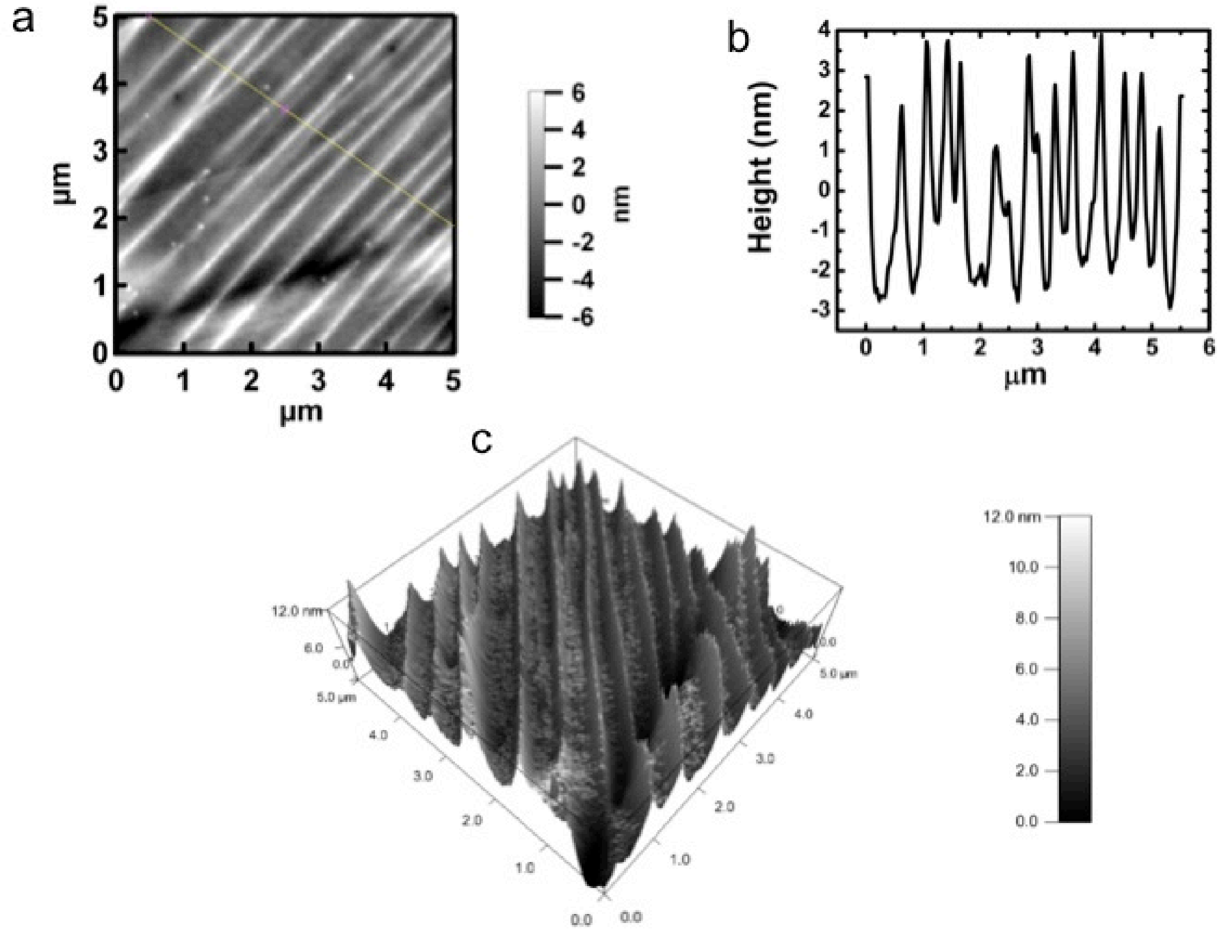

Figure 2.12 (a) AFM image, (b) line plot and (c) three dimensional topography of a chemical polished sample at a polishing temperature of 90°C. The thickness (FWHM) of the ridges are ~ 100 nm. The periodicity is ~ 0.5 µm and the peak to valley ratio is ~ 6.

We would also like to make an intriguing observation about the surface topography beyond the optimum polishing temperature. While the smoothest surface is obtained for an etchant temperature of 85°C, nanoscale ridges begin to evolve at ~ 90°C. Such a configuration is shown in Figure 2.12. The peak to trough ratio is ~ 6 with a periodicity of ~ 0.5 μm. The ridges are parallel, extend over several microns, and have a full width half maximum height of ~ 0.1 μm. Such patterns can be potentially exploited as a mask to develop crossbars for nanoscale memory circuits [110], [111].

In the first stage of our work, we have demonstrated a chemical polishing technique which offers a simpler, faster and safer route for aluminum pretreatment prior to anodization. This work is intended to draw renewed attention on the oft-overlooked chemical polishing method which has several advantages over the commonly employed electropolishing approach. We have performed an extensive study of the surface roughness which shows that this method produces similar (or better) results compared to electropolishing. Additionally, this process (a) is parallel with faster throughput (i.e. multiple aluminum substrates with arbitrary areas can be processed simultaneously), (b) is amenable to large area polishing and (c) avoids perchloric acid and related hazards altogether. Ordered nanopores are formed after multistep anodization of chemical polished surfaces. Nanopore formation process is essentially identical to that in the electropolished case. Under certain polishing conditions, parallel nanoridges are formed which can be further processed to fabricate parallel arrays of nanoscale crossbars. Such structures are the linchpins of many nanoscale memories and computing architectures.

2.3 Centrifugation-Assisted Growth of Organic Nanowire in AAO Template. (2nd Stage of Work).

In the second stage of this work, our goal was to grow organic nanowires within the cylindrical nanopores of the AAO template. We developed a novel, reagentless, one-step process that produces an array of vertically oriented organic nanowires within AAO matrix. Unlike other organic nanowire growth methods, this process does not require special apparatus [54]. This method also allows fabrication of axially heterostructured metal-organic bilayer hybrid nanowires, permits direct electrical contact at the two ends of the nanowires and therefore can be used for synthesis of various functional organic nanowire devices.

Preparation of nanoporous anodic alumina templates has been performed by two-step anodization of chemically polished aluminum foils, [53], [73] as described in the previous section. Pore lengths of several hundred nanometers with diameter and interpore spacing tunable in the sub-100 nm range are required for applications in organic photovoltaics and spintronics since for small molecule organics, the relevant length scales (exciton diffusion length and spin relaxation length, respectively) are typically in this range [39], [65], [131], [132]. As mentioned before, nanowire conductivity can also be controlled by varying nanowire diameter in sub-100 nm regime [63]. The anodization parameters are therefore tuned to generate array features lying in this size range. Figure 2.13 shows field emission scanning electron microscopic (FESEM) images of a pristine (unfilled) oxalic acid anodized AAO template used for synthesizing organic nanowires. In this case, nominal pore diameter is 50 nm, pore length is 1 μm, and wall thickness between neighboring pores is 50 nm. The pores are straight with no signature of branching (Figure 2.13, main image), have narrow size distribution and exhibit a hexagonal ordering (Figure 2.13, bottom inset).

There exists a uniform alumina barrier layer of thickness 30 nm at the pore bottom (Figure 2.13, main image), which needs to be removed for electrical transport experiments. This can be achieved by a pore-side etching technique, which removes the barrier layer with simultaneous widening of the pores (Figure 2.13, top inset). For the removal of the barrier layer we immersed the AAO in 5% phosphoric acid at room temperature for ~ 25 -70 mins., depending on the thickness of the barrier layer. For transport characterization, organic nanowires are grown within such pores and the nanowires are therefore in direct contact with the aluminum substrate, which acts as the bottom electrode. It is important to note that this pore growth process can be executed on arbitrary substrates like glass, indium tin oxide (ITO), silicon, etc. [133]–[135] and a recent work has also shown independent control over pore diameter and interpore spacing [136]. Therefore, using the growth mode described in this work, it is possible to synthesize organic nanowire arrays with controllable geometry on arbitrary substrates as required by a specific application. In this work, we demonstrate the growth method of organic nanowires using aluminum foil as the substrate.

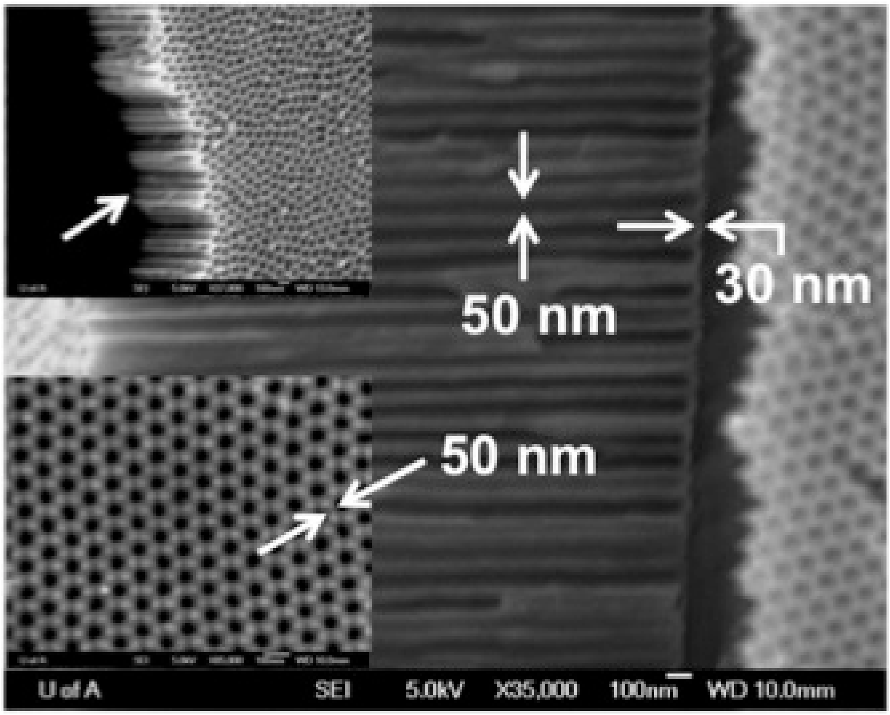

Figure 2.13 Templated synthesis of molecular organic nanowires. (main image) Cross-sectional view of an as-prepared pristine AAO template, synthesized by oxalic acid anodization. The nominal pore diameter is 50 nm. An insulating non-porous barrier layer (30 nm thick) is visible at the pore bottom. (bottom inset) Top view of the template, illustrating hexagonal arrangement of the nanopores. The arrow indicates wall thickness of 50 nm. (top inset) Cross-sectional view of the template after pore-side etching. The arrow indicates removal of the barrier layer.

Standard template wetting techniques typically involve placing few drops of the organic solution on the nanoporous template [54]. The solution enters the pores via capillary action and after evaporation of the solvent, organic material remains inside the nanopores and forms nanowires. As mentioned in the introduction section of this chapter, many groups have used this method successfully in the past to fabricate nanowire arrays of long chain polymers. Unfortunately, this process does not work for small-molecular weight organics. To drive the organic material within the nanopores, we coupled the traditional template wetting technique with a simultaneous fixed angle centrifugation process. The centrifugal force on the solvent thrusts the organic solution within the pores and after evaporation of the solvent, the trapped organic material forms nanowires within the cylindrical nanopores. The experimental setup for organic growth is shown in Figure 2.14 (a). The nanoporous templates are loaded in the centrifugation tubes and are completely immersed in a saturated solution of organics. The centrifugation is carried out at 4000 rpm for 5 min. The samples are not removed from the solution prior to the complete evaporation (room temperature) of the organic solvent. The top surface of the template is repeatedly cleaned by the same organic solvent. This cleaning step does not affect the nanowires hosted within the pores. To confirm the ingression of organic within the nanopores, we have exposed the nanowire tips from the backside of the template by sequential etching of aluminum and the barrier layer. The cleaned top surface was covered with a sacrificial polymer for mechanical stability of the submicron- thick templates.

Figure 2.14 (b) shows the oblique cross-sectional FESEM images of the rubrene nanowires synthesized within the template (main image). The nanowire tips are clearly visible from the backside of the template (top insets). Some of these tips have merged together due to prolonged removal of the supporting AAO host matrix (top left inset). The top right inset shows the nanowire tips after short-time etching of alumina from the backside. In this case, no merging has occurred. In general, we find that after short time etching of the template, the nanowires match perfectly to the contours of the host anodic alumina template. However, after long time etching, the exposed tips tend to have slightly larger diameter than the nanopores. This "swelling" occurs because during the etching process, the aqueous solvents expand the organic nanowires and the expanded shape does not return to its original form even after drying. A similar effect has been reported before in the context of template grown polymer nanowires [74].

Figure 2.15 (a) shows Alq_3 nanowires grown in 50 nm pores. The nanowires tend to coalesce after removal of the host template. The inset shows the Alq_3 nanowire tips imaged from the backside of the template. In all cases the FESEM images indicate near complete filling of most of the pores and demonstrate the efficiency of this process for high yield production of well ordered array of vertically oriented organic molecular nanowires. Figure 2.15 (a) and (b) show narrower diameter (20 nm) organic nanowires synthesized in sulphuric acid anodized AAO templates. In this case, both pore diameter and wall thickness are smaller (~20 nm, Figure 2.11) than before. Organic nanowires can still be grown within such narrow pores via the same method described above. Figures 2.15 (b) and (c) show released and bunched nanowires of rubrene and Alq_3, respectively after (near complete) removal of the host AAO matrix.

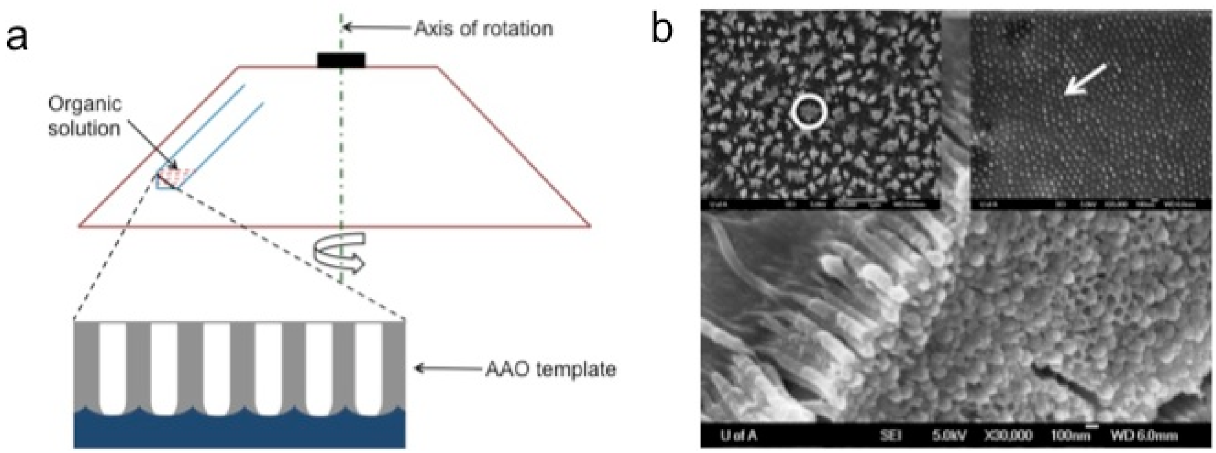

Figure 2.14 (a) Illustration of the fixed-angle centrifugation-assisted growth method for growth of molecular organic nanowires. The empty AAO templates are loaded in a standard commercial centrifuge, which is filled with organic solutions. Centrifugation is performed under the conditions specified in the text. (b) (main image) Oblique, cross-sectional view of the rubrene nanowires (70 nm diameters) grown within the AAO template. (top right inset) Rubrene nanowire tips exposed from the backside of the template after slight removal of alumina matrix. (top left inset) Rubrene nanowire tips merge together (shown by circle) after continued removal of the host matrix.

This method of organic growth can easily be coupled with traditional electrodeposition process to synthesize axially heterostructured metal-organic bilayer nanowires. To achieve this, we first deposit metal at the pore bottom from a slightly acidic solution of an appropriate metal-salt using standard dc (or ac) electrodeposition [53], [73]. Next organic nanowires are grown on top of the metal nanowire segments using the process described above. We note that a wide range of metals (Au, Ag, Cu, Ni, Co and many others) can be deposited within the pores of an AAO template and hence in this method organic nanowires can be easily interfaced with a metal electrode with an appropriate work function suitable for device applications. Later in Chapter 3, we will discuss the transport properties of Co-organic (rubrene) axially heterostructured bilayer nanowires.

Figure 2.16 (a) shows the typical outcome when the traditional template-wetting method (without centrifugation) or physical vapor deposition (without carrier gas) is used to grow organic nanowires within AAO templates. The organic does not enter the pores in these cases. Physical vapor deposition of organic (without any carrier gas) for extended time also results in a thick layer on the top surface as shown in Figure 2.16 (b).

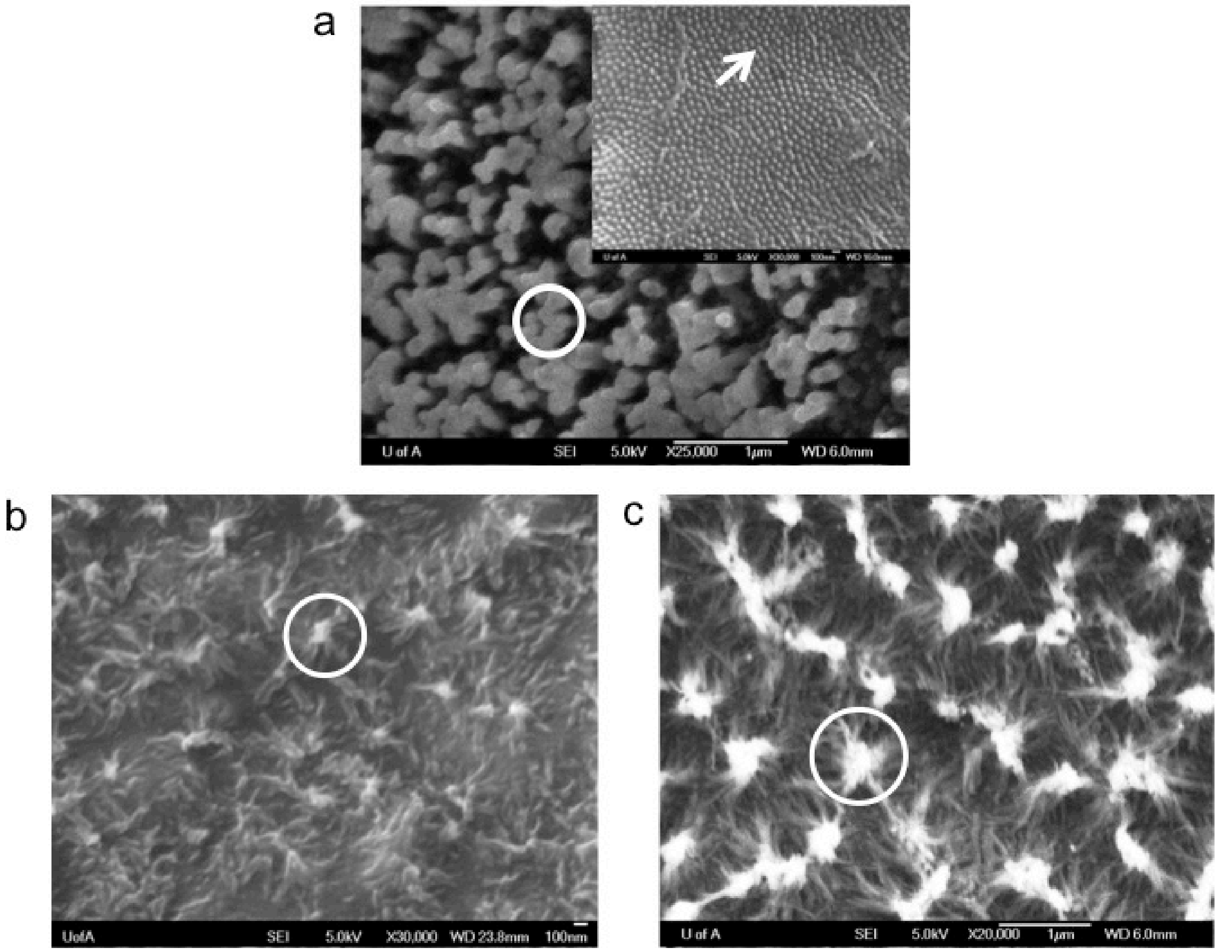

Figure 2.15 (a) (main image) Alq_3 nanowire tips exposed from the backside of the template. Wire diameter is 70 nm and some merging (circle) is visible. (inset) Alq_3 nanowire tips (arrow) after slight removal of the alumina. (b) Rubrene nanowires released from the template. (c) Alq_3 nanowires released from the template. In (b) and (c), the nanowires coalesce together due to the removal of the host AAO matrix, as shown by the circles.

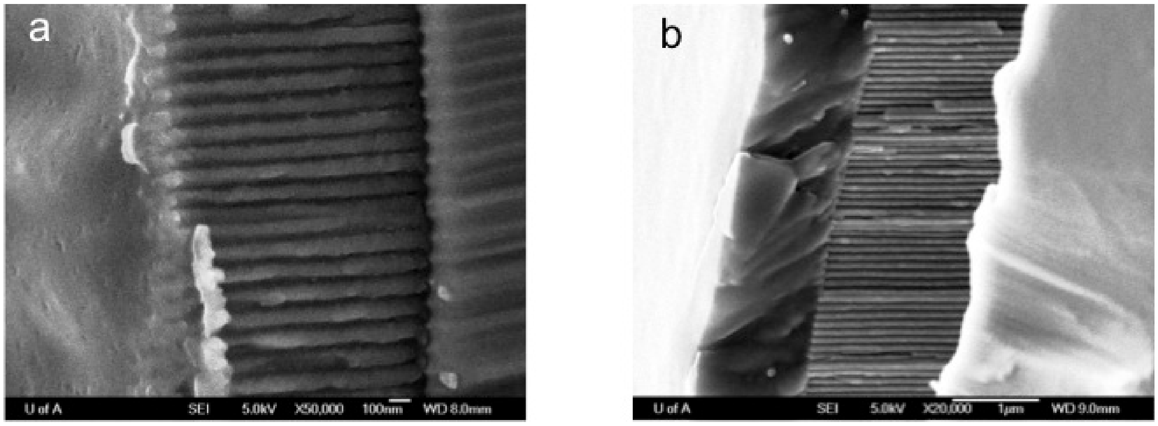

Figure 2.16 (a) Cross-sectional image of the template after traditional template-wetting cycle using rubrene solution. A thick layer of rubrene is visible on the top surface but the pores are empty. (b) Cross-sectional image of the template after physical vapor deposition of rubrene (without carrier gas). Again, a thick layer of rubrene is visible on the top surface but the pores are empty.

2.4 Characterization of Rubrene Nanowires. (3rd Stage of Work).

Prior to conducting electrical transport measurements, we performed a few characterization experiments with the aim of understanding relevant crystallographic, electronic and optical properties of rubrene nanowires grown in AAO. We performed low angle X-ray diffraction (XRD), Fourier transform infrared (FTIR) spectroscopy and photoluminescence (PL) measurements on the organic nanowires grown by the above method [54]. Details of these experiments are provided below.

2.4.1 X-ray Diffraction (XRD).

To investigate the crystallinity of the as-grown organic nanowires, low angle XRD (LAXRD) data has been acquired for the organic nanowire arrays hosted in the anodic alumina matrix. For this study, the top surface of the sample is repeatedly cleaned by acetone to remove any residual thin film layer, and then the nanowire tips are exposed by partial etching of the template in 5% phosphoric acid [54]. Figure 2.17 (a) shows the typical LAXRD diffractograms observed for the following samples: (*i*) annealed rubrene nanowires, (*ii*) as-grown (unannealed) rubrene nanowires and (*iii*) blank alumina template with same thermal history as of (*i*). Figure 2.17 (a) (inset) shows the molecular structure of rubrene. Absence of any diffraction peaks indicates the amorphous nature of the as-grown rubrene nanowires. The host alumina matrix does not exhibit any observable peak either in the scan range employed. This is in agreement with prior studies such as refs. [81]–[83]. However, the crystallinity of rubrene nanowires is significantly improved even after a short time (~15 min) annealing at a moderate temperature of ~200°C. Further optimization of the annealing parameters may result in better crystallinity of the rubrene nanowires.

The peak positions and relative intensities of rubrene nanowires [Figure 2.17 (a), post annealing] have close resemblance with those observed for single crystal rubrene and wide rubrene nanowires (~200 nm diameter) grown by physical vapor transport [89]. For single crystal rubrene, a very sharp crystalline peak occurs at $2\theta \approx 6.7^{\circ}$, which originates from the (002) plane. This agrees well with Figure 2.17 (a) and indicates strong $\pi - \pi$ stacking along the b axis and a high degree of crystallinity along the $a - b$ plane for the rubrene nanowires [54], [89]. We note that rubrene nanowires grown by physical vapor transport exhibit much weaker response at this angle and indicates lower degree of crystallinity [54], [89]. The rest of the peaks for single crystal rubrene occur at 2θ values 12°, 14°, 20° and 27°, which correspond to (010), (004), (006) and (008) planes respectively [89]. These peaks are also present in the XRD spectrum of our nanowire structures. Two additional peaks in the nanowire XRD spectrum [Figure 2.17 (a)] occur at 2θ values 17° and 24°, which represent (300) and (020) planes, respectively. Similar peaks (albeit weaker) have been reported earlier [89] and were attributed to constrained growth of the organic nanowire within limited space of the pore. In our pattern, we observe another new peak at ~18° (2θ) which may originate from enhanced space constraints imposed by smaller diameter pores. We note that there are two major differences between our rubrene nanowire and the vapor phase grown nanowires [54], [89]. First, the former is essentially a solution-based method whereas the latter employs physical vapor transport as the growth mode. The second difference lies in the geometry of the nanowires. As discussed before, our nanowires are ~1 μm long with ~50-70 nm diameter whereas the nanowires reported in ref. [89] are ~50 μm in length with ~200 nm diameter. These factors can lead to different molecular packing within the pores and hence different diffraction peaks. Nevertheless, the presence of the characteristic peaks in the LAXRD pattern confirms the growth and high degree of crystallinity of rubrene nanowires within the AAO templates. Further optimization of the annealing parameters is expected to improve the molecular arrangement.

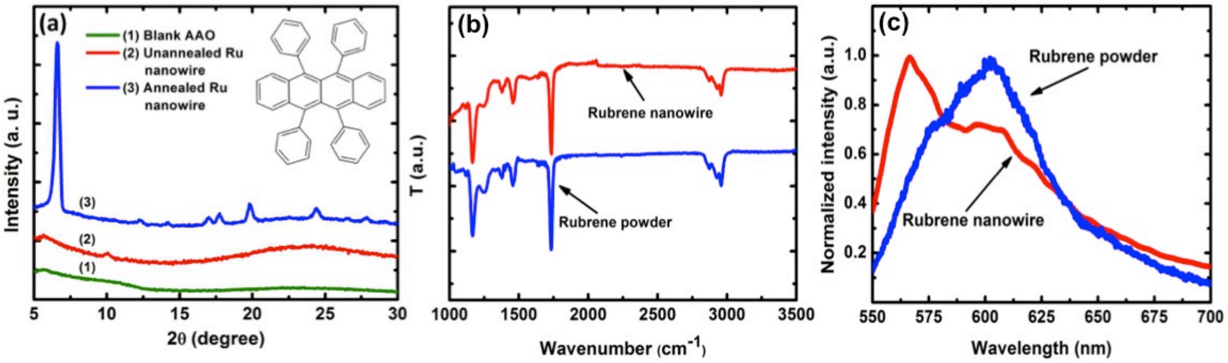

Figure 2.17 (a) XRD spectra of blank AAO, unannealed and annealed rubrene nanowires grown in AAO. (Inset) Molecular structure of rubrene. (b) FTIR transmission spectra for rubrene powder and nanowires in the mid-infrared regime. (c) Photoluminescence spectra for rubrene powder and nanowires. All data were acquired at room temperature.

2.4.2 Fourier Transform Infrared (FTIR) Spectroscopy.

The tips of the organic nanowires near the top-surface of the template are exposed to ambient air and are therefore prone to oxidation [137]. The nanowire tips at the bottom surface are however protected by the host alumina matrix, if the barrier layer is not removed. To examine the bonds in as-grown unoxidized organic nanowires, we have therefore performed attenuated total reflection (ATR) Fourier transform infrared (FTIR) measurements on the nanowire/barrier layer interface (to a depth > 50 nm, much larger than barrier layer thickness (10–30 nm) in the mid-infrared regime and have compared the data with bulk organic powder. To prepare such samples, we protected the top surface of the nanowires by a polymer coating and then the aluminum substrate was dissolved in a mercuric chloride solution. The organic nanowires were never in direct contact with this etchant and effect of such contaminants is therefore minimized in the FTIR response. Figure 2.17 (b) shows the representative results obtained from rubrene nanowires at room temperature. The data has been acquired after subtracting the background response originating from ambient air and host alumina template. For rubrene nanowires, the characteristic peaks have close resemblance with rubrene crystal and powder reported before [138], [139]. The three closely spaced peaks at ~3000 cm^{-1} [Figure 2.17 (b)] are typically associated with C-H bond stretching [138] and are present in both powder and nanowire spectra. The remaining peaks originate from the skeletal vibration of ring [Figure 2.17 (a) inset] and are also present in both spectra.

2.4.3 Photoluminescence (PL) Measurements.

Figure 2.17 (c) shows the photoluminescence (PL) spectrum (excitation wavelength 532 nm) obtained from rubrene nanowires and bulk powder at room temperature. For nanowire samples, the main peak appears at ~570 nm (which corresponds to photon energy of ~2.1 eV and the HOMO-LUMO gap of rubrene) and a shoulder peak occurs at ~600 nm. This agrees well with the PL spectra of single crystal rubrene [89], [137], [139] and organic vapor transport grown nanowire rubrene [89] reported before. For bulk powder, the main peak shifts to a higher wavelength (~600 nm) due to oxidation of rubrene powder [137], [139].

2.5 Characterization Equipments.

The following equipments have been used for the above-mentioned studies:

(a) Atomic Force Microscope (Asylum Research, MFP-3D) was used under ambient conditions with a standard tetrahedral silicon tip (Olympus, OMCLAC160TS- W2) for AFM imaging.

(b) For FESEM imaging of organic nanowire arrays, a JEOL 6301 F field emission scanning electron microscope (10 KV accelerating voltage) has been employed. The organic-filled templates are mounted on SEM stubs using double-sided carbon tapes and coated with chrome before imaging.

(c) XRD has been performed in Rigaku Ultima IV operating at 40KV and 44mA using a copper anode.

(d) FTIR characterization has been done by Thermo scientific Nicolet 8700 with smart speculator.

(e) Photoluminescence studies have been performed using Thermo Nicolet Almega XR Raman Microscope.

Thus the characterization experiments confirm growth of rubrene nanowires within AAO templates. We note that this is the first report of growth of rubrene nanowires within sub-100 nm diameter nanopores. In this chapter we have summarized the key results. Further details are available in ref. [54]. In the next chapter, we will discuss the 4th stage of our research in which we fabricate rubrene nanowire spin valve devices and study their magnetoresistance characteristics.

Chapter 3[*]

Spin Injection and Transport in Rubrene Nanowires.

In this chapter, we describe the fourth stage of our work, which is comprised of spin injection and transport studies in rubrene nanowires. These nanowires have been fabricated using the techniques described in Chapter 2. In fact, for spin transport studies, we have extended this technique to fabricate axially heterostructured metal-organic nanowires. Details are provided below, after a short introduction on organic spin valves.

3.1 Introduction.

As discussed in chapter 1, in an organic spin valve a layer of organic semiconductor is sandwiched between two ferromagnetic electrodes (spin injector and detector). In these devices, organic material acts as the medium for spin transport. In the literature, both lateral and vertical device geometries have been explored [1], [65], [141]. In all of these devices, a (planar) thin film of organic has been used. Reports on organic *nanowire* spin valves are relatively rare due to the complexities involved in the fabrication process. However, nanowire geometry [39], [88] can potentially introduce additional features that are not available for thin films. For example, it has been proposed that a "spin admixture parameter" plays a crucial role in determining the spin relaxation length in organics [68], [69]. The strength of this parameter depends on the growth process and the orientation and packing of organic molecules. It is known that organic nanowires grown in nanoporous anodic aluminum oxide (AAO) template exhibit different molecular packings, which are not observed in organic thin films [54], [89]. Therefore, template-grown organic nanowires are expected to exhibit different spin transport characteristics compared to thin films, which can potentially assist in understanding of the underlying spin transport mechanism. Additionally, a high-density array of vertically standing nanowire spin valves is a versatile architecture since it can be patterned to develop organic-based spintronic memories. In this chapter, we describe the fabrication of a rubrene nanowire spin valve and the results of electrical and spin transport measurements performed on this device [55].

---

[*] Parts of this chapter have been published in ref. [55], [140].

3.2 Synthesis of a Rubrene Nanowire Spin Valve.

We have fabricated an organic (rubrene) nanowire spin valve array consisting of cobalt (Co) nanowire/rubrene nanowire/nickel (Ni) thin film, using a combination of bottom-up electrochemical self-assembly [53], electrodeposition and centrifugation assisted organic growth technique as described in Chapter 2 [54]. The bottom-up electrochemical self-assembly comprises two steps, pretreatment of the aluminum foil by chemical polishing and multistep anodization. These two steps have been extensively described in the previous chapter. After the formation of nanopores, there exists a barrier layer at each pore bottom. This layer needs to be removed for performing further transport experiments.

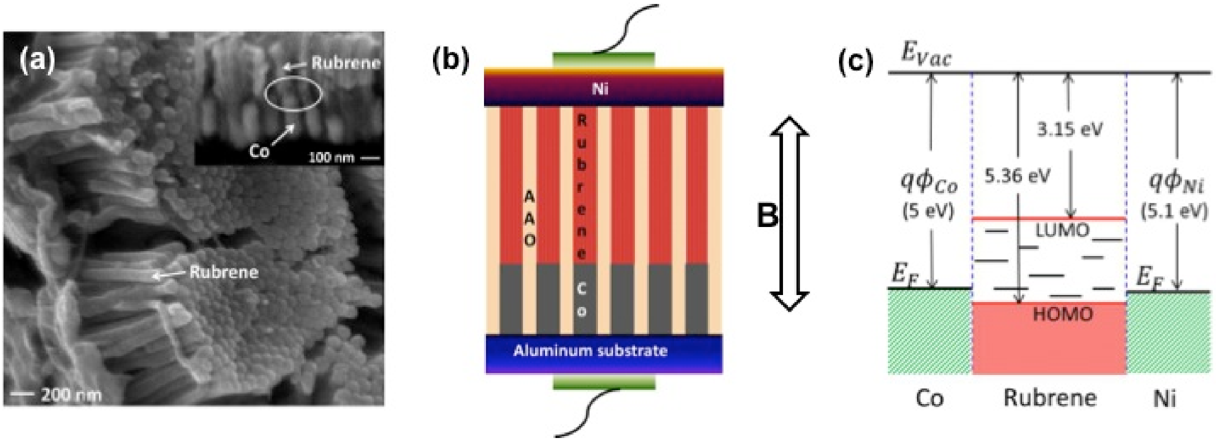

Figure 3.1 (a) FESEM image of rubrene nanowires liberated from the host AAO matrix. (Inset) Co-rubrene nanowire heterojunction. (b) Schematic of the Co-rubrene-Ni spin valve. The magnetic field (B) has been applied parallel to the nanowire axis (easy axis) and perpendicular to the Ni thin film (hard axis). (c) Rigid energy band diagram of the spin valve. Defect states are shown in the HOMO-LUMO gap.

We have removed this barrier layer by a "pore-side etching" technique described in section 2.3. The final pore diameter is 70 nm with a length of 500 nm. Note that we have optimized the anodization parameters to obtain this length. Next, Co is electrodeposited at the bottom of the pores. The electrodeposition time is optimized such that the resulting Co nanowires are ~200 nm in length. For longer deposition times, Co nanowire segments tend to become non-uniform in length with occasional overfilling of the pores. Next, rubrene nanowires (~300 nm length) are grown on top of Co using the centrifugation-assisted technique described in section 2.2. Longer rubrene nanowires do not exhibit any spin valve signal, which is consistent with the transport model described in the next section.

Figure 3.1 (a) shows the cross-sectional field emission scanning electron microscopic (FESEM) image of rubrene nanowires liberated from the host AAO template. The nanowires are solid, long (~300 nm), uniform, and continuous, and hence the possibility of pinhole channels can be excluded. Inset of Figure 3.1 (a) shows the Co-rubrene interface. The top surface of the template is cleaned with acetone to remove any rubrene residues. Finally, Ni is deposited on the top via electron beam evaporation. Gold wires are attached using silver paste to the top Ni and bottom Al, which forms an ohmic contact with the Co nanowires.

Figure 3.1 (b) shows the schematic depiction of the spin valve device. For electrical and magnetoresistance measurements, the host AAO template is kept intact, which also isolates neighboring nanowires and prevents pinhole shorts. The rigid energy band diagram for the spin valve structure is shown in Figure 3.1 (c). In general, trap states exist between the HOMO (highest occupied molecular orbital) and LUMO (lowest unoccupied molecular orbital) levels of rubrene. The trap states located in the vicinity of the Fermi level participate in conduction at low bias [142], [143].

3.3 Electrical and Spin Transport Experiments.

Figures 3.2 (a-d) show magnetoresistance measurements performed on Co nanowire/rubrene nanowire/Ni spin valves at four different temperatures [55]. The magnetic field has been applied parallel to the nanowire axis (easy axis) and perpendicular to the Ni thin film (hard axis). A negative background magnetoresistance (i.e., decreasing device resistance with increasing strength of the external magnetic field) is present in all plots. We note that such background magnetoresistance is a common occurrence in organic spin valves [88] and can have different origins [71], [144], [145]. More importantly, in Figures 3.2 (a-d), we observe positive peaks in the device resistance superimposed on the negative background magnetoresistance. These peaks occur between the coercive fields of top Ni film (~180 G at 8K) and bottom Co nanowire (~1400 G, at 8K), which have been extensively characterized before [146], [147]. Such peaks are the signatures of a “normal spin valve” effect. The coercive field of Co nanowires decreases with increasing temperature.

Figure 3.3 (left) shows the temperature dependence of the coercive field of Co nanowires as determined from the magnetoresistance measurements [Figure 3.2]. Previous studies on transition metal nanowires have demonstrated a linear decrease of coercivity with temperature [147]. The extrapolation from Figure 3.3 (left) yields a coercive field value of 689 G at 295K. We have performed vibrating sample magnetometer (VSM) measurements at room temperature on Co nanowires (embedded in AAO) of similar geometry as in the actual spin valve device. From this measurement, we obtain a coercive field value of 680 G [Figure 3.3 (middle)], which is in good agreement with the extrapolated value obtained from Figure 3.3 (left). We have performed room temperature VSM measurement on a Ni thin film [Figure 3.3 (right)]. The coercive field in this plot is ~170 G, which is slightly smaller than the low-temperature coercive field values (~180 G) obtained from the magnetoresistance measurements [Figure 3.3 (left)]. We note that compared to Co nanowires, the coercive field of top e-beam evaporated Ni thin film has very weak dependence on temperature. The normal spin valve peaks in Figures 3.2 (a-d), together with the control experiments described below, indicate occurrence of spin injection and transport in the rubrene nanowires.

Spin valve effects in rubrene thin films have been reported earlier [37], [142], [143]. To estimate the degree of spin relaxation in these devices, we have used the “modified Julliere formula” (eqn. 4, Chapter 1) and have extracted the lower bound of the spin relaxation length L_S [38], [39]. In the modified Julliere formula, P_1 = 0.33 and P_2 = 0.42 are the tunneling spin polarizations of Ni and Co, respectively [35], d is the length of rubrene nanowire (~300 nm) and $\frac{\Delta R}{R}$ is the spin valve magnetoresistance ratio where ΔR is the height of the spin-valve peak and R is the baseline resistance. From Figures 3.2 (a-d) and using the modified Julliere formula, the spin diffusion length (L_S) in rubrene nanowires is calculated to be ~47.4 nm and ~46.3 nm at 8K and 100K, respectively. These lengths are significantly higher than previously reported values in rubrene thin films [37], [142], [143]. Reference [37] reported this length to be 13.3 nm (0.45K), and using the modified Julliere formula, we have calculated this value to be 5.2 nm (100K) and

~10 nm (10K) from refs. [142] and [143], respectively. Figure 3.2 (e) (bottom inset) shows the temperature dependence of normalized spin-valve magnetoresistance $\frac{\Delta R}{R}$.

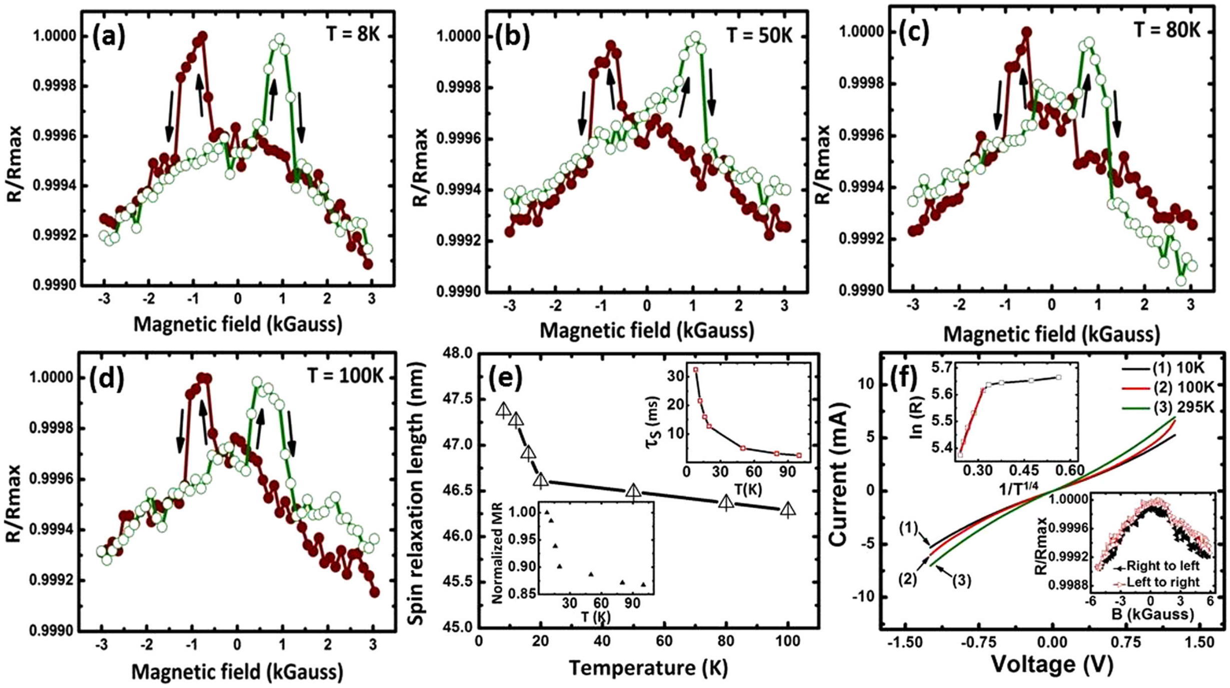

Figure 3.2 (a)–(d) Magnetoresistance of a Co-rubrene nanowire (amorphous)-Ni spin valve at four different temperatures. The spin valve peak height (~150 mΩ) is much larger than the resolution (~1 mΩ) of our measuring device (picotest multimeter). (e) (Bottom inset) Spin valve magnetoresistance vs. temperature. (Main image) Spin relaxation length vs. temperature. (Top inset) Spin relaxation time vs. temperature. (f) Current-voltage characteristics of the spin valve device as a function of temperature. (Top inset) $ln(R)$ vs. $T^{-1/4}$ at 0.5 V. Three-dimensional variable range hopping fit to the high temperature data is shown by the red line. (Bottom inset) Magnetoresistance of Co-rubrene nanowire (annealed)-Ni spin valve.

According to the modified Julliere model, a decrease of magnetoresistance (MR) with temperature indicates two possibilities. First, spin polarizations of the ferromagnetic electrodes can decrease with increasing temperature or second, enhanced spin relaxation occurs (i.e., decreasing L_S) within the organic at higher temperatures. Since the Curie temperatures of Co and Ni are significantly higher than the maximum temperature (100K) in this plot, the latter possibility is more likely. Figure 3.3 (e) (main image) shows the dependence of L_S on temperature (T). We note that rubrene nanowire length (d ~300 nm) is significantly large compared to L_S, which is consistent with the small magnetoresistance values observed in

Figures 3.2 (a-d). The spin valve effect persists up to 100K. We note that the calculated spin relaxation length actually represents a lower bound (discussed previously in Chapter 1), since we have assumed no loss of spin polarization at the ferromagnet-rubrene interface. Figure 3.2 (e) also shows that L_S is almost independent of temperature in the 8K–100K range. This is consistent with other organic semiconductor nanowires [39].

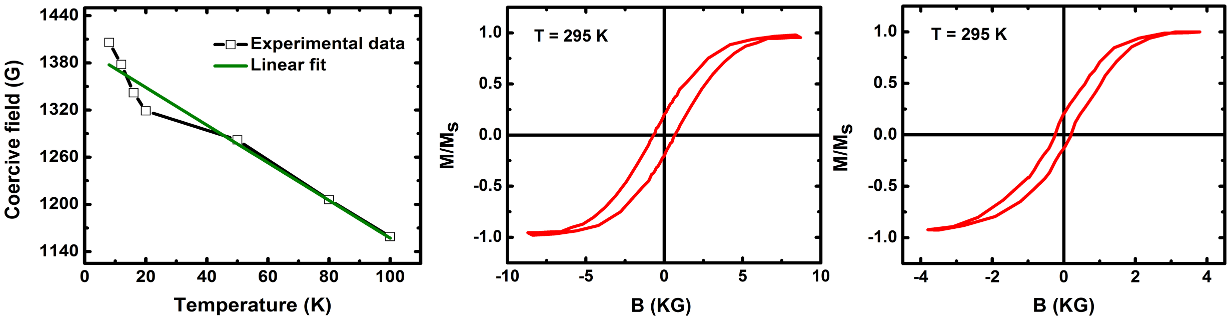

Figure 3.3 (Left) Coercive field of Co nanowire as a function of temperature. (Middle) Room temperature magnetization curve of Co nanowires embedded in AAO. The Co nanowires have same dimensions as the Co contacts in actual spin valve devices. (Right) Room temperature magnetization curve of e-beam evaporated Ni thin film.

We have performed an order-of-magnitude estimate of the spin relaxation time (τ_S) from L_S calculated above and available mobility data of amorphous rubrene (μ ~10^{-6} cm^2 /Vs) [37], [148]. Figure 3.2 (e) (top inset) shows τ_S as a function of temperature (T). Spin relaxation time and lengths are related through the equation, $\tau_S = eL_S^2 / k_B T \mu$ [39]. Since mobility is expected to be even smaller at lower temperatures, we find $\tau_S > 2.5$ ms at 100K. Such extremely long spin relaxation time makes amorphous rubrene nanowire a promising platform for implementing a classical single spin logic paradigm.

Current-voltage (I–V) characteristics of rubrene nanowire spin valves are shown in Figure 3.2 (f). The characteristics are symmetric in the bias range [−1.25, 1.25 V] and do not show any rectification effect. This can be attributed to similar coupling with the top and bottom contacts [Figure 3.1 (c)]. The I–V characteristics are non-linear and device resistance [$R=(dI/dV)^{-1}$] decreases as the temperature is increased. This indicates that the organic nanowires have a nonmetallic behavior and, combined with the disordered nature of these systems [Fig. 2.4 (a)], suggests hopping as the dominant transport mechanism [54], [149]. The top inset of Figure 3.2 (f) shows that *ln*(*R*) vs. $T^{-1/4}$ plot is linear at higher temperature and low bias, which indicates Mott's three-dimensional variable range hopping is the appropriate transport model in this regime [37], [54], [149]. At lower temperature (< 80K), thermal energy fails to sustain hopping and resistance tends to saturate in this temperature regime. Tunneling between molecular states is likely the dominant conduction mechanism in this range [54]. The trap states of the host amorphous alumina template are also known to influence the temperature-dependence of the nanowire transport characteristics [150]. Non-linearity in the *I–V* characteristics at high bias [Figure 3.2 (f)] often occurs in organic systems and is a signature of electric field induced hopping [54], [149]. The observed non-linearity and temperature dependence of *I–V* characteristics imply the absence of metallic pinhole shorts through the organic.

3.4 Control Experiments.

To confirm that the spin valve peaks observed in our devices [Figures 3.2 (a-d)] are not due to any artifact such as anisotropic magnetoresistance (AMR) of the contacts or local Hall effect due to stray magnetic fields from the contacts [151], we have performed four control experiments. Figures 3.4 (a-d) illustrate representative MR responses for (a) Co nanowire/Ni thin film, (b) Co nanowire/rubrene nanowire/Ag thin film, (c) Ag nanowire/rubrene nanowire/Ni thin film, and (d) Al/rubrene nanowire/Ag thin film, respectively. No spin valve peak was observed for any of these control samples. In control sample (a), typical AMR response is observed, which is consistent with previous works [71], [88], [152]. As expected, linear *I–V* curve with metallic temperature dependence has been found in this case (not shown). Also, resistance of this control sample is several orders of magnitude smaller than for the spin valve samples due to the absence of the rubrene layer. Thus, Figures 3.2 (a-d) cannot be explained by invoking AMR of the contacts. Control samples (b) and (c) contain rubrene nanowire and only one ferromagnetic contact. These samples have not shown any spin valve peaks, indicating that the MR peaks in Figures 3.2 (a-d) do not originate from the fringe magnetic fields of the ferromagnetic contacts [151]. However, these samples exhibit a background MR very similar to Figures 3.2 (a-d), which can originate from the fringe fields or the organic magnetoresistance (OMAR) of rubrene. Finally, control sample (d), which does not contain any ferromagnetic contact, also exhibits a very similar negative background MR without any spin valve signal. Thus, we infer that the background MR observed in Figures 3.2 (a-d) and Figures 3.4 (a-d) originates from rubrene and represents the so-called OMAR effect [153]. All rubrene-containing control samples exhibit nonlinear *I–V* characteristics (not shown), nominally identical to the spin valve devices [Figure 3.2 (f)]. It is well known that OMAR is a characteristic of bulk transport (instead of interface effect) [153]. Presence of OMAR in our samples provides additional evidence that transport is not dominated by the metal-organic interfaces. Similar negative background magnetoresistance has been observed before in rubrene single crystals [144] and thin films [145].

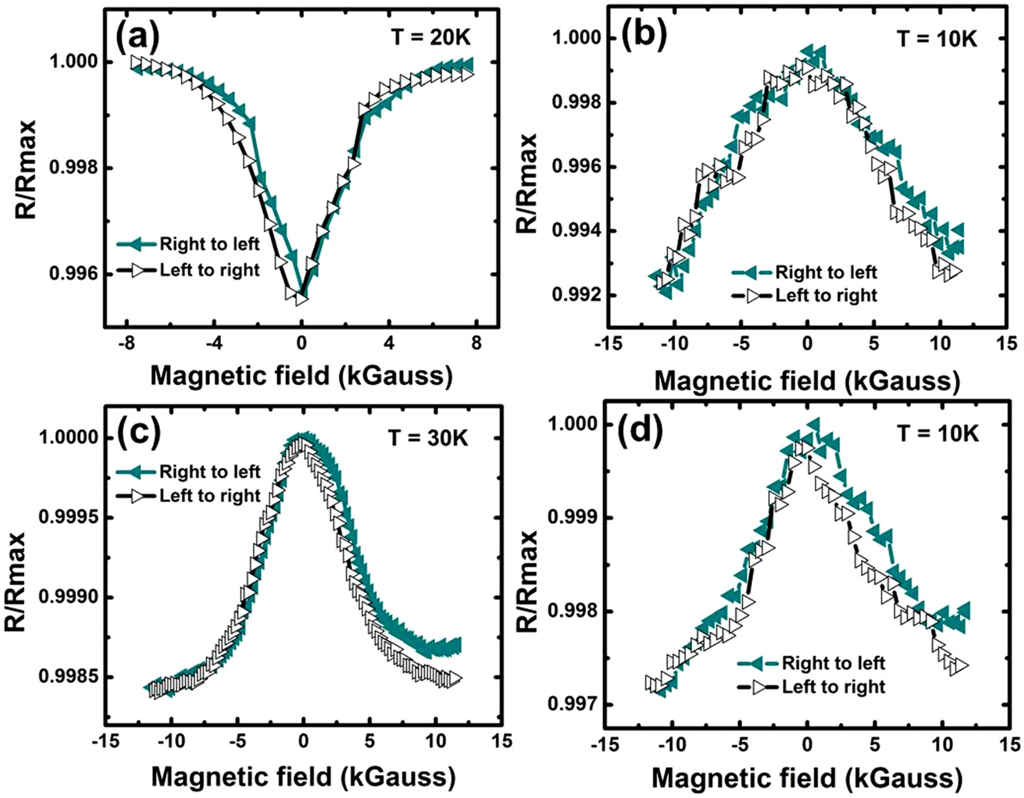

Figure 3.4 Magnetoresistance measurements on four control samples: (a) Co nanowire-Ni thin film, (b) Co nanowire-rubrene nanowire-Ag thin film, (c) Ag nanowire-rubrene nanowire-Ni thin film, and (d) Al-rubrene nanowire-Ag thin film.

3.5 High-Field Magnetoresistance Effects.

Fig. 3.5 shows the high field magnetoresistance (MR) effect in rubrene nanowire spin valves at four different temperatures. In all cases, a negative background MR is observed at high fields (-1 – 1T range). At low temperatures, a low-field spin valve response (similar to Fig. 3.2 a-d) is superimposed on this negative background MR. Similar high field negative MR has been reported before in rubrene single crystals [144]. This effect was found to decrease rapidly with increasing temperature and vanish beyond 200K [144]. Based on this observation, the negative MR was attributed to "weak localization" effects [144]. However, the background MR effect observed in our experiments is significantly different than that reported in Ref. [144] because of two reasons: (a) our negative background MR is relatively insensitive to temperature and persists even up to room temperature (Fig. 3.5), and (b) our negative background MR shows sign of saturation at ~1T (maximum value of magnetic field that can be applied using our experimental set up) as shown in Fig. 3.5. Thus, we believe that weak localization is not the physical mechanism behind the high-field background MR observed in our rubrene nanowires.

The high field MR effect in Fig. 3.5 cannot be attributed to artifacts such as anisotropic magnetoresistance (AMR) of the ferromagnetic contacts or the "local Hall effect" due to the fringing fields of the ferromagnetic contacts. Details of these control experiments have been discussed in the last section, and the observed MR has been confirmed to originate from the rubrene nanowire spacer itself.

Background MR effects have been reported before in Alq_3 nanowire samples [39], [71], [88]. In the case of Alq_3 nanowires, a correlation has been observed between the signs of the spin valve signal and the background MR. Such effects can be explained qualitatively if one assumes a magnetic field dependent spin relaxation length and that spin-orbit interaction is the dominant mode of spin relaxation [71]. No such correlation effect has been observed in the case of rubrene nanowires. We only observe a positive spin valve effect with a negative high field background MR (Fig. 3.5).

Further, persistence of the background MR effect in higher temperature regimes (>100K) where the spin valve signal is absent (Figs. 3.5 c-d) indicates that the background MR is not related to spin injection and spin-polarized transport. Thus, based on above discussions it appears that "organic magnetoresistance" (OMAR) is the likely origin of the background high-field MR in our rubrene nanowires.

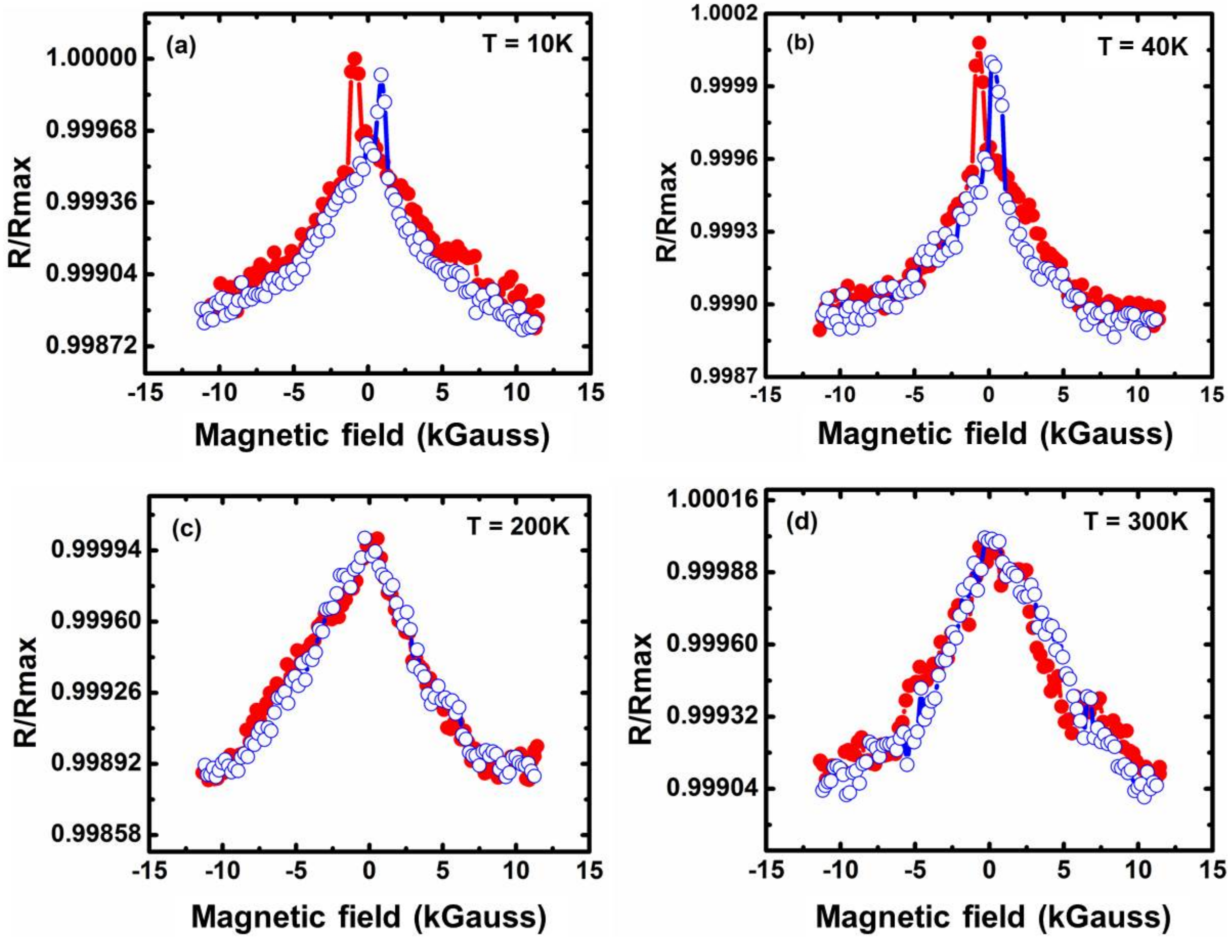

Figure 3.5 High field magnetoresistance of rubrene nanowire spin valves at four different temperatures, (a) 10 K, (b) 40K, (c) 200K, and (d) 300K. Open (closed) symbols indicate field scan from left-to-right i.e. -1T to 1T (right-to-left, 1T to -1T). The spin valve peak height (~150 mΩ) is much larger than the resolution (~1 mΩ) of our measuring device (picotest multimeter).

3.6 Possible Spin Relaxation Mechanism.

Based on our experimental data, we speculate on the dominant spin relaxation mechanism in rubrene nanowires. In organics, spin-orbit interaction (SOI) and hyperfine coupling (HC) with nuclei are typically the two main spin relaxation mechanisms, and the relative importance of SOI and HC varies significantly between organics [67], [154]. Experimental identification of the dominant mechanism relies on the qualitatively different temperature, electric field, and magnetic field dependence of L_S between these processes [154]. For rubrene nanowires, the decrease of L_S with temperature [Figure 3.2 (e)] suggests dominance of SOI since HC predicts an opposite temperature-dependence of L_S [68], [69]. This is because, at elevated temperatures, the effective hyperfine magnetic field weakens due to depolarization of the nuclear spin system [71], [154]. Further, the hopping frequency increases at higher temperature, leading to shorter waiting times at the molecular sites and hence reduced spin precession [155]. Saturation of L_S at high temperature and gradual increase at lower temperature [Figure 3.2 (e)] is very similar to that observed in Alq_3 [39], [41], and this feature has recently been quantitatively explained by a theoretical framework in which SOI plays the dominant role [68], [69]. If SOI is dominant, the spin relaxation length should be given by $L_S(T) = \hat{R}(T)/4\gamma$ [68], [69] , where $\hat{R}(T)$ is the average hopping distance and γ is the "spin admixture parameter." The admixture parameter determines the amount of "mixing" between spin-up and spin-down states (generally defined by the external magnetic field in a spin valve experiment) and is a function of atomic SOI, π-σ energy splitting, and the spatial orientation of the molecular orbitals [68], [69]. The orientation of the molecular orbitals depends on molecular packing, which is highly sensitive to the organic growth process. Atomic SOI and π-σ energy splitting are intrinsic properties of the organic material. The significantly higher L_S found in amorphous rubrene nanowires compared to thin films [37], [142], [143] indicates the key role of the spin admixture parameter γ, since $\hat{R}$ can only be worse in solution-grown highly amorphous specimens compared to vacuum deposited thin films [37], [142], [143]. We have also performed spin valve measurements on annealed rubrene nanowires, which exhibit a higher degree of crystallinity [Figure 2.4 (a)] and possibly higher $\hat{R}$. Interestingly, no spin valve signal has been observed in this case [Figure 3.2 (f), bottom inset), which can be attributed to the large γ in this sample. This is consistent with refs. [144], [156], which did not observe any spin valve signal in high mobility single crystal rubrene. We note that L_S is almost an order of magnitude higher in rubrene nanowires compared to Alq_3 nanowires [39]. This is consistent with refs. [68] and [69], which estimated γ to be significantly stronger in Alq_3 molecules. Therefore, our spin transport measurements indicate the crucial role of molecular packing, which affects the spin admixture parameter, on spin relaxation. Such structural tunability of spin relaxation is a unique feature of organic materials.

3.7 Temperature Dependence of Spin Relaxation Length.

The temperature-dependence of spin relaxation length (L_S) of rubrene nanowires is shown in Fig. 3.2 (e). As described in the previous section, the decrease of L_S with increasing temperature (T)

implies SOI as the dominant spin relaxation mechanism, since in the case of HC, one would expect an opposite trend [55]. A recent theoretical work [69] based on SOI has derived the expression of L_S as a function of hopping distance ($\hat{R}$) and spin admixture parameter (γ) as mentioned in the previous section.

Compared to previous works, long L_S found in our nanowire devices, in spite of a high degree of amorphousness and hence low hopping distance, indicates the crucial role of spin admixture parameter γ on spin relaxation. The parameter γ critically depends on the growth condition [55].

We notice from Fig. 3.2 (e) that there is a step-like increase in L_S below 20K. The origin of this feature is unlikely to be related to the surface spin polarization of the ferromagnetic electrodes [157]. In our device, we have used Co and Ni which have very high Curie temperatures (1388K for Co and 627K for Ni). Thus, negligible variation in spin injection efficiency is expected within this low and narrow temperature range. A similar step-like jump of L_S was also observed in Alq_3 below 40K [41]. No conclusion was made about the mechanism behind this observation [41]. However, the SOI-based physical picture mentioned above offers a qualitative explanation of this effect. In disordered systems below a critical temperature, strong Coulomb interaction between localized electrons creates a gap near the Fermi level [158]. This gap results in a new temperature dependence of hopping conductivity, and Mott's hopping law is modified in this regime [158]. Within the framework of Mott's law, hopping distance $\hat{R}$ is related to temperature as $\hat{R} \sim T^{-1/4}$ and in the strong Coulomb interaction case it is modified to $\hat{R} \sim T^{-1/2}$ [69]. According to the relation $L_S(T) = \hat{R}(T)/4\gamma$ mentioned before, temperature-dependence of the spin relaxation length solely depends on $\hat{R}(T)$ since γ is associated with the growth process and is relatively temperature-independent. Based on these considerations, variation of L_S with temperature is expected to be faster in the strong Coulomb interaction regime (at low temperature) and comparatively slower in the weak interaction regime (above the critical temperature). This is exactly what we observe for rubrene nanowires.

3.8 Characterization Equipments.

A model 642 electromagnet power supply and Cryotronics 332 Controller from Lake Shore have been used as electromagnet current source and temperature controller, respectively. A picotest

M3500 multimeter has been used to extract directly the resistance of the device. Each resistance value is the average of 50 readings. A 475DSP gauss meter has been used to record the magnetic field values. All equipments have been synchronized by LabView VI for data acquisition.

In the fourth stage of our work, we have demonstrated the spin valve effect in amorphous rubrene nanowires. Significant improvement in spin relaxation length has been observed compared to the previously reported vacuum-deposited rubrene thin films. Spin-orbit interaction appears to be the most likely agent for spin relaxation. Improved crystallinity has been found to enhance spin relaxation. This indicates the crucial role of molecular packing, which affects the spin admixture parameter. Such structural tunability of spin relaxation is a unique feature of organic materials.

Chapter 4[*]

Fabrication and Characterization of ssDNA-SWCNT Hybrid Nanotube Devices

In the previous chapters we have demonstrated the feasibility of spin injection and transport in organic semiconductor rubrene and the potential advantages of nanowire geometry. In these studies, organic nanowires were used as the transport channel for spin-polarized charge carriers. We used ferromagnetic contacts (such as Ni, Co) as the injector (and detector) of spin-polarized carriers. Now, we focus on another feature of organic spintronics in which organic-based materials can act as spin injector or detector. It has been suggested by a few groups [50]–[52] that certain organic-based systems can perform as efficient spin filters (i.e. spin injectors and detectors). Very few experimental studies exist in this area, and in the present part of this thesis (Chapter 4 and 5) we aim to explore this aspect of organic spintronics. Our material of choice is single wall carbon nanotubes (SWCNT) that are helically wrapped by single stranded deoxyribonucleic acid (ssDNA) molecules. Recent theoretical work [52] has shown that this system has the potential to act as a spin filter. However, no experimental work has been reported to date on this system. Here we report fabrication, characterization and spin transport experiments in ssDNA-SWCNT hybrid nanotube devices. In this chapter, we discuss the fifth stage of our work which is the fabrication and characterization of ssDNA-SWCNT hybrid nanotubes. Spin transport measurements will be the subject of discussion of Chapter 5 as the sixth and final stage of our work.

4.1 Introduction.

Carbon based materials show great promise for applications both in industry and academia. One distinguishing feature of carbon among other group IV elements in the Periodic Table is that it can participate in either sp^2 or sp^3 bond configurations and can form a variety of phases, such as diamond, graphite, and fullerenes [159]. Since the discovery of carbon nanotubes (CNT) in 1991 [160], they have attracted significant scientific and technological interest owing to their

---

[*] Parts of this chapter will be submitted for publication as a journal article.

promising electronic, optical, chemical and mechanical properties [159]. Beside numerous potential applications in nanoelectronics and sensing, CNTs provide an ideal model system to study the electrical transport properties of one-dimensional nanostructures and molecules [161], [162].

Despite the huge potential of these quasi one dimensional structures, efficient dispersion of CNT bundles and directed assembly of CNTs have been difficult tasks mainly due to their poor solubility in both aqueous and nonaqueous solutions. Zheng and coworkers reported an efficient method of dispersion of single wall carbon nanotube (SWCNT) bundles in aqueous solution by ultrasonication in the presence of single stranded deoxyribonucleic acid (ssDNA) [163], [164]. This method separates the individual CNTs from as-grown bundles and cuts them into short tubes. Subsequently, they have also demonstrated the feasibility of separation of metallic and semiconducting tubes by ion exchange chromatography, utilizing the fact that DNA imparts negative charge to the DNA-SWCNT hybrid [163], [164]. Efficient dispersion of CNTs is an important step towards building any functional device, but directed assembly or alignment of them is even more desirable. McLean and co-workers have shown the parallel alignment of ssDNA wrapped SWCNTs on SiO_2 substrate modified with hydrophobic organosilane films [165]. Hopkins and co-workers have reported another method of alignment of CNTs [166]. They have utilized a modified inkjet printer as a tool for direct printing and alignment of CNTs. Khripin et. al. have used a meniscus alignment method, also called molecular combing, for the directed assembly of DNA-SWCNT hybrids [167]. Here, we show that unlike ref. [165], DNA wrapped CNTs self-assemble on SiO_2 in parallel alignment without any surface modification.

DNA wrapped (functionalized) CNTs have application in separating metallic nanotubes from semiconducting nanotubes as mentioned earlier [163], [164]. These hybrid supramolecular complexes also have applications in diverse areas such as biological transporters and biosensors [168], fibers for artificial muscles [169], bioelectrodes for fuel cells [170], ultrafast detection of DNA hybridization [171]–[173], electrochemical sensing [174], polymerization of conducting polymer composites [175] and single molecule charge transport [176].

4.2 Synthesis of Aligned DNA-SWCNT Hybrid Nanotubes.

We have used the recipe of Zheng and co-workers to disperse bundled SWCNTs [163], [164]. We mixed 1mg of as-produced HiPCO (high-pressure carbon monoxide) nanotube (Carbon Nanotechnologies) with 1ml aqueous ssDNA (Integrated DNA Technologies) solution that contains nuclease free water and a buffer solution (EDTA) to maintain pH. The mixture solution was kept in an ice-water bath and probe-ultrasonicated (Sonics, VC 130 PB) for 90 minutes at a power level of 8W. After sonication the samples were centrifuged for 60 minutes at 14000g in order to remove the insoluble material. The top part of the solution after centrifugation was separated for further analysis.

Figure 4.1 shows the SEM image of as-produced CNT bundles. These ropes are very long and in bundles which prevent them from being useful for any CNT-based device. Figure 4.2 shows the SEM image of dispersed DNA wrapped CNTs on a Si surface. Successful separation and cutting is possible only when an appropriate amount of DNA is mixed with HiPCO CNTs as described in the last paragraph. We have tried to use smaller amounts of DNA and observed a poor dispersion efficiency. Figure 4.3 shows the SEM image of dispersed CNTs with a smaller amount of DNA. The individual CNTs are not separated in this case and the tubes are not cut into small pieces compared to Figure 4.2. In Figure 4.2 we see that despite good dispersion, the DNA-SWCNT hybrids are not aligned on bare Si substrate. We have used single stranded DNA, $d(GT)_{15}$ which has 30 alternating G and T bases. This sequence, according to reference [164], causes the most efficient dispersion.

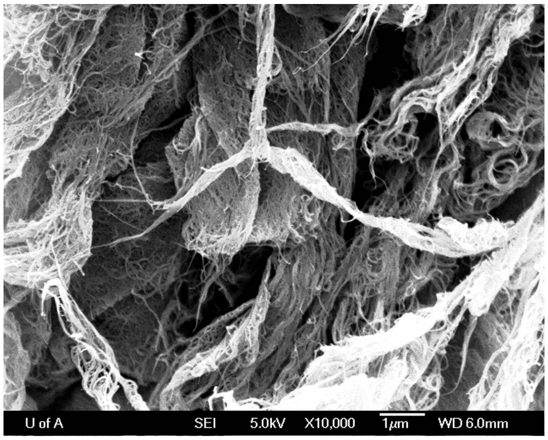

Figure 4.1 Scanning electron microscope (SEM) image of as-produced single wall carbon nanotube bundles.

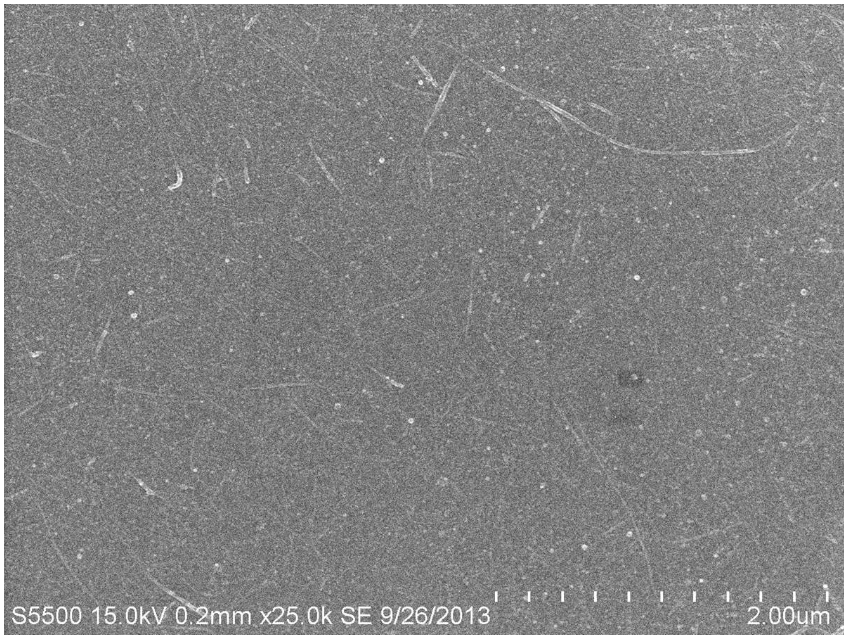

Figure 4.2 Scanning electron microscope (SEM) image of ssDNA-wrapped dispersed single wall carbon nanotubes on a bare Si substrate.

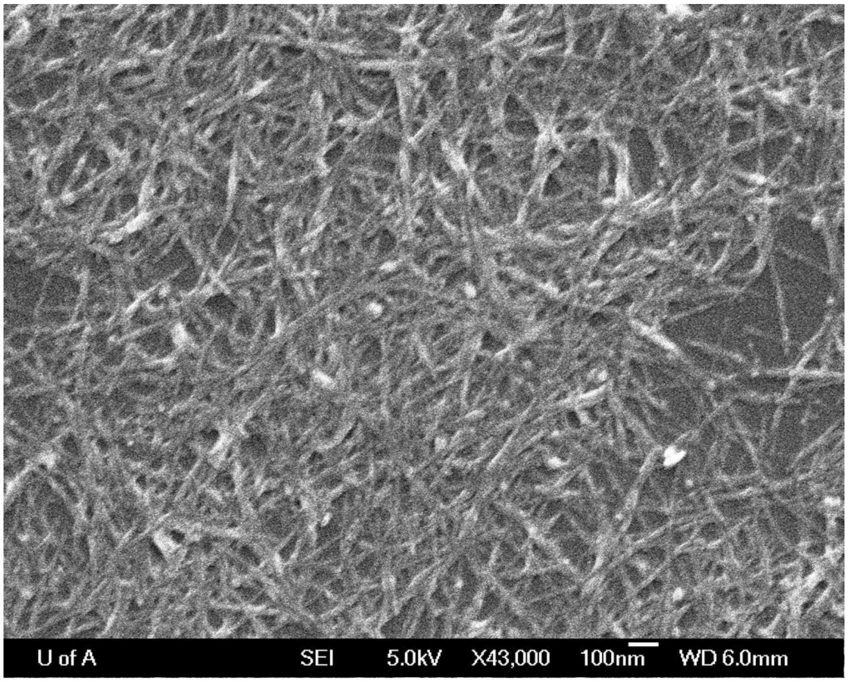

Figure 4.3 Scanning electron microscope (SEM) image of ssDNA-wrapped poorly dispersed single wall carbon nanotubes on a bare Si substrate.

As mentioned in the introduction section there are few reports regarding the alignment of ssDNA-wrapped SWCNTs [165]–[167]. Unlike previous works, we have observed a spontaneous alignment of these hybrids on bare SiO_2. This finding is very important as it eases the realization of many devices made from these hybrids such as field effect transistors (FET). Figures 4.4 and 4.5 show atomic force microscope (AFM) images of aligned ssDNA-SWCNTs on a bare SiO_2 substrate. We have dropped the solution containing these hybrids on the SiO_2 surface and rinsed and dried after 20 minutes (Figure 4.4) and 10 minutes (Figure 4.5). A clear difference in ssDNA-SWCNT amount is visible from these figures consistent with previously reported data [165].

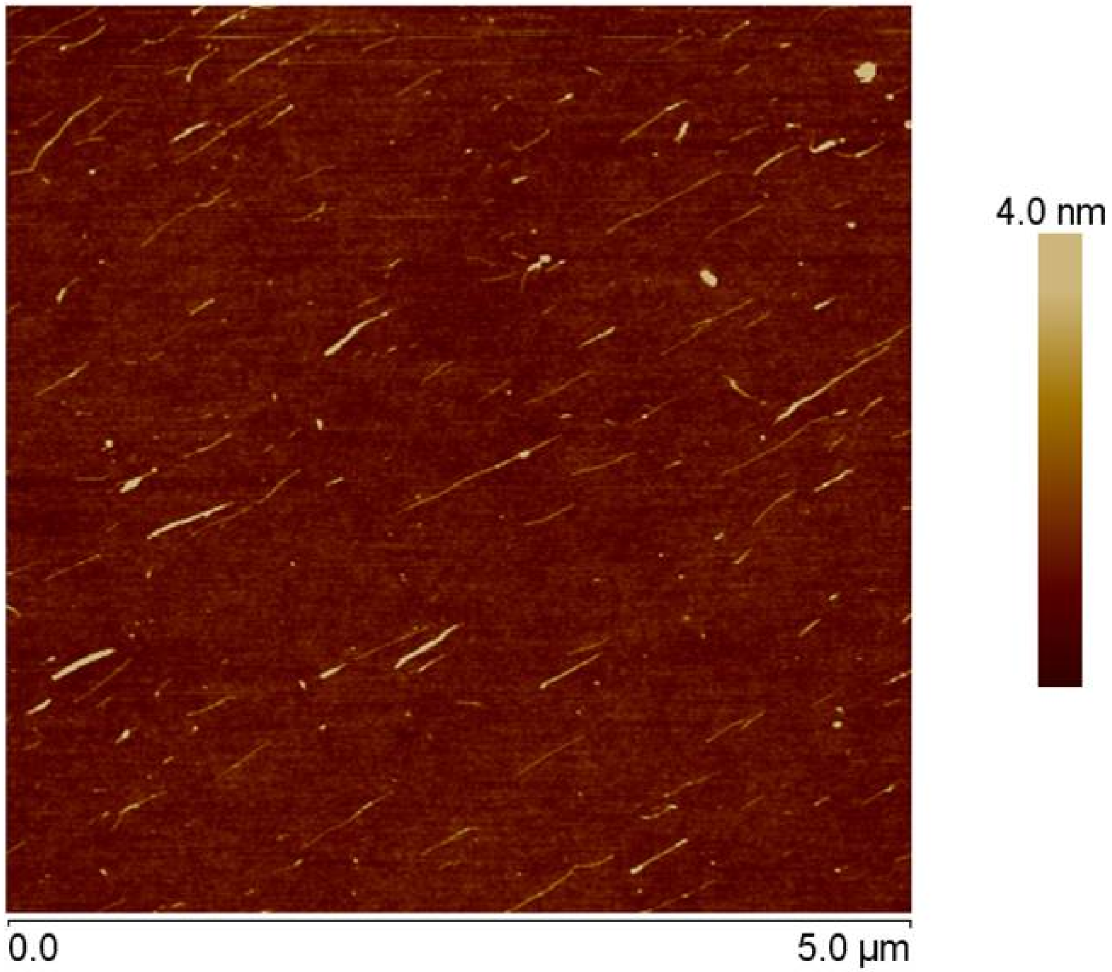

Figure 4.4 Atomic force microscope (AFM) image of ssDNA-wrapped single wall carbon nanotubes on a bare SiO_2 substrate. The deposition time is 20 minutes.

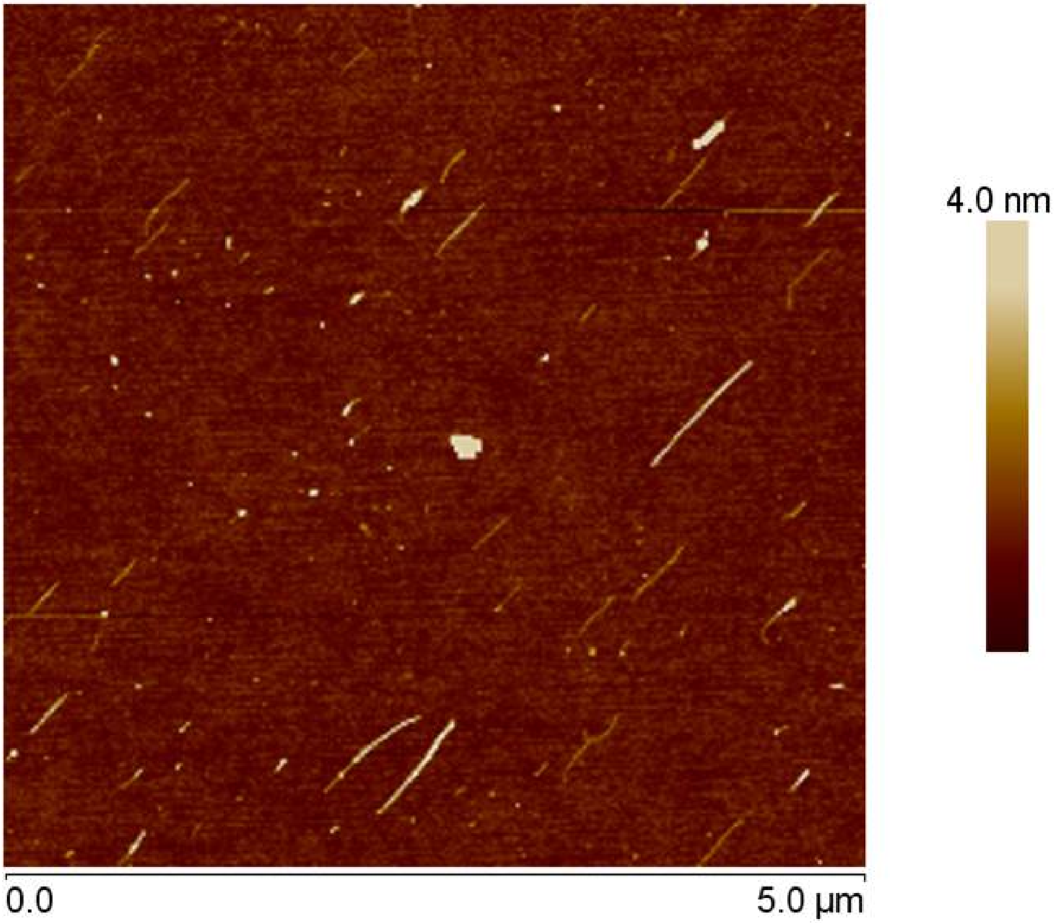

Figure 4.5 Atomic force microscope (AFM) image of ssDNA-wrapped single wall carbon nanotubes on a bare SiO_2 substrate. The deposition time is 10 minutes. Smaller number of tubes are present as compared to Figure 4.4.

The CNTs are wrapped by ssDNA when the aromatic hydrophobic DNA bases interact with the sidewall of CNT via π-stacking and the hydrophilic sugar-phosphate backbone of the DNA strand is left exposed to interact with the aqueous solvent [163]. Flexibility allows the molecule to find low energy conformations that maximize base-nanotube stacking and results in helical wrapping with right or left-handed turns. The ssDNA chains forms a shell encasing the nanotube while keeping the hydrophilic sugar-phosphate backbone on the exterior side [163]. Figure 4.6 shows the AFM image of a single ssDNA-SWCNT hybrid. This hybrid nanotube is approximately 800 nm long.

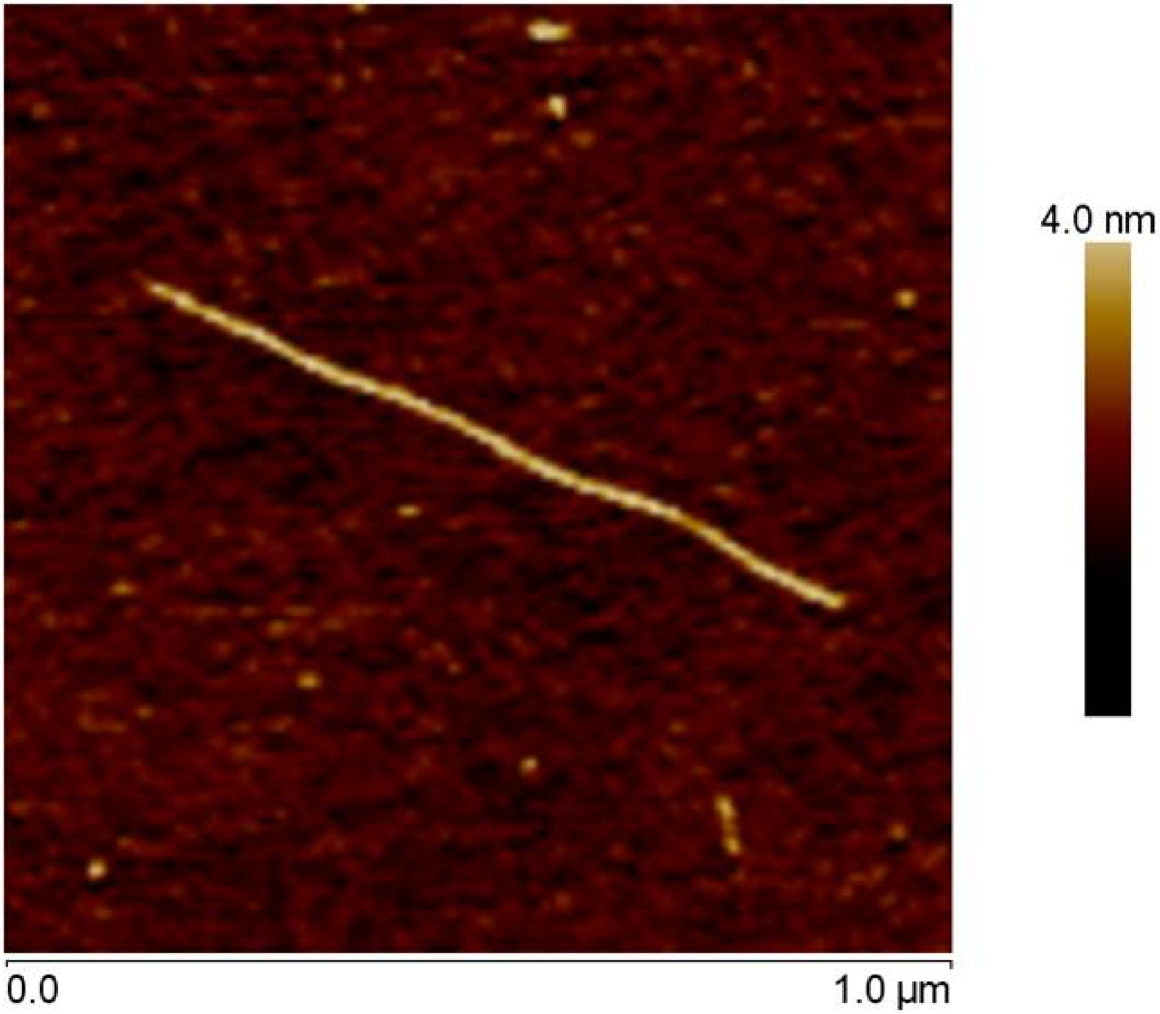

Figure 4.6 Atomic force microscope (AFM) image of a single DNA-wrapped single wall carbon nanotube on a bare SiO_2 substrate. The length of this hybrid nanotube is ~800 nm.

4.3 Characterization of ssDNA-SWCNT Hybrid Nanotubes.

Prior to conducting the magnetotransport measurements, few characterization experiments have been performed on ssDNA-SWCNT hybrid nanotubes. These experiments shed light on the electrical and optical properties of the ssDNA-SWCNT hybrids compared to the pristine CNTs. We have performed Raman spectroscopy and photoluminescence (PL) measurements. The ensuing sections have detailed these experiments.

4.3.1 Raman Spectroscopy.

Raman spectroscopy with excitation wavelength of 532 nm has been used to probe the pristine CNTs and ssDNA-SWCNT hybrids. After centrifugation (section 4.2), we have divided the top clean part of the ssDNA-SWCNT solution into two fractions. We have focused on both radial breathing mode (RBM) and tangential mode (TM). RBM band determines tube diameter distribution [177]–[179]. The TM band is split into two components, G^+ and G^-, at higher and lower frequencies respectively [179].

Figure 4.7 shows the RBM bands of as-produced and two fractions of DNA wrapped SWCNTs. Both fractions of DNA-SWCNT hybrids have upshifted RBM frequencies, a typical signature of DNA wrapping, consistent with previously found results [177]–[179]. The upshifted RBM bands for fraction 1 (Figure 4.7, b) have almost similar diameter selectivity as that of pristine CNTs (Figure 4.7, a). On the other hand, upshifted RBM bands for fraction 2 (Figure 4.7, c) have smaller diameter selectivity as RBM frequency is inversely proportional to diameter. We see that the alternating sequence of guanine (G) and thymine (T) DNA efficiently wraps HiPCO nanotubes over a wide range of diameters.

Figure 4.8 shows the G band feature (TM) of as-produced and two fractions of DNA wrapped SWCNTs. These fractions are the same as before. We see that all three bands have two components (peaks). The G^+ peak at higher frequency is generally ascribed to the vibrations of carbon atoms along the tube axis and G^- peak at lower frequency is due to the circumferential vibrations [178], [180], [181]. The high frequency component is ubiquitous in carbon based materials including single wall CNTs, multiwall CNTs, graphene and graphite, but the low frequency component is a distinct feature of SWCNTs, which arises due to curvature and confinement [181]. The relative intensities of G^- to G^+ band are reduced after DNA wrapping for both fractions (Figure 4.8). The calculated relative intensity for pristine CNTs is 0.67, while for fractions 1 and 2, these numbers are 0.54 and 0.63, respectively. This intensity reduction is a common feature of the ssDNA-SWCNT hybrid and implies suppression of vibrations of carbon atoms along the circumference direction [178]. From Figure 4.8 we notice that the G^+ peaks for both fractions have upshifted (1590 and 1587 cm^{-1} for fractions 1 and 2 respectively) after wrapping. G^+ peak position for the pristine CNTs was 1580 cm^{-1}. This was attributed to the fact that nanotube transfers charge to the DNA molecule [181]. When the charge transfer occurs in the opposite direction, this peak is downshifted [178], [181]. The width of the G^+ band is almost unchanged for fraction 1, but reduced for fraction 2. Wrapping induced width reduction of the G^+ band has also been reported in previous experiments [178], [182].

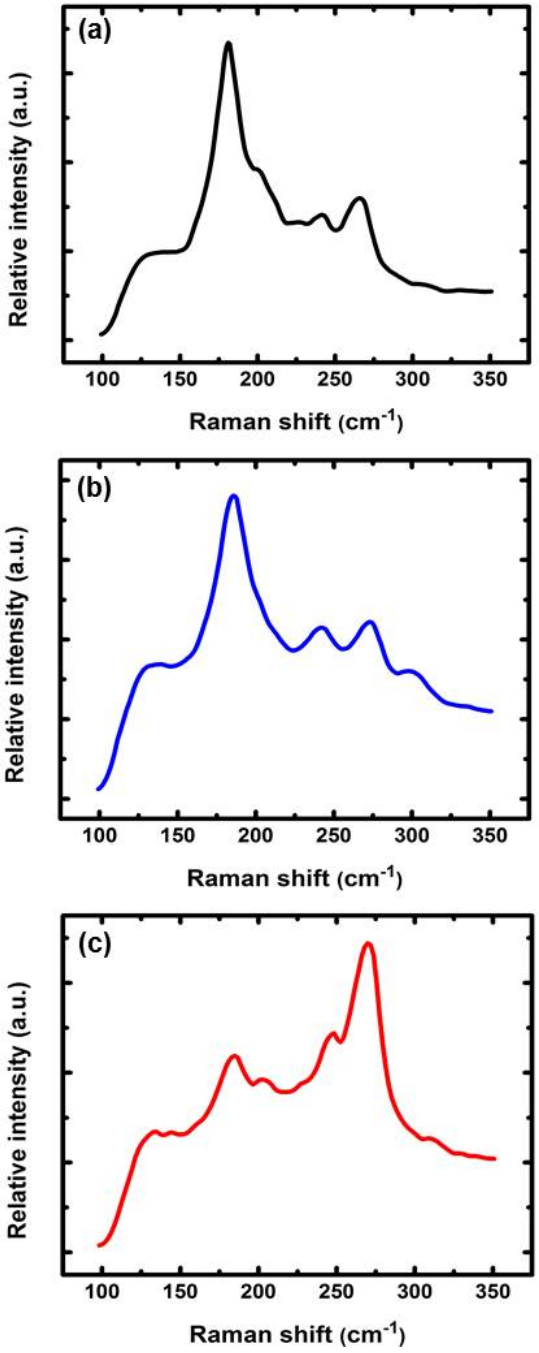

Figure 4.7 Radial breathing modes (RBM) in Raman spectra for (a) as-produced SWCNTs and (b), (c) DNA wrapped SWCNTs for fractions 1 and 2, respectively.

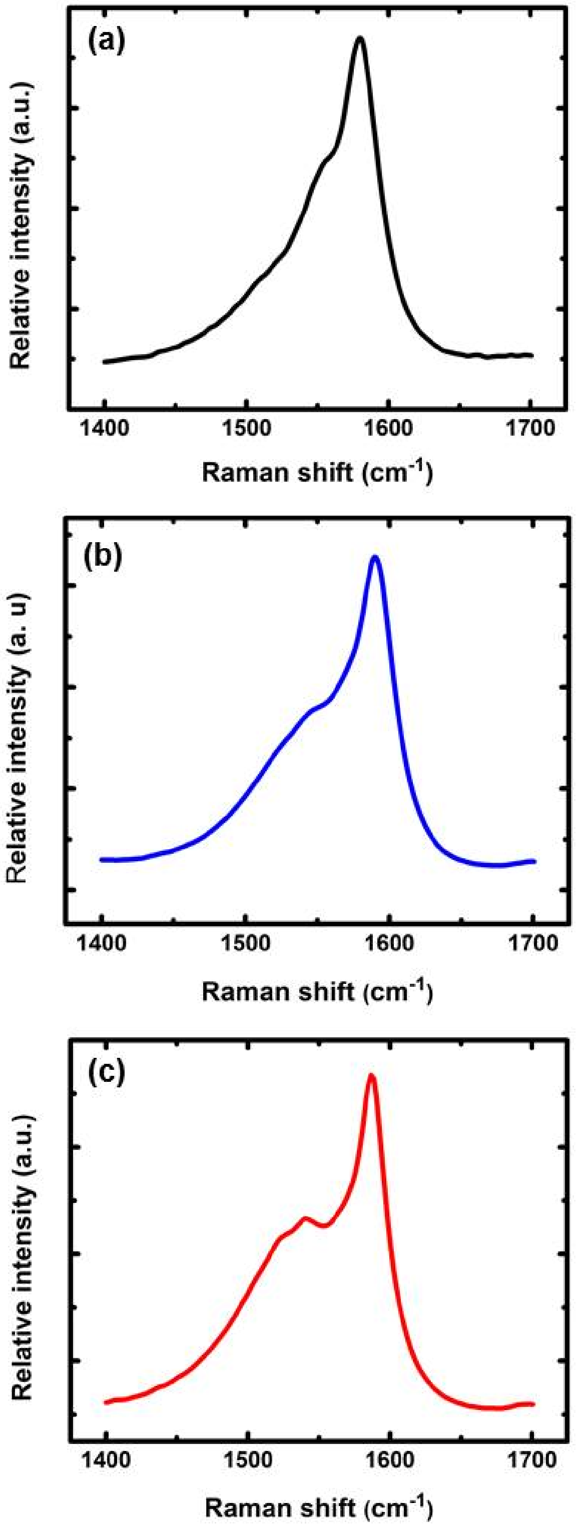

Figure 4.8 Tangential modes (TM) in Raman spectra for (a) as-produced SWCNTs and (b), (c) DNA wrapped SWCNTs for fractions 1 and 2, respectively.

4.3.2 Photoluminescence (PL) Measurements.

Figure 4.9 shows the photoluminescence (PL) spectrum (excitation wavelength 532 nm) obtained from as-produced CNTs and ssDNA wrapped CNTs at room temperature. No PL signal can be found for as-produced CNTs, but strong signal is observed for DNA wrapped CNTs, consistent with previously reported data [183], [184]. Each peak in the PL spectrum originates from a specific nanotube diameter. From Figure 4.9 it is evident that d(GT)$_{15}$ which is a short single stranded DNA has good diameter selectivity. Similar diameter selectivity was also found in reference [183] for short single stranded DNA. Along with AFM and SEM images and Raman spectroscopy, these PL signals confirm efficient DNA wrapping around SWCNTs.

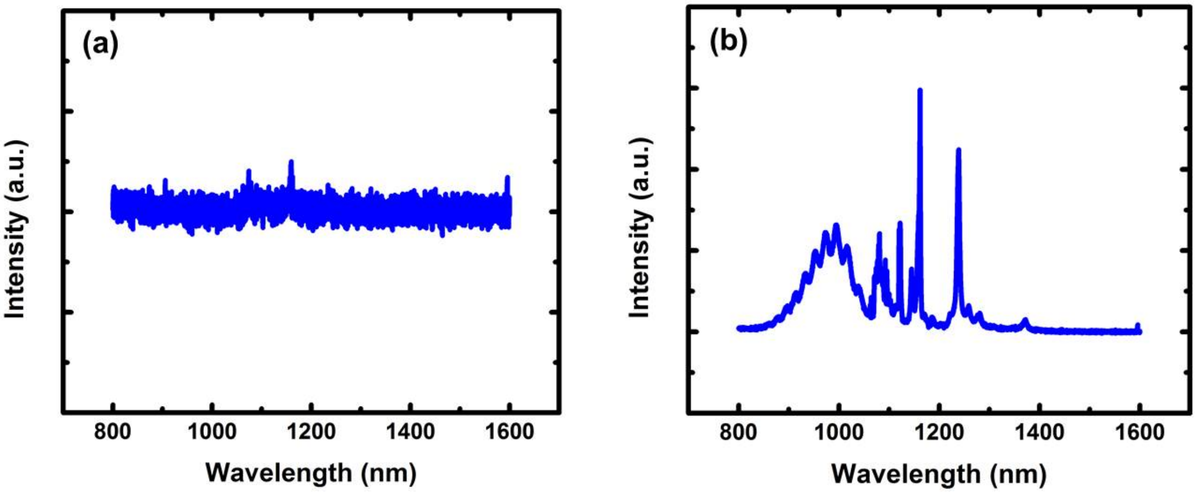

Figure 4.9 Photoluminescence spectra for (a) as-produced SWCNTs and (b) DNA wrapped SWCNTs.

Chapter 5[*]

Spin Filtering Effect in ssDNA-SWCNT Hybrid Nanotubes.

In this chapter, we describe the sixth stage of our work, which is comprised of spin transport studies in ssDNA-SWCNT hybrid nanotubes. These hybrid nanotubes have been fabricated using the methods described in the previous chapter. In order to perform transport measurements in these nanotubes, we have connected them with various metallic electrodes. Details are provided below after an introduction on spin filters and spin transport in chiral organic based systems.

5.1 Introduction.

Spin filters are solid-state systems that are able to generate and detect spin polarized charge carriers [35]. In the field of spintronics, the central idea is to use the spin of a charge carrier as a state variable for information processing and storage, and hence spin filters are indispensable components in all-electrical spintronic devices [4], [10]. In almost all cases, transition metal ferromagnets (Ni, Fe, Co etc.) and their alloys are used as spin filters [35], [185]. These materials are characterized by an unequal density of states between majority and minority spins, say ρ_M and ρ_m respectively, at the Fermi level (Stoner model), and the spin filtering properties of these materials can be understood by considering a simple [tunnel barrier/ferromagnet] composite system [35]. For generation of spin-polarized carriers, consider the case when a negative bias is applied on the ferromagnet. Since the carriers at the (quasi) Fermi level are responsible for tunneling and since these carriers have definite spin-polarization (parallel and antiparallel to the magnetization of the ferromagnet), the tunneling current injected from the ferromagnet will consist of carriers with definite spin polarizations. The population of carriers with spins parallel to majority (minority) spin should be proportional to ρ_M (ρ_m), and hence the net injected spin polarization will be proportional to $\rho_M - \rho_m$. For diamagnetic materials (such as Au, Ag etc.), $\rho_M = \rho_m$, and hence these materials cannot be used to generate spin-polarized carrier population.

---

[*] Parts of this chapter will be submitted for publication as a journal article.

Similarly, a ferromagnet can be used to detect an incoming population of spin-polarized carriers. Suppose n_M and n_m are the densities of carriers with spins parallel to the majority and minority spins, respectively, for a given polarization of the ferromagnet. In this case, tunnel conductance will be proportional to $n_M\rho_M + n_m\rho_m$. However, if the magnetization of the ferromagnet is flipped, tunnel conductance will be proportional to $n_M\rho_m + n_m\rho_M$. Thus the incoming carriers will experience different resistances depending on the magnetization of the ferromagnet. Clearly, if the incoming carriers have no net spin polarization (i.e. $n_M = n_m$) then no change in device resistance will occur. Similarly, if we use a nonmagnet ($\rho_M = \rho_m$) then also no change in device resistance will occur. Thus, observation of a change in device resistance that depends on magnetization of the ferromagnetic electrode implies detection of spin-polarized carriers. Of course, one has to ensure via control experiments that such change does not originate due to any other effect in the system.

As mentioned above, transition metal ferromagnets are widely used in all-electrical spintronic devices [35], [185]. Other candidates that have been explored as spin filters include manganite perovskites and chalcogenides [185]. Very recently various non-conventional materials have also been proposed as spin filters. For example, it has been proposed theoretically that a few layers of graphene as grown on Ni, can act as a "nearly perfect" spin filter [186]. This prediction is based on a special band structure alignment between graphene and Ni at the Fermi level which allows transmission of primarily minority spins. However, to date this effect has not been demonstrated experimentally. Spin selective properties of chiral double-stranded (ds) DNA molecules have been reported experimentally both by optical and electrical techniques [50], [51]. In ref. [50] dsDNA monolayer was adsorbed on a (non-magnetic) gold (Au) substrate. Spin polarization of the photoelectrons transmitted through the dsDNA layer was found to be ~ 60% at room temperature [50]. In ref. [51], current flow has been measured in a nickel/dsDNA/Au device. A change in device resistance has been observed due to spin filtering through the dsDNA [51]. The physical process underlying the above-mentioned effect is not yet well understood [187]–[190]. The main challenge is that dsDNA is non-magnetic and mainly consists of light atoms with small atomic spin-orbit coupling which is not consistent with the experimentally observed high value of spin polarization at room temperature. It has been suggested [187]–[190] that the inversion asymmetry of the helical molecule can potentially enhance the effective spin-orbit interaction, despite the fact that atomic spin-orbit interactions are weak.

Another candidate that has been proposed theoretically as a spin filter is single wall carbon nanotube (SWCNT), wrapped by a chiral molecule (such as single stranded DNA), which creates a helical potential in the tube [52]. Carbon nanotubes (CNTs), which can be loosely described as graphitic sheets rolled into a cylinder, have been explored extensively in the area of spintronics [191]. In almost all studies, carbon nanotubes have been used as an active medium for spin transport, and significant effort has been invested in determining spin relaxation length, time and mechanisms in these structures [191]. Since the nanotubes are made solely by low atomic number (carbon) atoms, spin-orbit coupling is expected to be extremely weak in these systems. However, recent studies have indicated that the curvature arising from the cylindrical geometry can enhance spin-orbit coupling due to hybridization among neighboring carbon atoms [192], [193]. The strength of the spin-orbit interaction is also strongly dependent on the substrates and the species adsorbed on the tube surface [194].

DNA is known to interact strongly with carbon nanotubes and typically result in a helical wrapping of the nanotubes due to π-stacking [163]. The coiling period (pitch) of the DNA molecule correlates well with nanotube chirality [164], [195]. The DNA strands wrapped around the nanotube create a strong and inversion asymmetric electric field. This electric field generates a strong Rashba-type spin-orbit interaction. According to a recent theoretical work [52], such interactions can polarize the spins transmitted by (single-stranded) DNA wrapped carbon nanotubes. To the best of our knowledge, no spin filtering experiment has been performed on DNA-wrapped carbon nanotubes. This is exactly what we intend to explore in this stage of our work.

The DNA-CNT composite has the added advantage of having higher conductivity compared to pure DNA-based devices. The DNA molecule is essentially an insulator and hence is unsuitable for integration with practical spintronic devices where the actual channel will most likely have smaller resistance. Further DNA-CNT hybrids allow efficient fabrication of planar spintronic devices, which is difficult to achieve using DNA molecules alone. The vertical geometry that is generally achieved by DNA molecules [50], [51], is prone to pinhole shorts and possible creation of defects while depositing the top contact. Such problems do not arise in the planar geometry.

In this work, we have used the same principle described in the introductory paragraphs of this chapter to examine the spin-state of the carrier ensemble emanating from one end of a ssDNA wrapped SWCNT. The other end of the ssDNA wrapped SWCNT is connected to a (diamagnetic) Au electrode [Figure 5.1]. The carriers are injected from the Au electrode to the SWCNT, which is wrapped by ssDNA. The carriers injected from the Au electrode have no net spin polarization. These carriers traverse through ssDNA wrapped SWCNT and their spin-polarization at the end of the tube is probed by a nickel electrode. It has been found that device resistance depends on the magnetization orientation of the Ni spin detector. Combined with various control experiments, we show that this phenomenon is related to spin polarization of charge carriers emanating from the ssDNA wrapped SWCNT. This work shows that ssDNA wrapped SWCNT can perform as a spin filter in the sense that it can polarize an injected population of spin-unpolarized carriers (which, in this case, originate from the Au electrode) and it can also differentiate between the net spin polarizations of carriers originating from a known spin injector (which, in this case, is Ni).

5.2 Synthesis of ssDNA-SWCNT Hybrid Nanotube Devices.

The experimental setup and measurement geometry are shown in Figure 5.1. First, we deposited 500 nm of silicon dioxide on a silicon wafer. The 100 nm thick Ni and Au electrodes were sputtered on this surface keeping a gap of 750 nm between them. The device geometry was patterned by photolithography. A droplet of the ssDNA-SWCNT solution prepared according to a well established method (ref. Chapter 4) was placed on and in between the electrodes. After 15 minutes, the solution was washed out with DI water and dried with nitrogen. A field emission scanning electron microscope (FESEM) image (Figure 5.1, inset) shows ssDNA-SWCNT hybrids are connected between the metal electrodes. The two purple arrows show two ends of one ssDNA-SWCNT hybrid nanotube bridging the metal electrodes. The drop-casted solution contains ssDNA wrapped SWCNTs, possibly some unused ssDNA and EDTA (ref. Chapter 4). It is expected that the solution does not contain any SWCNT ropes in presence of excess ssDNA (ref. Chapter 4). EDTA is a small molecule and does not form bonds with either ssDNA or

SWCNT. The ssDNA has only 30 base pairs. Therefore, neither EDTA nor ssDNA are expected to bridge the metal electrodes. AFM shows (Chapter 4) most of the ssDNA-SWCNT hybrids are shorter than the gap (750 nm) between the Ni and Au electrodes. Therefore it is reasonable to assume few hybrids are bridging the electrodes. This argument is justified by the FESEM image (Figure 5.1, inset). We see in this image that most of the tubes are not bridging the electrodes.

For studying the transport properties of these hybrid nanotubes, we applied ±2V across the Ni and Au electrodes. Current voltage data were acquired in presence of a magnetic field of strength 1T applied in two opposite directions. The green arrows in Figure 5.1 correspond to these two magnetic field directions. Note the magnetic field directions are along the easy axis of the Ni electrode.

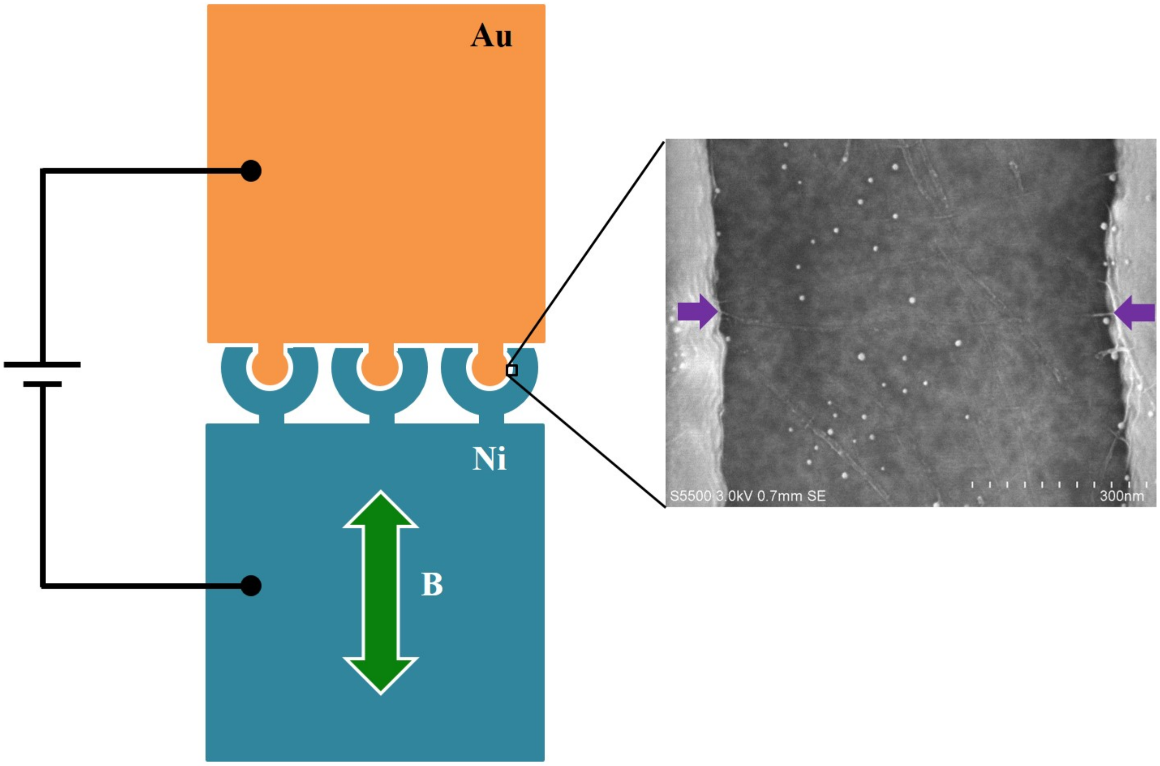

Figure 5.1 Schematic of the experimental setup. The green arrows indicate the two opposite directions (1 Tesla and -1 Tesla) of externally applied magnetic fields. The inset shows a field emission scanning electron microscope (FESEM) image of ssDNA-SWCNT hybrid nanotubes that are connected between Ni and Au electrodes. The two purple arrows show two ends of one ssDNA-SWCNT hybrid nanotube bridging the metal electrodes.

The drop-casted hybrid nanotubes get connected with the metal electrodes by weak Van der Waals bonds. Prior to the transport measurements, we have vacuum annealed the device at 200°C for 30 minutes. This annealing step significantly improves the electrical contact. In order to investigate any structural change introduced by the annealing step, we performed Raman spectroscopy on the annealed hybrid nanotubes. Raman spectroscopy results for both the pristine CNTs and ssDNA wrapped CNTs have been described in detail in the previous chapter. The radial breathing mode (RBM) bands are found frequency upshifted similar to unannealed hybrids found previously (not shown here) while tangential mode (TM) bands demonstrated interesting features. Figure 5.2 shows the G band feature (TM) of annealed hybrid nanotubes. The relative intensity of the G^- to G^+ band is reduced to 0.42. These intensity ratios were 0.67, 0.54 and 0.63 for pristine CNTs, and the two fractions of unannealed ssDNA-SWCNT hybrids respectively (ref. Chapter 4). This intensity reduction implies a further suppression of vibrations of carbon atoms along the circumferential direction. Therefore, we conclude that mild annealing results in a tighter wrapping of CNTs by ssDNA.

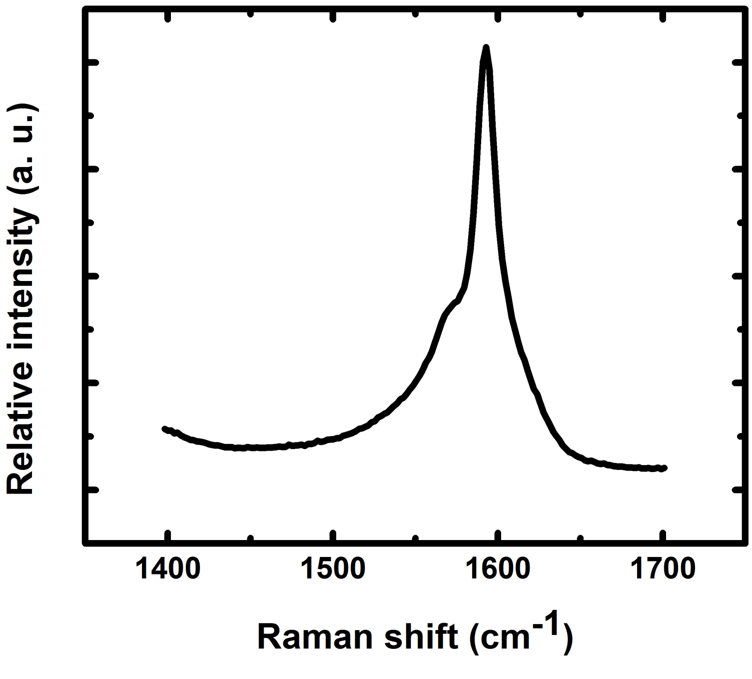

Figure 5.2 Tangential modes (TM) in Raman spectra for annealed DNA wrapped SWCNTs.

5.3 Transport Experiments.

Detailed electrical measurements have been performed on the devices described above. There exist two possible conduction pathways between the electrodes: the SWCNT and the ssDNA molecular chain that wraps the SWCNT. In the past, various groups have explored electrical transport in DNA molecules with varying lengths [196]–[199]. In these molecules, two different conduction processes can take place [196]–[199]: (a) coherent tunneling between the electrodes and (b) diffusive thermal hopping between various molecular sites. In our devices, the ssDNA molecular chain is long, ~750 nm, which precludes conduction via coherent tunneling. Hopping transport, assisted by phonons, is expected to be the dominant process for such long chain ssDNA molecules. However, this mechanism becomes almost ineffective at the low temperature range (~10–30K) employed in this study, and under these operating conditions the long chain ssDNA molecule can be viewed as an insulator. This is consistent with the established literature on electrical conduction via long DNA molecules [196]–[199]. The nitrogen drying step and extended (~30 minutes) high temperature (~200^{o}C) annealing step described above makes any water molecule mediated ionic conduction highly unlikely. Further, this mode of conduction will be even less effective at cryogenic temperatures and under dc operating conditions employed in this study. Thus, we conclude that the SWCNT is the primary charge transport channel in our devices. Direct experimental evidence of this picture has been discussed later in this work, where we show that there is no qualitative difference between the temperature-dependent current-voltage characteristics of SWCNT and ssDNA-wrapped SWCNT. In fact, if the DNA molecule participates in charge conduction, it results in a "staircase shape", with a significant conductance suppression over a bias range of ~ 1V near zero bias in the current-voltage characteristics [200]. Such effects have not been observed in our experiments even at room temperature. Thus the ssDNA chain does not offer any charge transport pathway to the carriers in our experiments.

It is important to note the distinction between our devices and previous DNA-based spin filters as reported in ref. [51]. For example, in ref. [51] no SWCNT was present and spin selectivity of double stranded DNA molecule was explored. In this case, charge transfer occurred via the double stranded DNA molecules. The current-voltage characteristics (taken at room temperature) in this work [51] indicates a wide bandgap semiconductor (or insulator) behavior, which is consistent with existent literature on charge transport in DNA [196]. In our case, as described above, the main conduction channel is the SWCNT. The ssDNA molecular chain offers a helicoidal potential to the charge carriers in the nanotube due to the electrostatically charged sugar-phosphate backbone. As discussed before, the helical wrapping of ssDNA around SWCNT is mediated by the electrostatic interaction of the sugar-phosphate backbone, as well as overlap of π orbitals of ssDNA bases and (sp^2 hybridized) carbon atoms of the SWCNT.

The current-voltage (*I-V*) measurements have been performed for two orientations of the in-plane magnetic field (+1T and – 1T) over a wide temperature range of 10 – 300K. Typical measurement geometry is shown in Figure 5.1. Since the in-plane coercivities of the Ni thin film electrodes are very small (~ 0.01T range), the above-mentioned magnetic field values are more than sufficient to control the magnetization orientation of the Ni electrode. As described below, two control experiments have been performed to obtain a better understanding of the observed behavior. Multiple (~10) devices have been tested in each category and the behavior reported below is representative of each category.

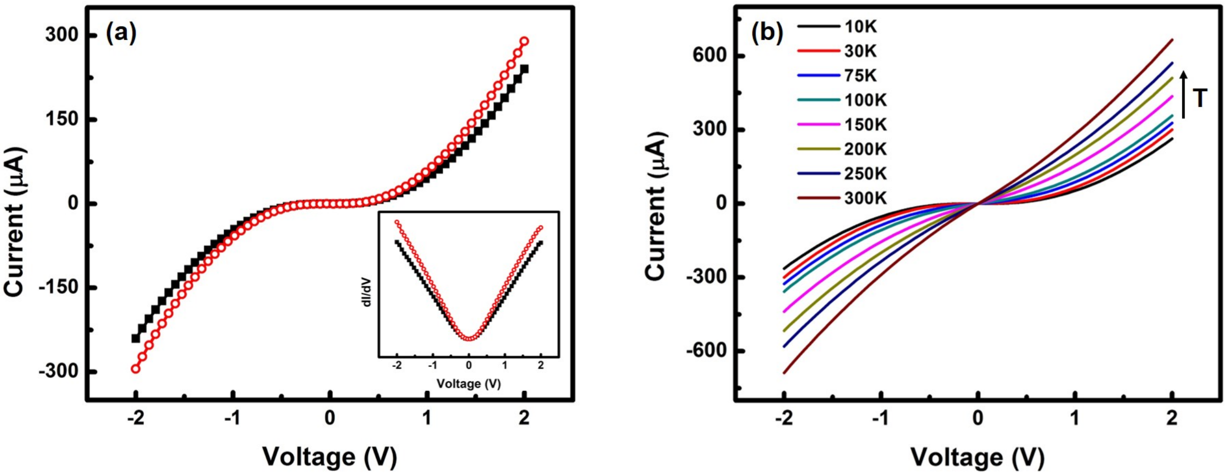

Figure 5.3 (a) Current vs. voltage curves for the Au-ssDNA-SWCNT-Ni device for two opposite directions of magnetic field at 10K. The filled black squares represent the data obtained at 1 Tesla and the open red circles represent the data obtained at -1 Tesla. (inset) The corresponding differential conductance vs. voltage curves. (b) Current vs. voltage curves for this device at different temperatures in the absence of a magnetic field.

We have measured the current-voltage (*I-V*) characteristics of Au/[ssDNA-SWCNT]/Ni devices for +1T and –1T. Figure 5.3 (a) shows the *I-V* plot of this device at 10K. The key observation in this case is the manifestation of a splitting in the current-voltage characteristics as a function of the magnetic field orientation. The splitting is more pronounced at higher bias. This effect is strongest at the lowest measurement temperature of 10K and gradually decreases as the temperature is increased and almost vanishes at ~30K. The inset show the computed conductance (d*I*/d*V*) versus bias (*V*) plot at 10K. A clear gap in the conductance has been seen as a function of magnetic field orientation. Figure 5.3 (b) shows the temperature dependence of the zero magnetic field current-voltage characteristics over the entire temperature range of 10 – 300K used in this study. Semiconducting temperature dependence has been observed, which is consistent with prior studies on SWCNTs [201].

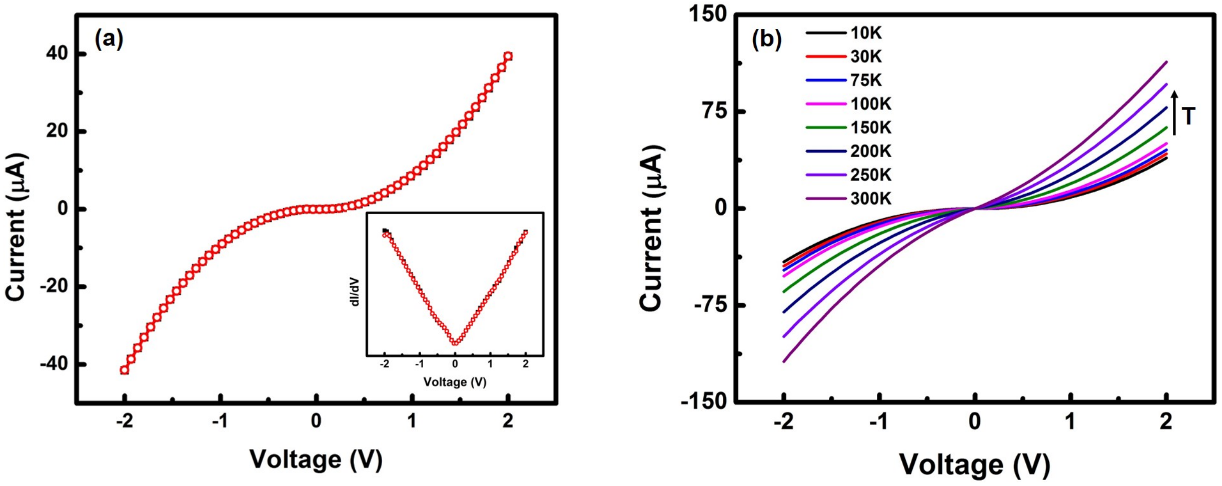

Figure 5.4 (a) Current vs. voltage curves for the Au-ssDNA-SWCNT-Au device for two opposite directions of magnetic field at 10K. The filled black squares represent the data obtained at 1 Tesla and the open red circles represent the data obtained at -1 Tesla. (inset) The corresponding differential conductance vs. voltage curves. (b) Current vs. voltage curves for this device at different temperatures in the absence of a magnetic field.

Clearly, as seen from Figure 5.3 (a), a magnetoresistance effect exists in Au/[ssDNA-SWCNT]/Ni devices. This magnetoresistance can originate from various sources and in order to obtain a better understanding of this effect we have tested two reference devices. In the first reference device, the Ni electrode has been replaced by a gold electrode and everything else has been kept the same as before. Transport data from these reference devices are shown in Figure 5.4 (a). In this case, no splitting in the current-voltage characteristics has been observed for any device even at low temperatures. Temperature dependence of the zero magnetic field current-voltage characteristics over the entire temperature range of 10 – 300K has been shown in Figure 5.4 (b). These samples exhibit qualitatively similar current-voltage characteristics as in Figure 5.3. Thus, we conclude that the presence of the Ni electrode is essential for observation of the splitting reported in Figures 5.3 (a). This reference experiment also confirms that the orbital magnetoresistance effects of Au and ssDNA-SWCNT are not responsible for the features observed in Figure 5.3 (a).

In our second reference experiment, we have explored the role of ssDNA wrapping. In this case, Au/[SWCNT]/Ni devices have been fabricated in the absence of ssDNA molecules and hence any wrapping. These unwrapped SWCNTs were synthesized by a similar process of ultrasonication and centrifugation (ref. Chapter 4) in 1% sodium dodecyl sulfate instead of ssDNA d(GT)$_{15}$ [202]. In the inset of Figure 5.5 (b), we see the AFM image of these dispersed SWCNTs without ssDNA. As shown in Figure 5.5, the current-voltage characteristics are qualitatively in agreement with Figures 5.3 and 5.4. This provides direct experimental evidence

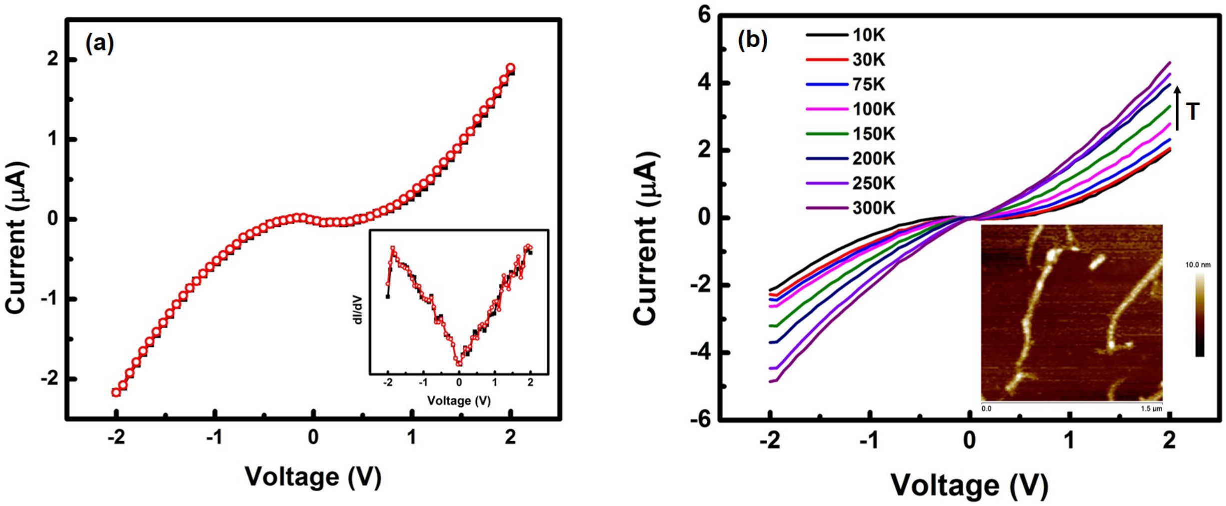

Figure 5.5 (a) Current vs. voltage curves for the Au-SWCNT-Ni device for two opposite directions of magnetic field at 10K. The filled black squares represent the data obtained at 1 Tesla and the open red circles represent the data obtained at -1 Tesla. (inset) The corresponding differential conductance vs. voltage curves. (b) Current vs. voltage curves for this device at different temperatures in the absence of a magnetic field. (inset) Atomic force microscope (AFM) image of unwrapped single wall carbon nanotubes on a bare SiO$_2$ substrate.

in support of our previous observation where we argued that the primary conduction channel in our devices is SWCNT and the ssDNA molecular chain has no major role in conduction. The conductance is suppressed for voltage range ~ few mV near zero bias at low temperatures (~10K). This is consistent with previous studies performed on SWCNTs of comparable dimensions and operating temperatures [201]. However, unlike Figures 5.3, we do not observe any splitting in the current-voltage characteristics when an external magnetic field is applied. Thus, we conclude that wrapping of the SWCNT channel by ssDNA is a key component behind the observed splitting. No significant magnetoresistance effect has been observed in this case, implying negligible presence of any spurious Hall effect due to the fringing field lines from the Ni contact.

In the past, it has been proposed that certain chemical groups (such as thiols) when adsorbed on Au can make the Au surface magnetic [203], [204]. Such effects are unlikely to occur in our experiments simply because we do not use thiol groups unlike the experiments cited above. The chemicals used in our experiment (EDTA) are not known to have similar properties, and the fabrication steps used in this study ensures the presence of such chemicals in trace amounts only. Thus, the feature observed in Figures 5.3 (a) are unlikely to arise from these effects.

Summarizing the above discussion, we conclude that the splitting is observed only when the SWCNT is wrapped with ssDNA and one of the contacts is Ni. This effect has been shown not to originate from any orbital magnetoresistance effect or spurious Hall effects in the system. Thus, we proceed to explain this effect using the framework of spin-polarized carrier generation and detection. This model is based on recent theoretical work [52] that predicted spin polarized conductance for DNA-wrapped CNTs which originates due to the Rashba spin-orbit coupling due to the helicoidal electric field induced by the ssDNA molecule.

In our transport measurement setup, the nickel contact has always been used as the ground terminal. For negative voltage polarity, electrons are injected into the ssDNA-SWCNT from the Au electrode. The exact nature of this contact is unknown and even the nature of the DNA/metal contact is still unclear even after decades of research [196]–[199]. However, according to our present understanding, it is highly unlikely that there is good ohmic contact, and the contact can be represented by a Schottky-type potential barrier. Carrier injection occurs primarily via tunneling, at least in the low temperature regime where thermionic emission is muted. Since Au is diamagnetic, these electrons have no net spin polarization in any direction, even in the presence of an external magnetic field. In this ensemble of electrons, 50% of the population has “spin up” polarization component (which, say, is parallel to “+1T” orientation of the external magnetic field) and the remaining 50% has “spin down” polarization component (i.e. parallel to “– 1T”) and the net polarization is zero. As these electrons traverse through the ssDNA wrapped SWCNT, according to ref. [52], they may accumulate some net spin polarization (say P). If this happens, the accumulated spin polarization P can be sensed by the ferromagnetic Ni “spin detector” at the other end of the device. Note that there exists a Schottky-type barrier at this detecting interface as well. As the magnetization of the Ni electrode is flipped, as seen in Figures 5.3, it indeed offers a different resistance to these carriers, indicating non-zero value of P. Thus, combining with the results from the reference experiments we conclude that ssDNA wrapped SWCNT indeed polarizes an initially spin-unpolarized population of carriers. It is important to note that the role of the external magnetic field is to flip the magnetization of the Ni ferromagnet and thus facilitate in spin detection. It does not play any direct role in creation of the incoming spin polarization P. This spin-polarization is created from an unpolarized ensemble (diamagnetic Au electrode) due to the influence of the helicoidal potential induced by ssDNA wrapping.

The reverse effect takes place when the voltage polarity is positive. In this case, spin polarized electrons are injected from the Ni electrode. The Au/[ssDNA-SWCNT] composite can be viewed as an effective electrode with a fixed spin polarized density of states (with spin polarization P) at the (quasi) Fermi level. This composite now acts as a spin detector. As Ni magnetization is flipped, so does the polarity of the incoming spins from the Ni. The composite electrode offers different resistances in both cases, resulting in split current-voltage characteristics in the positive quadrant.

For Au/[ssDNA-SWCNT]/Au reference devices, no spin detecting electrode is present since Au is nonmagnetic. Therefore, even though spin-polarized carriers are generated by the Au/[ssDNA-SWCNT] composite, they go undetected by the second Au electrode, and hence no splitting is observed in the current-voltage characteristics. For Au/[SWCNT]/Ni devices, no splitting has been observed which underscores the critical role played by the helicoidal potential of the ssDNA molecule.

Using the physical picture described above, we can estimate the spin polarization *P* by applying the Julliere formula (ref. Chapter 1). As mentioned before, these electrons are ultimately detected by the Ni electrode. There exists a Schottky-type potential barrier at the Ni/[ssDNA-SWCNT] interface, and at the low temperatures employed in this study, transport at this interface is primarily due to tunneling. Applying Julliere's formula at the tunnel junction at the detecting interface, we obtain a spin polarization value (lower limit) of $P \sim 35\%$ at low bias.

The disappearance of this effect at higher temperature can be ascribed to the enhanced spin relaxation within the tube at higher temperatures. In order to observe the spin filtering effect, the Rashba spin-split bands should remain sufficiently distinct. At higher temperature, thermal energy broadens these bands, leading to enhanced spin mixing and loss of spin filtering.

From the computed dI/dV curves, we observe that a given conductance level is achieved for different bias values, depending on the magnetization orientation of Ni. This bias differential should reflect the potential barrier experienced by the "unfavorable" spins as compared to the "favorable" ones. The barrier is ~ 0.3 eV for a bias of ~1.5V, and the barrier height increases with bias. Such spin-dependent barrier height is too high to be explained by invoking atomic spin-orbit coupling of the lightweight elements that comprise the ssDNA-SWCNT hybrid. In the present case, SWCNT and ssDNA primarily consist of light elements with atomic spin-orbit coupling values at least two orders of magnitude smaller than the barrier height estimated above. Also as discussed previously, the main conduction channel is SWCNT and the carbon atoms, in their most abundant form (^{12}C), do not offer any hyperfine interaction. Thus, this mechanism alone cannot explain the large spin dependent barrier height discussed above. Therefore, this work should be viewed within the framework of the Rashba spin-orbit interaction induced by the helicoidal electric field of the ssDNA [52].

In the sixth stage of our work, we have demonstrated spin-selective carrier transmission in ssDNA wrapped SWCNT. Significant spin polarization, comparable to typical transition metal ferromagnets, has been observed at low temperature. The helical wrapping of the ssDNA is essential for observing this effect. The possibility of generating spin-polarized carriers via non-magnetic materials can result in "magnetless" spintronic devices in future, which will relax some of the fabrication constraints involved in state-of-the-art spintronic devices.

Chapter 6

Conclusions and Recommendations.

In this thesis, we have reported synthesis of organic nanowires using a novel technique and have demonstrated the feasibility of spin injection and transport in these organic nanowires (Chapters 2 and 3). We have also explored another feature of organic spintronics, namely "spin filtering" (Chapters 4 and 5). In this chapter, we will first present the summary of original contributions and major conclusions throughout the different stages of our work. Next, we will introduce a few future possible projects.

6.1 Summary of Contributions and Conclusions.

(1) For fabrication of the nanowire organic spin valve device, we have used anodic aluminum oxide (AAO) templates. The AAO template contains an array of well-ordered cylindrical nanopores. Formation of nanopores is an outcome of an electrochemical self-assembly process. It is essential to create a highly polished aluminum substrate with surface roughness of only a few nanometers, in order to obtain well-ordered nanopores of uniform dimension.

In the first stage of our work, we have demonstrated a chemical polishing technique which offers a simpler, faster and safer route for aluminum pretreatment prior to anodization. This work is intended to draw renewed attention on the oft-overlooked chemical polishing method which has several advantages over the commonly employed electropolishing approach. We have performed an extensive study of the surface roughness which shows that this method produces similar (or better) results compared to electropolishing. Additionally, this process (a) is parallel with faster throughput (i.e. multiple aluminum substrates with arbitrary areas can be processed simultaneously), (b) is amenable to large area polishing and (c) avoids perchloric acid and related hazards altogether. Ordered nanopores are formed after multistep anodization of chemical polished surfaces. Nanopore formation process is essentially identical to that in the electropolished case. Under certain polishing conditions, parallel nanoridges are formed which can be further processed to fabricate parallel arrays of nanoscale crossbars. Such structures are the linchpins of many nanoscale memories and computing architectures.

(2) In the second stage, we have fabricated organic nanowires within the nanopores of the AAO template using a novel “centrifugation-assisted” technique. There are very few reports in literature on fabrication of small-molecular organic nanowires in AAO templates. These works used a special organic evaporator with the facility of a carrier gas inside the deposition chamber. This method, however, does not allow growth of nanowires of arbitrary dimensions. We have developed a novel, reagentless, one-step process that produces an array of vertically oriented organic nanowires within AAO matrix. This method also allows fabrication of axially heterostructured metal-organic bilayer hybrid nanowires, permits direct electrical contact at the two ends of the nanowires and therefore can be used for synthesis of various functional organic nanowire devices.

(3) In the third stage, we have extensively characterized the organic nanowires grown by the above-mentioned technique. In addition to field emission scanning electron microscope (FESEM) studies, we have performed X-Ray diffraction (XRD), photoluminescence (PL) and Fourier transform infrared spectroscopy (FTIR) characterization of these nanowires. The characterization experiments confirmed growth of rubrene nanowires within AAO templates.

(4) In the fourth stage, we have successfully combined the above-mentioned techniques to fabricated rubrene *nanowire* spin valve devices . Rubrene has been selected since based on recent reports this material is expected to show a large spin relaxation length. Both electrical and spin transport measurements have been performed on rubrene nanowire spin valves. The magnetoresistance data clearly shows the spin valve signal, indicating successful spin injection, transport and detection in these devices. Control experiments have been performed to confirm the physical origin of the observed effect. The major conclusions from these measurements are listed below.

(a) Larger spin relaxation length compared to thin film devices.
(b) Spin-orbit interaction appears to be the most likely agent for spin relaxation.
(c) Molecular packing (growth process) affects the spin relaxation.

(d) Long spin relaxation time and length are very promising in spintronic logic and memory devices as well as in spin organic light emitting diodes.

(e) OMAR is likely to be the origin of background high field MR.

(f) Spin relaxation length falls faster in the strong coulomb interaction regime.

(5) In the fifth stage, we have synthesized and dispersed single wall carbon nanotubes wrapped with single-stranded deoxyribonucleic acid (ssDNA). We have also characterized these hybrid nanotubes through FESEM, AFM, Raman spectroscopy, and photoluminescence (PL). AFM and SEM images, Raman spectroscopy, and PL signals confirm efficient DNA wrapping around SWCNTs. We have observed a spontaneous alignment of these hybrids on a bare SiO_2.

(6) In the sixth stage, we have performed electrical transport measurements on the CNT-DNA hybrid nanotubes synthesized in the fifth stage of our work. Our experimental results indicate that these hybrid nanotubes can act as efficient spin filters. Significant spin polarization, comparable to typical transition metal ferromagnets, has been observed at low temperature. The helical wrapping of the ssDNA is essential for observing this effect. Control experiments have been performed to confirm the physical origin of the observed effect.

6.2 Future Recommendations.

Based on our experimental results on ssDNA-SWCNT hybrids (stage six) and previous works reported by other groups [50]–[52], a few possible endeavors could be made to explore the spin filtering properties of organic materials in magnetic tunnel junction (MTJ) configuration. The ensuing sections briefly discuss and give guidelines to those possible future projects.

6.2.1 Introduction.

As discussed before (ref. Chapter 5), spin filters are solid-state systems that preferentially transmit spins of one particular orientation. Spin filters are an essential component of all-electrical spintronic devices such as magnetic tunnel junctions (MTJs) [35], spin field-effect transistors (spin-FETs) [4] and many others [205], where they are employed as spin injectors and detectors (ref. Chapter 1). An ideal spin filter transmits only one particular spin orientation and blocks all other spin orientations. Ideal spin filters can improve the performance of virtually all spin-based electrical devices. For example, they result in extremely large magnetoresistance (MR) ratios in MTJs, which can be exploited to achieve reliable read operation in high-density magnetic random access memory (MRAM) chips. Ideal spin filtering can also significantly attenuate the leakage current and enhance the conductance on-off ratio in spin-FETs [4]. Very few experimental studies exist that convincingly demonstrate efficient electrical spin filtering through organic molecules. In the ensuing sections we briefly discuss two experimentally realizable projects.

6.2.2 Proposed Projects.

Electrical spin filtering experiments can be performed with the following systems by employing a magnetic tunnel junction geometry:
(1) Chiral molecule such as double stranded deoxyribonucleic acid (dsDNA), and
(2) Single wall carbon nanotube (SWCNT) wrapped with single stranded DNA (ssDNA).

Spin filtering efficiency of these structures can be experimentally determined by the magnetic tunnel junction (MTJ) configuration [35]. This geometry is commonly used for characterizing spin filter materials [206]. The experimental data can be analyzed using the Julliere formalism. The two systems mentioned above can lead to magnetless spintronic devices, which will relax some of the fabrication constraints involved in state-of-the-art spintronic devices.

6.2.2.1 Subproject A: Spin Filtering with dsDNA.

Background.

Experimental results on spin selective properties of chiral dsDNA molecules have been reported in references [50] and [51]. In ref. [50], dsDNA monolayer was adsorbed on a (non-magnetic) gold (Au) substrate. Spin polarization of the photoelectrons transmitted through the dsDNA layer was found to be ~60% at room temperature. Such values of spin polarization are much larger compared to common transition metal ferromagnets [35]. In ref. [51], current flow has been measured in a nickel/dsDNA/Au device. A change in device resistance has been observed due to spin filtering through the dsDNA. The physical process underlying the above-mentioned effect is not yet well-understood [188]–[190], [207], [208]. The main challenge is that dsDNA is nonmagnetic and mainly consists of light atoms with small atomic spin-orbit coupling [188]–[190], [208], which is not consistent with the experimentally observed high values of spin polarization at room temperature [50], [51]. It has been suggested [188]–[190], [208] that the inversion asymmetry of the helical molecule can potentially enhance the effective spin-orbit interaction, despite the fact that atomic spin-orbit interactions are weak. The hyperfine interaction due to nuclear spins can also play a crucial role. To the best of our knowledge, this effect has not been investigated for dsDNA based MTJ devices. For the above-mentioned spin filter concept to be useful, it is necessary to employ the Au/dsDNA composite as a spin injector (or detector) in a spin valve (or magnetic tunnel junction) geometry [206]. Such configurations will also allow estimation of the spin filtering efficiency in an electrical setup which may be different than that obtained optically due to possible presence of additional spin scattering processes. Electrically detected spin filtering efficiency is a more relevant metric for spintronic devices since it indicates the suitability of new spin filters for practical applications.

Proposed Methodology.

Double stranded DNA monolayers can be self-assembled on a gold substrate using a standard recipe described in refs. [50] and [209]. Vertical orientation of the ds-DNA helices is necessary for a higher degree of spin filtering [50]. Such organization can be achieved by (a) modifying one end of DNA by adding a thiol group which has an intrinsically high affinity to Au [209], and (b) partially covering the Au surface by an insulating and hydrophobic layer (C_{18}–SH) before adsorption of the thiolated DNA [209]. The last step allows specific binding of the thiolated ends of DNA with Au (through the regions not covered by C_{18}–SH) and prevents any other nonspecific bindings [209]. Being insulating, C_{18}–SH layer is not expected to interfere with the electrical measurements [209]. Next, a thin layer (~1 nm) of alumina or other appropriate insulator can be deposited on the ds-DNA layer. Various deposition methods can be tried such as electron beam evaporation or atomic layer deposition (ALD). Care needs to be taken to avoid any structural damage of the DNA molecule. Finally, a transition metal ferromagnet of known spin polarization (e.g. Co, NiFe, CoFe, etc.) can be deposited on the topmost surface. A schematic description of this device is shown in Figure 6.1 (a). Magnetoresistance response of this device can be measured over a wide temperature range and magnetic field range. Magnetoresistance data can be modeled by the Julliere formula to determine the spin filtering efficiency of the dsDNA/Au composite.

6.2.2.2 Subproject B: Spin Filtering with ssDNA Wrapped SWCNT.

Background.

Carbon nanotubes have been explored extensively in the area of spintronics [191]. In almost all studies, carbon nanotubes have been used as an active medium for spin transport, and significant effort has been invested in determining spin relaxation length, time and mechanisms in these structures [210]–[213]. We have already discussed about ssDNA wrapped single wall carbon nanotubes (SWCNTs) in Chapters 4 and 5. We have demonstrated that ssDNA wrapped SWCNTs behave as spin filters. The wrapping induced helicoidal potential is crucial for observation of this effect (Chapter 5). In the following paragraph, we will briefly discuss a MTJ device where ssDNA-SWCNT hybrid nanotubes can be employed as a spin filter.

Proposed Methodology.

Exploration of spin filtering properties of ssDNA wrapped SWCNTs can be performed in a vertical geometry using a magnetic tunnel junction (MTJ) device configuration. In this MTJ, ss-DNA wrapped tubes will serve as one of the contacts and a ferromagnet with known spin polarization as the other contact [Figure 6.1 (b)]. These two contacts will be separated by an appropriate tunnel oxide. The fabrication of this vertical geometry [Figure 6.1 (b)] can be performed by using the methodology in section 6.2.2.1 with minor modifications. Single stranded DNA wrapped tubes can be formed by mixing nanotubes in an aqueous solution of ssDNA in an ice water bath as described in Chapter 4. One end of the ssDNA will be thiolated to facilitate binding with gold substrate. Prior surface modification of the gold substrate (similar to that described in section 6.2.1) will allow vertical orientation of the ssDNA wrapped nanotubes. Next, tunnel barrier growth can be performed, followed by deposition of a ferromagnet with known spin polarization, to complete the magnetic tunnel junction geometry. These steps are same as that described before. Temperature-dependent magnetoresistance measurements can be performed on this device to detect any spin filtering effect.

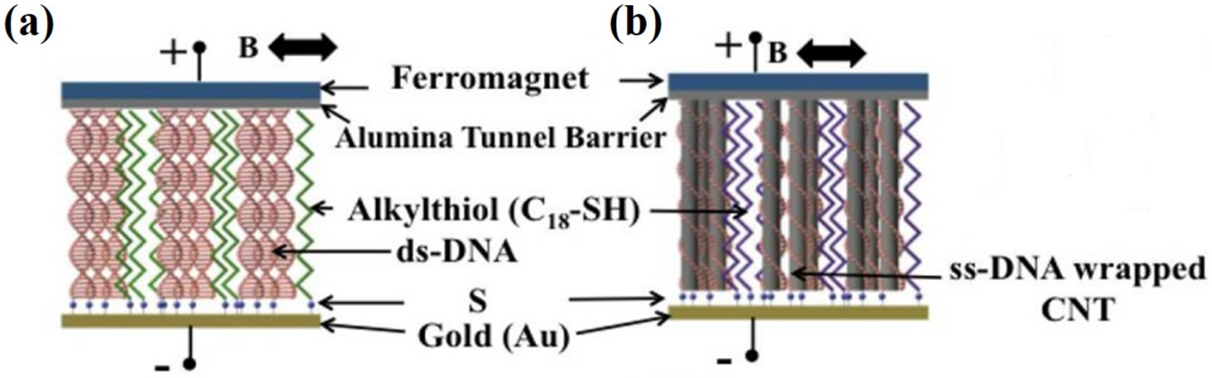

Figure 6.1 Schematic representation of the proposed spin filters, integrated with MTJ for electrical measurement of spin filtering efficiency. MTJs with (a) Au/dsDNA, (b) Au/ssDNA wrapped SWCNTs.

References.

[1] K. M. Alam and S. Pramanik, "Spin Transport in Organic Semiconductors: A Brief Overview of the First Eight Years," in *Nano-Semiconductors: Devices and Technology*, Boca Raton, Florida, USA: CRC Press, 2012, p. 87.

[2] S. A. Wolf, D. D. Awschalom, R. A. Buhrman, J. M. Daughton, S. von Molnár, M. L. Roukes, A. Y. Chtchelkanova, and D. M. Treger, "Spintronics: A Spin-Based Electronics Vision for the Future," *Science*, vol. 294, no. 5546, pp. 1488–1495, Nov. 2001.

[3] S. A. Wolf, A. Y. Chtchelkanova, and D. M. Treger, "Spintronics: a retrospective and perspective," *IBM J. Res. Dev.*, vol. 50, no. 1, pp. 101–110, Jan. 2006.

[4] S. Bandyopadhyay and M. Cahay, "Electron spin for classical information processing: a brief survey of spin-based logic devices, gates and circuits," *Nanotechnology*, vol. 20, no. 41, p. 412001, Oct. 2009.

[5] M. Cahay and S. Bandyopadhyay, "An electron's spin—Part I," *IEEE Potentials*, vol. 28, no. 3, pp. 31 –35, Jun. 2009.

[6] D. D. Awschalom and M. E. Flatté, "Challenges for semiconductor spintronics," *Nature Physics*, vol. 3, no. 3, pp. 153–159, 2007.

[7] M. Cahay and S. Bandyopadhyay, "Spintronics," *Circuits, Devices and Systems, IEE Proceedings* -, vol. 152, no. 4, pp. 293 – 296, Aug. 2005.

[8] M. N. Baibich, J. M. Broto, A. Fert, F. N. Van Dau, and F. Petroff, "Giant Magnetoresistance of (001)Fe/(001)Cr Magnetic Superlattices," *Physical Review Letters*, vol. 61, no. 21, pp. 2472–2475, Nov. 1988.

[9] G. Binasch, P. Grünberg, F. Saurenbach, and W. Zinn, "Enhanced magnetoresistance in layered magnetic structures with antiferromagnetic interlayer exchange," *Physical Review B*, vol. 39, no. 7, pp. 4828–4830, Mar. 1989.

[10] C. Chappert, A. Fert, and F. N. V. Dau, "The emergence of spin electronics in data storage," *Nature Materials*, vol. 6, no. 11, pp. 813–823, 2007.

[11] C. Palmstrom, "Spintronics," *IEEE Signal Processing Magazine*, vol. 23, no. 6, pp. 96 –94, Nov. 2006.

[12] J. M. Daughton, "Magnetic tunneling applied to memory (invited)," *Journal of Applied Physics*, vol. 81, no. 8, pp. 3758–3763, Apr. 1997.

[13] J. Åkerman, "Toward a Universal Memory," *Science*, vol. 308, no. 5721, pp. 508–510, Apr. 2005.

[14] J. S. Moodera, L. R. Kinder, T. M. Wong, and R. Meservey, "Large Magnetoresistance at Room Temperature in Ferromagnetic Thin Film Tunnel Junctions," *Physical Review Letters*, vol. 74, no. 16, pp. 3273–3276, Apr. 1995.

[15] S. Yuasa, T. Nagahama, A. Fukushima, Y. Suzuki, and K. Ando, "Giant room-temperature magnetoresistance in single-crystal Fe/MgO/Fe magnetic tunnel junctions," *Nature Materials*, vol. 3, no. 12, pp. 868–871, Oct. 2004.

[16] A. Ney, C. Pampuch, R. Koch, and K. H. Ploog, "Programmable computing with a single magnetoresistive element," *Nature*, vol. 425, no. 6957, pp. 485–487, Oct. 2003.

[17] D. Nikonov, G. Bourianoff, and P. Gargini, "Power Dissipation in Spintronic Devices Out of Thermodynamic Equilibrium," *Journal of Superconductivity and Novel Magnetism*, vol. 19, no. 6, pp. 497–513, 2006.

[18] R. H. Dennard, F. H. Gaensslen, V. L. Rideout, E. Bassous, and A. R. LeBlanc, “Design of ion-implanted MOSFET’s with very small physical dimensions,” *IEEE Journal of Solid-State Circuits*, vol. 9, no. 5, pp. 256 – 268, Oct. 1974.

[19] K. J. Kuhn, “Moore’s law past 32nm: Future challenges in device scaling,” in *Proceedings of the 13th International Workshop of Computational Electronics*, 2009, pp. 1 – 6.

[20] B. Behin-Aein, S. Salahuddin, and S. Datta, “Switching Energy of Ferromagnetic Logic Bits,” *IEEE Transactions on Nanotechnology*, vol. 8, no. 4, pp. 505 –514, Jul. 2009.

[21] P. S. Peercy, “The drive to miniaturization,” *Nature*, vol. 406, no. 6799, pp. 1023–1026, Aug. 2000.

[22] S. Bandyopadhyay and M. Cahay, *Introduction to Spintronics*, 1st ed. CRC Press, 2008.

[23] D. Loss and D. P. DiVincenzo, “Quantum computation with quantum dots,” *Physical Review A*, vol. 57, no. 1, pp. 120–126, Jan. 1998.

[24] B. Behin-Aein, D. Datta, S. Salahuddin, and S. Datta, “Proposal for an all-spin logic device with built-in memory,” *Nature Nanotechnology*, vol. 5, no. 4, pp. 266–270, Feb. 2010.

[25] H. Dery, P. Dalal, L. Cywiński, and L. J. Sham, “Spin-based logic in semiconductors for reconfigurable large-scale circuits,” *Nature*, vol. 447, no. 7144, pp. 573–576, May 2007.

[26] S. Datta and B. Das, “Electronic analog of the electro-optic modulator,” *Applied Physics Letters*, vol. 56, no. 7, pp. 665–667, Feb. 1990.

[27] T. D. Ladd, F. Jelezko, R. Laflamme, Y. Nakamura, C. Monroe, and J. L. O’Brien, “Quantum computers,” *Nature*, vol. 464, no. 7285, pp. 45–53, Mar. 2010.

[28] I. Žutić and S. Das Sarma, “Spintronics: Fundamentals and applications,” *Reviews of Modern Physics*, vol. 76, no. 2, pp. 323–410, Apr. 2004.

[29] J. Fabian and S. D. Sarma, “Spin relaxation of conduction electrons,” *Journal of Vacuum Science Technology B: Microelectronics and Nanometer Structures*, vol. 17, no. 4, pp. 1708 –1715, Jul. 1999.

[30] R. J. Elliott, “Theory of the Effect of Spin-Orbit Coupling on Magnetic Resonance in Some Semiconductors,” *Phys. Rev.*, vol. 96, no. 2, pp. 266–279, Oct. 1954.

[31] M. Dyakonov and V. Perel, “Spin Relaxation of Conduction Electrons in Noncentrosymmetric Semiconductors,” *Sov. Phys. Solid State*, vol. 13, no. 12, pp. 3023–3026, 1972.

[32] G. L. Bir, A. G. Aronov, and G. E. Pikus, “Spin relaxation of electrons due to scattering by holes,” *Soviet Journal of Experimental and Theoretical Physics*, vol. 42, p. 705, Oct. 1975.

[33] M. I. D’Yakonov and V. I. Perel’, “Optical orientation in a system of electrons and lattice nuclei in semiconductors. Theory,” *Soviet Journal of Experimental and Theoretical Physics*, vol. 38, p. 177, Jan. 1974.

[34] M. Julliere, “Tunneling between ferromagnetic films,” *Physics Letters A*, vol. 54, no. 3, pp. 225–226, Sep. 1975.

[35] E. Y. Tsymbal, O. N. Mryasov, and P. R. LeClair, “Spin-dependent tunnelling in magnetic tunnel junctions,” *Journal of Physics: Condensed Matter*, vol. 15, no. 4, pp. R109–R142, Feb. 2003.

[36] J. De Teresa, A. Barthélémy, A. Fert, J. Contour, R. Lyonnet, F. Montaigne, P. Seneor, and A. Vaurès, “Inverse Tunnel Magnetoresistance in Co/SrTiO3/La0.7Sr0.3MnO3: New Ideas on Spin-Polarized Tunneling,” *Physical Review Letters*, vol. 82, no. 21, pp. 4288–4291, May 1999.

[37] J. H. Shim, K. V. Raman, Y. J. Park, T. S. Santos, G. X. Miao, B. Satpati, and J. S. Moodera, “Large spin diffusion length in an amorphous organic semiconductor.,” *Physical Review Letters*, vol. 100, no. 22, p. 226603, 2008.

[38] Z. H. Xiong, D. Wu, Z. V. Vardeny, and J. Shi, “Giant magnetoresistance in organic spin-valves,” *Nature*, vol. 427, no. 6977, pp. 821–824, Feb. 2004.

[39] S. Pramanik, C.-G. Stefanita, S. Patibandla, S. Bandyopadhyay, K. Garre, N. Harth, and M. Cahay, “Observation of extremely long spin relaxation times in an organic nanowire spin valve,” *Nat Nanotechnol*, vol. 2, no. 4, pp. 216–219, Apr. 2007.

[40] R. Meservey and P. M. Tedrow, “Spin-polarized electron tunneling,” *Physics Reports*, vol. 238, no. 4, pp. 173–243, Mar. 1994.

[41] A. J. Drew, J. Hoppler, L. Schulz, F. L. Pratt, P. Desai, P. Shakya, T. Kreouzis, W. P. Gillin, A. Suter, N. A. Morley, V. K. Malik, A. Dubroka, K. W. Kim, H. Bouyanfif, F. Bourqui, C. Bernhard, R. Scheuermann, G. J. Nieuwenhuys, T. Prokscha, and E. Morenzoni, “Direct measurement of the electronic spin diffusion length in a fully functional organic spin valve by low-energy muon spin rotation,” *Nature Materials*, vol. 8, no. 2, pp. 109–114, 2009.

[42] M. Cinchetti, K. Heimer, J.-P. Wüstenberg, O. Andreyev, M. Bauer, S. Lach, C. Ziegler, Y. Gao, and M. Aeschlimann, “Determination of spin injection and transport in a ferromagnet/organic semiconductor heterojunction by two-photon photoemission,” *Nature Materials*, vol. 8, no. 2, pp. 115–119, 2009.

[43] S. R. Forrest, “The path to ubiquitous and low-cost organic electronic appliances on plastic,” *Nature*, vol. 428, no. 6986, pp. 911–918, Apr. 2004.

[44] P. Peumans, S. Uchida, and S. R. Forrest, “Efficient bulk heterojunction photovoltaic cells using small-molecular-weight organic thin films,” *Nature*, vol. 425, no. 6954, pp. 158–162, Sep. 2003.

[45] D. J. Gundlach, Y. Y. Lin, T. N. Jackson, S. F. Nelson, and D. G. Schlom, “Pentacene organic thin-film transistors-molecular ordering and mobility,” *IEEE Electron Device Letters*, vol. 18, no. 3, pp. 87 –89, Mar. 1997.

[46] J. Boyd, “Flash memory built on bendy plastic (News: Flexible flash),” *IEEE Spectrum*, vol. 47, 2010.

[47] S. Sanvito, “Organic electronics: Spintronics goes plastic,” *Nature Materials*, vol. 6, no. 11, pp. 803–804, 2007.

[48] S. Sanvito, “Injecting and controlling spins in organic materials,” *J. Mater. Chem.*, vol. 17, no. 42, pp. 4455–4459, Oct. 2007.

[49] W. J. M. Naber, S. Faez, and W. G. van der Wiel, “Organic spintronics,” *Journal of Physics D: Applied Physics*, vol. 40, no. 12, pp. R205–R228, Jun. 2007.

[50] B. Göhler, V. Hamelbeck, T. Z. Markus, M. Kettner, G. F. Hanne, Z. Vager, R. Naaman, and H. Zacharias, “Spin Selectivity in Electron Transmission Through Self-Assembled Monolayers of Double-Stranded DNA,” *Science*, vol. 331, no. 6019, pp. 894–897, Feb. 2011.

[51] Z. Xie, Z. Xie, T. Z. Markus, S. R. Cohen, Z. Vager, R. Gutierrez, and R. Naaman, “Spin specific electron conduction through DNA oligomers,” *Nano Lett.*, vol. 11, no. 11, pp. 4652–4655, Nov. 2011.

[52] G. S. Diniz, A. Latgé, and S. E. Ulloa, “Helicoidal Fields and Spin Polarized Currents in Carbon Nanotube–DNA Hybrids,” *Phys. Rev. Lett.*, vol. 108, no. 12, p. 126601, Mar. 2012.

[53] K. M. Alam, A. P. Singh, S. C. Bodepudi, and S. Pramanik, “Fabrication of hexagonally ordered nanopores in anodic alumina: An alternative pretreatment,” *Surface Science*, vol. 605, no. 3–4, pp. 441–449, Feb. 2011.

[54] K. M. Alam, A. P. Singh, R. Starko-Bowes, S. C. Bodepudi, and S. Pramanik, “Template-Assisted Synthesis of π-Conjugated Molecular Organic Nanowires in the Sub-100 nm Regime and Device Implications,” *Advanced Functional Materials*, vol. 22, no. 15, pp. 3298–3306, 2012.

[55] K. M. Alam, S. C. Bodepudi, R. Starko-Bowes, and S. Pramanik, “Suppression of spin relaxation in rubrene nanowire spin valves,” *Applied Physics Letters*, vol. 101, no. 19, pp. 192403–192403–5, Nov. 2012.

[56] S. Forrest, P. Burrows, and M. Thompson, “The dawn of organic electronics,” *IEEE Spectr.*, vol. 37, no. 8, pp. 29–34, Aug. 2000.

[57] G. Chidichimo and L. Filippelli, “Organic Solar Cells: Problems and Perspectives,” *International Journal of Photoenergy*, vol. 2010, pp. 1–11, 2010.

[58] S. Günes, H. Neugebauer, and N. S. Sariciftci, “Conjugated Polymer-Based Organic Solar Cells,” *Chem. Rev.*, vol. 107, no. 4, pp. 1324–1338, Apr. 2007.

[59] J. E. Slota, X. He, and W. T. S. Huck, “Controlling nanoscale morphology in polymer photovoltaic devices,” *Nano Today*, vol. 5, no. 3, pp. 231–242, Jun. 2010.

[60] M. D. Kelzenberg, D. B. Turner-Evans, M. C. Putnam, S. W. Boettcher, R. M. Briggs, J. Y. Baek, N. S. Lewis, and H. A. Atwater, “High-performance Si microwire photovoltaics,” *Energy Environ. Sci.*, vol. 4, no. 3, pp. 866–871, Mar. 2011.

[61] Mukti Aryal, Fatih Buyukserin, Kamil Mielczarek, Xiao-Mei Zhao, Jinming Gao, Anvar Zakhidov, and Wenchuang (Walter) Hu, “Imprinted large-scale high density polymer nanopillars for organic solar cells,” *J. Vac. Sci. Technol. B*, vol. 26, no. 6, p. 2562, 2008.

[62] N. Haberkorn, J. S. Gutmann, and P. Theato, “Template-Assisted Fabrication of Free-Standing Nanorod Arrays of a Hole-Conducting Cross-Linked Triphenylamine Derivative: Toward Ordered Bulk-Heterojunction Solar Cells,” *ACS Nano*, vol. 3, no. 6, pp. 1415–1422, Jun. 2009.

[63] J. L. Duvail, Y. Long, S. Cuenot, Z. Chen, and C. Gu, “Tuning electrical properties of conjugated polymer nanowires with the diameter,” *Applied Physics Letters*, vol. 90, no. 10, pp. 102114–102114–3, Mar. 2007.

[64] A. L. Briseno, S. C. B. Mannsfeld, S. A. Jenekhe, Z. Bao, and Y. Xia, “Introducing organic nanowire transistors,” *Materials Today*, vol. 11, no. 4, pp. 38–47, Apr. 2008.

[65] V. A. Dediu, L. E. Hueso, I. Bergenti, and C. Taliani, “Spin routes in organic semiconductors,” *Nature Materials*, vol. 8, no. 9, pp. 707–716, 2009.

[66] B. Kanchibotla, S. Pramanik, S. Bandyopadhyay, and M. Cahay, “Transverse spin relaxation time in organic molecules,” *Phys. Rev. B*, vol. 78, no. 19, p. 193306, Nov. 2008.

[67] T. D. Nguyen, G. Hukic-Markosian, F. Wang, L. Wojcik, X.-G. Li, E. Ehrenfreund, and Z. V. Vardeny, “Isotope effect in spin response of π-conjugated polymer films and devices,” *Nature Materials*, vol. 9, no. 4, pp. 345–352, 2010.

[68] Z. G. Yu, “Spin-Orbit Coupling, Spin Relaxation, and Spin Diffusion in Organic Solids,” *Phys. Rev. Lett.*, vol. 106, no. 10, p. 106602, Mar. 2011.

[69] Z. G. Yu, “Spin-orbit coupling and its effects in organic solids,” *Phys. Rev. B*, vol. 85, no. 11, p. 115201, Mar. 2012.

[70] L. Das, J. Mateo, S. Bandyopadhyay, S. Bandyopadhyay, J. D. Edwards, and J. Anderson, “Motional modes in bulk powder and few-molecule clusters of tris(8-hydroxyquinoline

aluminum) and their relation to spin dephasing," *Applied Physics Letters*, vol. 98, no. 6, pp. 063109–063109–3, Feb. 2011.

[71] K. M. Alam and S. Pramanik, "High-field magnetoresistance in nanowire organic spin valves," *Phys. Rev. B*, vol. 83, no. 24, p. 245206, Jun. 2011.

[72] F. S. Kim, G. Ren, and S. A. Jenekhe, "One-Dimensional Nanostructures of π-Conjugated Molecular Systems: Assembly, Properties, and Applications from Photovoltaics, Sensors, and Nanophotonics to Nanoelectronics†," *Chem. Mater.*, vol. 23, no. 3, pp. 682–732, Feb. 2011.

[73] B. Kanchibotla, S. Pramanik, and S. Bandyopadhyay, "Self assembly of nanostructures using nanoporous alumina templates," in *Nano and Molecular Electronics Handbook*, Boca Raton, Florida, USA: CRC Press, 2007, pp. 9–1.

[74] K. Kim and J.-I. Jin, "Preparation of PPV Nanotubes and Nanorods and Carbonized Products Derived Therefrom," *Nano Lett.*, vol. 1, no. 11, pp. 631–636, Nov. 2001.

[75] J. Joo, B. H. Kim, D. H. Park, H. S. Kim, D. S. Seo, J. H. Shim, S. J. Lee, K. S. Ryu, K. Kim, J.-I. Jin, T. J. Lee, and C. J. Lee, "Fabrication and Applications of Conducting Polymer Nanotube, Nanowire, Nanohole, and Double Wall Nanotube," *Synthetic Metals*, vol. 153, no. 1–3, pp. 313–316, Sep. 2005.

[76] Y. Berdichevsky and Y.-H. Lo, "Polypyrrole Nanowire Actuators," *Advanced Materials*, vol. 18, no. 1, pp. 122–125, 2006.

[77] L. Zhang, F. Meng, Y. Chen, J. Liu, Y. Sun, T. Luo, M. Li, and J. Liu, "A novel ammonia sensor based on high density, small diameter polypyrrole nanowire arrays," *Sensors and Actuators B: Chemical*, vol. 142, no. 1, pp. 204–209, Oct. 2009.

[78] S. I. Cho, W. J. Kwon, S.-J. Choi, P. Kim, S.-A. Park, J. Kim, S. J. Son, R. Xiao, S.-H. Kim, and S. B. Lee, "Nanotube-Based Ultrafast Electrochromic Display," *Advanced Materials*, vol. 17, no. 2, pp. 171–175, 2005.

[79] D. O'Carroll, I. Lieberwirth, and G. Redmond, "Microcavity effects and optically pumped lasing in single conjugated polymer nanowires," *Nature Nanotechnology*, vol. 2, no. 3, pp. 180–184, Feb. 2007.

[80] D. O'Carroll, D. Iacopino, A. O'Riordan, P. Lovera, É. O'Connor, G. A. O'Brien, and G. Redmond, "Poly(9,9-dioctylfluorene) Nanowires with Pronounced β-Phase Morphology: Synthesis, Characterization, and Optical Properties," *Advanced Materials*, vol. 20, no. 1, pp. 42–48, 2008.

[81] D. O' Carroll, J. Irwin, D. A. Tanner, and G. Redmond, "Polyfluorene nanowires with pronounced axial texturing prepared by melt-assisted template wetting," *Materials Science and Engineering: B*, vol. 147, no. 2–3, pp. 298–302, Feb. 2008.

[82] G. A. O'Brien, A. J. Quinn, D. A. Tanner, and G. Redmond, "A Single Polymer Nanowire Photodetector," *Advanced Materials*, vol. 18, no. 18, pp. 2379–2383, 2006.

[83] S. Moynihan, D. Iacopino, D. O'Carroll, P. Lovera, and G. Redmond, "Template Synthesis of Highly Oriented Polyfluorene Nanotube Arrays†," *Chem. Mater.*, vol. 20, no. 3, pp. 996–1003, Feb. 2008.

[84] J. S. Kim, Y. Park, D. Y. Lee, J. H. Lee, J. H. Park, J. K. Kim, and K. Cho, "Poly(3-hexylthiophene) Nanorods with Aligned Chain Orientation for Organic Photovoltaics," *Advanced Functional Materials*, vol. 20, no. 4, pp. 540–545, 2010.

[85] K. M. Coakley, B. S. Srinivasan, J. M. Ziebarth, C. Goh, Y. Liu, and M. D. McGehee, "Enhanced Hole Mobility in Regioregular Polythiophene Infiltrated in Straight Nanopores," *Advanced Functional Materials*, vol. 15, no. 12, pp. 1927–1932, 2005.

[86] D. H. Park, B. H. Kim, M. G. Jang, K. Y. Bae, and J. Joo, “Characteristics and photoluminescence of nanotubes and nanowires of poly (3-methylthiophene),” *Applied Physics Letters*, vol. 86, no. 11, pp. 113116–113116–3, Mar. 2005.

[87] R. O. Al-Kaysi, T. H. Ghaddar, and G. Guirado, “Fabrication of One-Dimensional Organic Nanostructures Using Anodic Aluminum Oxide Templates,” *Journal of Nanomaterials*, pp. 1–14, Jan. 2009.

[88] S. Pramanik, S. Bandyopadhyay, K. Garre, and M. Cahay, “Normal and inverse spin-valve effect in organic semiconductor nanowires and the background monotonic magnetoresistance,” *Phys. Rev. B*, vol. 74, no. 23, p. 235329, Dec. 2006.

[89] J. W. Lee, K. Kim, D. H. Park, M. Y. Cho, Y. B. Lee, J. S. Jung, D.-C. Kim, J. Kim, and J. Joo, “Light-Emitting Rubrene Nanowire Arrays: A Comparison with Rubrene Single Crystals,” *Advanced Functional Materials*, vol. 19, no. 5, pp. 704–710, 2009.

[90] H. Liu, Y. Li, L. Jiang, H. Luo, S. Xiao, H. Fang, H. Li, D. Zhu, D. Yu, J. Xu, and B. Xiang, “Imaging As-Grown [60]Fullerene Nanotubes by Template Technique,” *J. Am. Chem. Soc.*, vol. 124, no. 45, pp. 13370–13371, Nov. 2002.

[91] Y. J. Xing, G. Y. Jing, J. Xu, D. P. Yu, H. B. Liu, and Y. L. Li, “Electrical conductivity of a single C60 nanotube,” *Applied Physics Letters*, vol. 87, no. 26, pp. 263117–263117–3, Dec. 2005.

[92] H. Gan, H. Liu, Y. Li, L. Gan, L. Jiang, T. Jiu, N. Wang, X. He, and D. Zhu, “Fabrication of fullerene nanotube arrays using a template technique,” *Carbon*, vol. 43, no. 1, pp. 205–208, 2005.

[93] G. D. Sulka, “Highly Ordered Anodic Porous Alumina Formation by Self-Organized Anodizing,” in *Nanostructured Materials in Electrochemistry*, A. Eftekhari, Ed. Wiley-VCH Verlag GmbH & Co. KGaA, 2008, pp. 1–116.

[94] T. R. Kline, M. Tian, J. Wang, A. Sen, M. W. H. Chan, and T. E. Mallouk, “Template-Grown Metal Nanowires,” *Inorg. Chem.*, vol. 45, no. 19, pp. 7555–7565, Sep. 2006.

[95] L. Liu, W. Zhou, S. Xie, L. Song, S. Luo, D. Liu, J. Shen, Z. Zhang, Y. Xiang, W. Ma, Y. Ren, C. Wang, and G. Wang, “Highly Efficient Direct Electrodeposition of Co−Cu Alloy Nanotubes in an Anodic Alumina Template,” *J. Phys. Chem. C*, vol. 112, no. 7, pp. 2256–2261, Feb. 2008.

[96] W. Lee, M. Alexe, K. Nielsch, and U. Gösele, “Metal Membranes with Hierarchically Organized Nanotube Arrays,” *Chem. Mater.*, vol. 17, no. 13, pp. 3325–3327, Jun. 2005.

[97] D. Losic, J. G. Shapter, J. G. Mitchell, and N. H. Voelcker, “Fabrication of gold nanorod arrays by templating from porous alumina,” *Nanotechnology*, vol. 16, no. 10, p. 2275, Oct. 2005.

[98] M. Cahay, K. Garre, J. W. Fraser, D. J. Lockwood, V. Semet, V. T. Binh, S. Bandyopadhyay, S. Pramanik, B. Kanchibotla, S. Fairchild, and L. Grazulis, “Characterization and field emission properties of lanthanum monosulfide nanoprotrusion arrays obtained by pulsed laser deposition on self-assembled nanoporous alumina templates,” *Journal of Vacuum Science & Technology B*, vol. 25, no. 2, pp. 594–603, Mar. 2007.

[99] X. Gao, L. Liu, B. Birajdar, M. Ziese, W. Lee, M. Alexe, and D. Hesse, “High-Density Periodically Ordered Magnetic Cobalt Ferrite Nanodot Arrays by Template-Assisted Pulsed Laser Deposition,” *Adv. Funct. Mater.*, vol. 19, no. 21, pp. 3450–3455, Nov. 2009.

[100] Z. H. Yuan, H. Huang, H. Y. Dang, J. E. Cao, B. H. Hu, and S. S. Fan, “Field emission property of highly ordered monodispersed carbon nanotube arrays,” *Applied Physics Letters*, vol. 78, no. 20, pp. 3127–3129, May 2001.

[101] C. Goh, K. M. Coakley, and M. D. McGehee, “Nanostructuring Titania by Embossing with Polymer Molds Made from Anodic Alumina Templates,” *Nano Lett.*, vol. 5, no. 8, pp. 1545–1549, Aug. 2005.

[102] M. Lahav, T. Sehayek, A. Vaskevich, and I. Rubinstein, “Nanoparticle Nanotubes,” *Angewandte Chemie International Edition*, vol. 42, no. 45, pp. 5576–5579, Nov. 2003.

[103] L.-F. Liu, S.-W. Lee, J.-B. Li, M. Alexe, G.-H. Rao, W.-Y. Zhou, J.-J. Lee, W. Lee, and U. Gösele, “Enhanced ionic conductivity of AgI nanowires/AAO composites fabricated by a simple approach,” *Nanotechnology*, vol. 19, no. 49, p. 495706, Dec. 2008.

[104] H. Chik, J. Liang, S. G. Cloutier, N. Kouklin, and J. M. Xu, “Periodic array of uniform ZnO nanorods by second-order self-assembly,” *Applied Physics Letters*, vol. 84, no. 17, pp. 3376–3378, Apr. 2004.

[105] H. Masuda and M. Satoh, “Fabrication of Gold Nanodot Array Using Anodic Porous Alumina as an Evaporation Mask,” *Jpn. J. Appl. Phys.*, vol. 35, no. 1B, p. L126, Jan. 1996.

[106] H. Masuda, H. Yamada, M. Satoh, H. Asoh, M. Nakao, and T. Tamamura, “Highly ordered nanochannel-array architecture in anodic alumina,” *Applied Physics Letters*, vol. 71, no. 19, pp. 2770–2772, Nov. 1997.

[107] C. Y. Liu, A. Datta, and Y. L. Wang, “Ordered anodic alumina nanochannels on focused-ion-beam-prepatterned aluminum surfaces,” *Applied Physics Letters*, vol. 78, no. 1, pp. 120–122, Jan. 2001.

[108] I. Mikulskas, S. Juodkazis, R. Tomašiūnas, and J. G. Dumas, “Aluminum Oxide Photonic Crystals Grown by a New Hybrid Method,” *Adv. Mater.*, vol. 13, no. 20, pp. 1574–1577, Oct. 2001.

[109] K. Yasui, K. Nishio, H. Nunokawa, and H. Masuda, “Ideally ordered anodic porous alumina with Sub-50nm hole intervals based on imprinting using metal molds,” *Journal of Vacuum Science & Technology B*, vol. 23, no. 4, pp. L9–L12, Jul. 2005.

[110] S. Bandyopadhyay, A. E. Miller, H. C. Chang, G. Banerjee, V. Yuzhakov, D.-F. Yue, R. E. Ricker, S. Jones, J. A. Eastman, E. Baugher, and M. Chandrasekhar, “Electrochemically assembled quasi-periodic quantum dot arrays,” *Nanotechnology*, vol. 7, no. 4, p. 360, Dec. 1996.

[111] R. E. Ricker, A. E. Miller, D.-F. Yue, G. Banerjee, and S. Bandyopadhyay, “Nanofabrication of a quantum dot array: Atomic force microscopy of electropolished aluminum,” *JEM*, vol. 25, no. 10, pp. 1585–1592, Oct. 1996.

[112] L. Ba and W. S. Li, “Influence of anodizing conditions on the ordered pore formation in anodic alumina,” *J. Phys. D: Appl. Phys.*, vol. 33, no. 20, p. 2527, Oct. 2000.

[113] W. Lee, R. Ji, U. Gösele, and K. Nielsch, “Fast fabrication of long-range ordered porous alumina membranes by hard anodization,” *Nature Materials*, vol. 5, no. 9, pp. 741–747, 2006.

[114] M. Tian, S. Xu, J. Wang, N. Kumar, E. Wertz, Q. Li, P. M. Campbell, M. H. W. Chan, and T. E. Mallouk, “Penetrating the Oxide Barrier in Situ and Separating Freestanding Porous Anodic Alumina Films in One Step,” *Nano Lett.*, vol. 5, no. 4, pp. 697–703, Apr. 2005.

[115] S. Ö. N. Taşaltin, “Simple fabrication of highly ordered AAO nanotubes,” *Journal of Optoelectronic and Biomedical Materials*, pp. 79–84, 2009.

[116] A. L. Vázquez, R. Carrera, E. Arce, N. Castillo, S. Castillo, and M. Morán-Pineda, "Preparation of mesoporous alumina films by anodization: Effect of pretreatments on the aluminum surface and MTBE catalytic oxidation," *Journal of Alloys and Compounds*, vol. 483, no. 1–2, pp. 418–421, Aug. 2009.

[117] O. Jessensky, F. Müller, and U. Gösele, "Self-Organized Formation of Hexagonal Pore Structures in Anodic Alumina," *J. Electrochem. Soc.*, vol. 145, no. 11, pp. 3735–3740, Nov. 1998.

[118] K. G. Biswas, H. El Matbouly, V. Rawat, J. L. Schroeder, and T. D. Sands, "Self-supporting nanowire arrays templated in sacrificial branched porous anodic alumina for thermoelectric devices," *Applied Physics Letters*, vol. 95, no. 7, pp. 073108–073108–3, Aug. 2009.

[119] P. Bocchetta, C. Sunseri, G. Chiavarotti, and F. Di Quarto, "Microporous alumina membranes electrochemically grown," *Electrochimica Acta*, vol. 48, no. 20–22, pp. 3175–3183, Sep. 2003.

[120] "Anodic oxidation of aluminum and its alloys," in *Information Bulletin*, vol. 14, London: The Aluminum development association, 1948.

[121] R. S. Alwitt, C. K. Dyer, and B. Noble, "Voids in Anodic Aluminum Oxide Films," *J. Electrochem. Soc.*, vol. 129, no. 4, pp. 711–717, Apr. 1982.

[122] S. Ono, M. Saito, and H. Asoh, "Self-ordering of anodic porous alumina formed in organic acid electrolytes," *Electrochimica Acta*, vol. 51, no. 5, pp. 827–833, Nov. 2005.

[123] G. J. Simpson, D. L. Sedin, and K. L. Rowlen, "Surface Roughness by Contact versus Tapping Mode Atomic Force Microscopy," *Langmuir*, vol. 15, no. 4, pp. 1429–1434, Feb. 1999.

[124] N. Almqvist, "Fractal analysis of scanning probe microscopy images," *Surface Science*, vol. 355, no. 1–3, pp. 221–228, Jun. 1996.

[125] C. H. Lui, L. Liu, K. F. Mak, G. W. Flynn, and T. F. Heinz, "Ultraflat graphene," *Nature*, vol. 462, no. 7271, pp. 339–341, Nov. 2009.

[126] B. Bhushan and M. Nosonovsky, "Scale Effect in Mechanical Properties and Tribology," in *Springer Handbook of Nanotechnology*, B. B. Prof, Ed. Springer Berlin Heidelberg, 2007, pp. 1167–1198.

[127] M. V. H. Rao, B. K. Mathur, and K. L. Chopra, "Evaluation of the scaling exponent of self-affine fractal surface from a single scanning probe microscope image," *Applied Physics Letters*, vol. 65, no. 1, pp. 124–126, Jul. 1994.

[128] L. Zhang, X. Zhang, C. Pan, and J. Zhu, "Effect of anneal pre-treatment of polycrystalline aluminum sheets on synthesis of highly-ordered anodic aluminum oxide membranes," *Sci. China Ser. E-Technol. Sci.*, vol. 51, no. 11, pp. 1838–1842, Nov. 2008.

[129] M. Gowtham, L. Eude, C. S. Cojocaru, B. Marquardt, H. J. Jeong, P. Legagneux, K. K. Song, and D. Pribat, "Controlled fabrication of patterned lateral porous alumina membranes," *Nanotechnology*, vol. 19, no. 3, p. 035303, Jan. 2008.

[130] T. L. Wade, X. Hoffer, A. D. Mohammed, J.-F. Dayen, D. Pribat, and J.-E. Wegrowe, "Nanoporous alumina wire templates for surrounding-gate nanowire transistors," *Nanotechnology*, vol. 18, no. 12, p. 125201, Mar. 2007.

[131] T. A. Beierlein, B. Ruhstaller, D. J. Gundlach, H. Riel, S. Karg, C. Rost, and W. Rieß, "Investigation of internal processes in organic light-emitting devices using thin sensing layers," *Synthetic Metals*, vol. 138, no. 1–2, pp. 213–221, Jun. 2003.

[132] J. Mei, M. S. Bradley, and V. Bulović, “Photoluminescence quenching of tris-(8-hydroxyquinoline) aluminum thin films at interfaces with metal oxide films of different conductivities,” *Phys. Rev. B*, vol. 79, no. 23, p. 235205, Jun. 2009.

[133] T. R. B. Foong, A. Sellinger, and X. Hu, “Origin of the Bottlenecks in Preparing Anodized Aluminum Oxide (AAO) Templates on ITO Glass,” *ACS Nano*, vol. 2, no. 11, pp. 2250–2256, Nov. 2008.

[134] J. J. Hill, K. Haller, and K. J. Ziegler, “Direct Fabrication of High-Aspect Ratio Anodic Aluminum Oxide with Continuous Pores on Conductive Glass,” *J. Electrochem. Soc.*, vol. 158, no. 1, pp. E1–E7, Jan. 2011.

[135] N. Taşaltın, S. Öztürk, N. Kılınç, H. Yüzer, and Z. Z. Öztürk, “Simple fabrication of hexagonally well-ordered AAO template on silicon substrate in two dimensions,” *Appl. Phys. A*, vol. 95, no. 3, pp. 781–787, Jun. 2009.

[136] K. H. Lee and C. C. Wong, “Decoupling two-step anodization in anodic aluminum oxide,” *Journal of Applied Physics*, vol. 106, no. 10, p. 104305, Nov. 2009.

[137] C. Kloc, K. J. Tan, M. L. Toh, K. K. Zhang, and Y. P. Xu, “Purity of rubrene single crystals,” *Appl. Phys. A*, vol. 95, no. 1, pp. 219–224, Apr. 2009.

[138] P. Zhang, X. Zeng, J. D. Huang, F. Bao, Y. Qiu, and K. X. Zhang, “Growth Mechanism of Large-Size Rubrene Single Crystals Grown by a Solution Technique,” *Japanese Journal of Applied Physics*, vol. 49, no. 9, p. 095501, 2010.

[139] K. K. Zhang, K. Tan, C. Zou, M. Wikberg, L. E. McNeil, S. G. Mhaisalkar, and C. Kloc, “Control of charge mobility in single-crystal rubrene through surface chemistry,” *Organic Electronics*, vol. 11, no. 12, pp. 1928–1934, Dec. 2010.

[140] K. M. Alam, S. C. Bodepudi, R. Starko-Bowes, and S. Pramanik, “High-field magnetoresistance effects and temperature-dependent spin relaxation in rubrene nanowire spin valves,” in *2013 13th IEEE Conference on Nanotechnology (IEEE-NANO)*, 2013, pp. 841–844.

[141] Z. V. Vardeny, *Organic spintronics*. Boca Raton: CRC Press/Taylor & Francis, 2010.

[142] R. Lin, F. Wang, J. Rybicki, M. Wohlgenannt, and K. A. Hutchinson, “Distinguishing between tunneling and injection regimes of ferromagnet/organic semiconductor/ferromagnet junctions,” *Phys. Rev. B*, vol. 81, no. 19, p. 195214, May 2010.

[143] J.-W. Yoo, H. W. Jang, V. N. Prigodin, C. Kao, C. B. Eom, and A. J. Epstein, “Giant magnetoresistance in ferromagnet/organic semiconductor/ferromagnet heterojunctions,” *Phys. Rev. B*, vol. 80, no. 20, p. 205207, Nov. 2009.

[144] F. Burke, P. Stamenov, and J. M. D. Coey, “Charge injection, transport and localization in rubrene,” *Synthetic Metals*, vol. 161, no. 7–8, pp. 563–569, Apr. 2011.

[145] K. V. Raman, J. Chang, and J. S. Moodera, “New method of spin injection into organic semiconductors using spin filtering tunnel barriers,” *Organic Electronics*, vol. 12, no. 7, pp. 1275–1278, Jul. 2011.

[146] H. Zeng, M. Zheng, R. Skomski, D. J. Sellmyer, Y. Liu, L. Menon, and S. Bandyopadhyay, “Magnetic properties of self-assembled Co nanowires of varying length and diameter,” *Journal of Applied Physics*, vol. 87, no. 9, pp. 4718–4720, May 2000.

[147] J. Sarkar, G. G. Khan, and A. Basumallick, “Nanowires: properties, applications and synthesis via porous anodic aluminium oxide template,” *Bull Mater Sci*, vol. 30, no. 3, pp. 271–290, Jun. 2007.

[148] S. Seo, B.-N. Park, and P. G. Evans, “Ambipolar rubrene thin film transistors,” *Applied Physics Letters*, vol. 88, no. 23, pp. 232114–232114–3, Jun. 2006.

[149] L. Gence, S. Faniel, C. Gustin, S. Melinte, V. Bayot, V. Callegari, O. Reynes, and S. Demoustier-Champagne, "Structural and electrical characterization of hybrid metal-polypyrrole nanowires," *Phys. Rev. B*, vol. 76, no. 11, p. 115415, Sep. 2007.

[150] M. Tzolov, B. Chang, A. Yin, D. Straus, J. M. Xu, and G. Brown, "Electronic Transport in a Controllably Grown Carbon Nanotube-Silicon Heterojunction Array," *Phys. Rev. Lett.*, vol. 92, no. 7, p. 075505, Feb. 2004.

[151] F. G. Monzon and M. L. Roukes, "Spin injection and the local Hall effect in InAs quantum wells," *Journal of Magnetism and Magnetic Materials*, vol. 198–199, pp. 632–635, Jun. 1999.

[152] T. Ohgai, X. Hoffer, A. Fábián, L. Gravier, and J.-P. Ansermet, "Electrochemical synthesis and magnetoresistance properties of Ni, Co and Co/Cu nanowires in a nanoporous anodic oxide layer on metallic aluminium," *J. Mater. Chem.*, vol. 13, no. 10, pp. 2530–2534, Sep. 2003.

[153] T. L. Francis, ö Mermer, G. Veeraraghavan, and M. Wohlgenannt, "Large magnetoresistance at room temperature in semiconducting polymer sandwich devices," *New Journal of Physics*, vol. 6, pp. 185–185, Dec. 2004.

[154] S. Bandyopadhyay, "Dominant spin relaxation mechanism in compound organic semiconductors," *Phys. Rev. B*, vol. 81, no. 15, p. 153202, Apr. 2010.

[155] P. A. Bobbert, W. Wagemans, F. W. A. van Oost, B. Koopmans, and M. Wohlgenannt, "Theory for Spin Diffusion in Disordered Organic Semiconductors," *Phys. Rev. Lett.*, vol. 102, no. 15, p. 156604, Apr. 2009.

[156] W. J. M. Naber, M. F. Craciun, J. H. J. Lemmens, A. H. Arkenbout, T. T. M. Palstra, A. F. Morpurgo, and W. G. van der Wiel, "Controlled tunnel-coupled ferromagnetic electrodes for spin injection in organic single-crystal transistors," *Organic Electronics*, vol. 11, no. 5, pp. 743–747, May 2010.

[157] J.-H. Park, E. Vescovo, H.-J. Kim, C. Kwon, R. Ramesh, and T. Venkatesan, "Magnetic Properties at Surface Boundary of a Half-Metallic Ferromagnet La_{0.7}Sr_{0.3}MnO_{3}," *Phys. Rev. Lett.*, vol. 81, no. 9, pp. 1953–1956, Aug. 1998.

[158] A. L. Efros and B. I. Shklovskii, "Coulomb gap and low temperature conductivity of disordered systems," *Journal of Physics C: Solid State Physics*, vol. 8, no. 4, pp. L49–L51, Feb. 1975.

[159] Dresselhaus, Mildred S, Dresselhaus, and Avouris, Phaedon, *Carbon Nanotubes - Synthesis, Structure, Properties, and Applications*, vol. 80. Springer, 2001.

[160] S. Iijima, "Helical microtubules of graphitic carbon," *Nature*, vol. 354, no. 6348, pp. 56–58, Nov. 1991.

[161] S. J. Wind, J. Appenzeller, and P. Avouris, "Lateral Scaling in Carbon-Nanotube Field-Effect Transistors," *Phys. Rev. Lett.*, vol. 91, no. 5, p. 058301, Jul. 2003.

[162] A. Javey, J. Guo, M. Paulsson, Q. Wang, D. Mann, M. Lundstrom, and H. Dai, "High-Field Quasiballistic Transport in Short Carbon Nanotubes," *Phys. Rev. Lett.*, vol. 92, no. 10, p. 106804, Mar. 2004.

[163] M. Zheng, A. Jagota, E. D. Semke, B. A. Diner, R. S. Mclean, S. R. Lustig, R. E. Richardson, and N. G. Tassi, "DNA-assisted dispersion and separation of carbon nanotubes," *Nature Materials*, vol. 2, no. 5, pp. 338–342, 2003.

[164] M. Zheng, A. Jagota, M. S. Strano, A. P. Santos, P. Barone, S. G. Chou, B. A. Diner, M. S. Dresselhaus, R. S. Mclean, G. B. Onoa, G. G. Samsonidze, E. D. Semke, M. Usrey, and

D. J. Walls, "Structure-Based Carbon Nanotube Sorting by Sequence-Dependent DNA Assembly," *Science*, vol. 302, no. 5650, pp. 1545–1548, Nov. 2003.

[165] R. S. Mclean, X. Huang, C. Khripin, A. Jagota, and M. Zheng, "Controlled Two-Dimensional Pattern of Spontaneously Aligned Carbon Nanotubes," *Nano Lett.*, vol. 6, no. 1, pp. 55–60, Jan. 2006.

[166] A. R. Hopkins, N. A. Kruk, and R. A. Lipeles, "Macroscopic alignment of single-walled carbon nanotubes (SWNTs)," *Surface and Coatings Technology*, vol. 202, no. 4–7, pp. 1282–1286, Dec. 2007.

[167] C. Y. Khripin, M. Zheng, and A. Jagota, "Deposition and meniscus alignment of DNA–CNT on a substrate," *Journal of Colloid and Interface Science*, vol. 330, no. 2, pp. 255–265, Feb. 2009.

[168] L. S.-R. Germarie Sánchez-Pomales, "DNA-functionalized carbon nanotubes for biosensing applications.," *Journal of nanoscience and nanotechnology*, vol. 9, no. 4, pp. 2175–88, 2009.

[169] S. R. Shin, C. K. Lee, I. S. So, J. H. Jeon, T. M. Kang, C. W. Kee, S. I. Kim, G. M. Spinks, G. G. Wallace, and S. J. Kim, "DNA-Wrapped Single-Walled Carbon Nanotube Hybrid Fibers for supercapacitors and Artificial Muscles," *Adv. Mater.*, vol. 20, no. 3, pp. 466–470, Feb. 2008.

[170] J. Y. Lee, H. Y. Shin, S. W. Kang, C. Park, and S. W. Kim, "Use of bioelectrode containing DNA-wrapped single-walled carbon nanotubes for enzyme-based biofuel cell," *Journal of Power Sources*, vol. 195, no. 3, pp. 750–755, Feb. 2010.

[171] S. Basuray, S. Senapati, A. Aijian, A. R. Mahon, and H.-C. Chang, "Shear and AC Field Enhanced Carbon Nanotube Impedance Assay for Rapid, Sensitive, and Mismatch-Discriminating DNA Hybridization," *ACS Nano*, vol. 3, no. 7, pp. 1823–1830, Jul. 2009.

[172] M. T. Martínez, Y.-C. Tseng, N. Ormategui, I. Loinaz, R. Eritja, and J. Bokor, "Label-Free DNA Biosensors Based on Functionalized Carbon Nanotube Field Effect Transistors," *Nano Lett.*, vol. 9, no. 2, pp. 530–536, Feb. 2009.

[173] X. Dong, D. Fu, Y. Xu, J. Wei, Y. Shi, P. Chen, and L.-J. Li, "Label-Free Electronic Detection of DNA Using Simple Double-Walled Carbon Nanotube Resistors," *J. Phys. Chem. C*, vol. 112, no. 26, pp. 9891–9895, Jul. 2008.

[174] F. Berti, L. Lozzi, I. Palchetti, S. Santucci, and G. Marrazza, "Aligned carbon nanotube thin films for DNA electrochemical sensing," *Electrochimica Acta*, vol. 54, no. 22, pp. 5035–5041, Sep. 2009.

[175] Y. Ma, P. L. Chiu, A. Serrano, S. R. Ali, A. M. Chen, and H. He, "The electronic role of DNA-functionalized carbon nanotubes: efficacy for in situ polymerization of conducting polymer nanocomposites," *J. Am. Chem. Soc.*, vol. 130, no. 25, pp. 7921–7928, Jun. 2008.

[176] S. Roy, H. Vedala, A. D. Roy, D. Kim, M. Doud, K. Mathee, H. Shin, N. Shimamoto, V. Prasad, and W. Choi, "Direct Electrical Measurements on Single-Molecule Genomic DNA Using Single-Walled Carbon Nanotubes," *Nano Lett.*, vol. 8, no. 1, pp. 26–30, Jan. 2008.

[177] S. Bandow, S. Asaka, Y. Saito, A. M. Rao, L. Grigorian, E. Richter, and P. C. Eklund, "Effect of the Growth Temperature on the Diameter Distribution and Chirality of Single-Wall Carbon Nanotubes," *Phys. Rev. Lett.*, vol. 80, no. 17, pp. 3779–3782, Apr. 1998.

[178] H. Kawamoto, T. Uchida, K. Kojima, and M. Tachibana, "G band Raman features of DNA-wrapped single-wall carbon nanotubes in aqueous solution and air," *Chemical Physics Letters*, vol. 432, no. 1–3, pp. 172–176, Dec. 2006.

[179] H. Kawamoto, T. Uchida, K. Kojima, and M. Tachibana, “The feature of the Breit-Wigner-Fano Raman line in DNA-wrapped single-wall carbon nanotubes,” *Journal of Applied Physics*, vol. 99, no. 9, p. 094309, May 2006.

[180] A. Jorio, A. G. Souza Filho, G. Dresselhaus, M. S. Dresselhaus, A. K. Swan, M. S. Ünlü, B. B. Goldberg, M. A. Pimenta, J. H. Hafner, C. M. Lieber, and R. Saito, “G-band resonant Raman study of 62 isolated single-wall carbon nanotubes,” *Phys. Rev. B*, vol. 65, no. 15, p. 155412, Mar. 2002.

[181] V. A. Karachevtsev and A. Y. Glamazda, “Raman spectroscopy of DNA-wrapped single-walled carbon nanotube films at 295 and 5K,” *Low Temperature Physics*, vol. 36, no. 5, pp. 373–381, May 2010.

[182] S. G. Chou, H. B. Ribeiro, E. B. Barros, A. P. Santos, D. Nezich, G. G. Samsonidze, C. Fantini, M. A. Pimenta, A. Jorio, F. P. Filho, M. S. Dresselhaus, G. Dresselhaus, R. Saito, M. Zheng, G. B. Onoa, E. D. Semke, A. K. Swan, M. S. Ünlü, and B. B. Goldberg, “Optical characterization of DNA-wrapped carbon nanotube hybrids,” *Chemical Physics Letters*, vol. 397, no. 4–6, pp. 296–301, Oct. 2004.

[183] Q.-H. Yang, Q. Wang, N. Gale, C. J. Oton, L. Cui, I. S. Nandhakumar, Z. Zhu, Z. Tang, T. Brown, and W. H. Loh, “Loosening the DNA wrapping around single-walled carbon nanotubes by increasing the strand length,” *Nanotechnology*, vol. 20, no. 19, p. 195603, May 2009.

[184] S. M. Bachilo, “Structure-Assigned Optical Spectra of Single-Walled Carbon Nanotubes,” *Science*, vol. 298, no. 5602, pp. 2361–2366, Dec. 2002.

[185] K. Inomata, N. Ikeda, N. Tezuka, R. Goto, S. Sugimoto, M. Wojcik, and E. Jedryka, “Highly spin-polarized materials and devices for spintronics,” *Sci. Technol. Adv. Mater.*, vol. 9, no. 1, p. 014101, Jan. 2008.

[186] V. M. Karpan, G. Giovannetti, P. A. Khomyakov, M. Talanana, A. A. Starikov, M. Zwierzycki, J. van den Brink, G. Brocks, and P. J. Kelly, “Graphite and Graphene as Perfect Spin Filters,” *Phys. Rev. Lett.*, vol. 99, no. 17, p. 176602, Oct. 2007.

[187] S. Yeganeh, M. A. Ratner, E. Medina, and V. Mujica, “Chiral electron transport: scattering through helical potentials,” *J Chem Phys*, vol. 131, no. 1, p. 014707, Jul. 2009.

[188] R. Gutierrez, E. Díaz, R. Naaman, and G. Cuniberti, “Spin-selective transport through helical molecular systems,” *Phys. Rev. B*, vol. 85, no. 8, p. 081404, Feb. 2012.

[189] A.-M. Guo and Q. Sun, “Spin-Selective Transport of Electrons in DNA Double Helix,” *Phys. Rev. Lett.*, vol. 108, no. 21, p. 218102, May 2012.

[190] A.-M. Guo and Q. Sun, “Enhanced spin-polarized transport through DNA double helix by gate voltage,” *Phys. Rev. B*, vol. 86, no. 3, p. 035424, Jul. 2012.

[191] A. Cottet, T. Kontos, S. Sahoo, H. T. Man, M.-S. Choi, W. Belzig, C. Bruder, A. F. Morpurgo, and C. Schönenberger, “Nanospintronics with carbon nanotubes,” *Semiconductor Science and Technology*, vol. 21, no. 11, pp. S78–S95, Nov. 2006.

[192] F. Kuemmeth, S. Ilani, D. C. Ralph, and P. L. McEuen, “Coupling of spin and orbital motion of electrons in carbon nanotubes,” *Nature*, vol. 452, no. 7186, pp. 448–452, Mar. 2008.

[193] J. Klinovaja, M. J. Schmidt, B. Braunecker, and D. Loss, “Helical Modes in Carbon Nanotubes Generated by Strong Electric Fields,” *Phys. Rev. Lett.*, vol. 106, no. 15, p. 156809, Apr. 2011.

[194] A. Varykhalov, J. Sánchez-Barriga, A. M. Shikin, C. Biswas, E. Vescovo, A. Rybkin, D. Marchenko, and O. Rader, "Electronic and Magnetic Properties of Quasifreestanding Graphene on Ni," *Phys. Rev. Lett.*, vol. 101, no. 15, p. 157601, Oct. 2008.

[195] D. A. Yarotski, S. V. Kilina, A. A. Talin, S. Tretiak, O. V. Prezhdo, A. V. Balatsky, and A. J. Taylor, "Scanning Tunneling Microscopy of DNA-Wrapped Carbon Nanotubes," *Nano Lett.*, vol. 9, no. 1, pp. 12–17, Jan. 2009.

[196] D. Porath, A. Bezryadin, S. de Vries, and C. Dekker, "Direct measurement of electrical transport through DNA molecules," *Nature*, vol. 403, no. 6770, pp. 635–638, Feb. 2000.

[197] A. J. Storm, J. van Noort, S. de Vries, and C. Dekker, "Insulating behavior for DNA molecules between nanoelectrodes at the 100 nm length scale," *Applied Physics Letters*, vol. 79, no. 23, pp. 3881–3883, Dec. 2001.

[198] R. G. Endres, D. L. Cox, and R. R. P. Singh, "Colloquium: The quest for high-conductance DNA," *Rev. Mod. Phys.*, vol. 76, no. 1, pp. 195–214, Jan. 2004.

[199] J. R. Heath and M. A. Ratner, "Molecular electronics," *Physics Today*, vol. 56, no. 5, pp. 43–49, May 2003.

[200] J. S. Hwang, H. T. Kim, H. K. Kim, M. H. Son, J. H. Oh, S. W. Hwang, and D. Ahn, "Electronic transport characteristics of a single wall carbon nanotube field effect transistor wrapped with deoxyribonucleic acid molecules," *J. Phys.: Conf. Ser.*, vol. 109, no. 1, p. 012015, Mar. 2008.

[201] M. Bockrath, "Single-Electron Transport in Ropes of Carbon Nanotubes," *Science*, vol. 275, no. 5308, pp. 1922–1925, Mar. 1997.

[202] M. Cha, S. Jung, M.-H. Cha, G. Kim, J. Ihm, and J. Lee, "Reversible Metal−Semiconductor Transition of ssDNA-Decorated Single-Walled Carbon Nanotubes," *Nano Lett.*, vol. 9, no. 4, pp. 1345–1349, Apr. 2009.

[203] P. Crespo, R. Litrán, T. C. Rojas, M. Multigner, J. M. de la Fuente, J. C. Sánchez-López, M. A. García, A. Hernando, S. Penadés, and A. Fernández, "Permanent Magnetism, Magnetic Anisotropy, and Hysteresis of Thiol-Capped Gold Nanoparticles," *Phys. Rev. Lett.*, vol. 93, no. 8, p. 087204, Aug. 2004.

[204] J. S. Garitaonandia, M. Insausti, E. Goikolea, M. Suzuki, J. D. Cashion, N. Kawamura, H. Ohsawa, I. Gil de Muro, K. Suzuki, F. Plazaola, and T. Rojo, "Chemically Induced Permanent Magnetism in Au, Ag, and Cu Nanoparticles: Localization of the Magnetism by Element Selective Techniques," *Nano Lett.*, vol. 8, no. 2, pp. 661–667, Feb. 2008.

[205] T. Taniyama, E. Wada, M. Itoh, and M. Yamaguchi, "Electrical and optical spin injection in ferromagnet/semiconductor heterostructures," *NPG Asia Materials*, vol. 3, no. 7, pp. 65–73, 2011.

[206] K. Inomata, N. Ikeda, N. Tezuka, R. Goto, S. Sugimoto, M. Wojcik, and E. Jedryka, "Highly spin-polarized materials and devices for spintronics," *Science and Technology of Advanced Materials*, vol. 9, no. 1, p. 014101, Mar. 2008.

[207] S. Yeganeh, M. A. Ratner, E. Medina, and V. Mujica, "Chiral electron transport: Scattering through helical potentials," *The Journal of Chemical Physics*, vol. 131, no. 1, pp. 014707–014707–9, Jul. 2009.

[208] E. Medina, F. López, M. A. Ratner, and V. Mujica, "Chiral molecular films as electron polarizers and polarization modulators," *EPL (Europhysics Letters)*, vol. 99, no. 1, p. 17006, Jul. 2012.

[209] T. Aqua, R. Naaman, and S. S. Daube, "Controlling the Adsorption and Reactivity of DNA on Gold," *Langmuir*, vol. 19, no. 25, pp. 10573–10580, Dec. 2003.

[210] K. Tsukagoshi, B. W. Alphenaar, and H. Ago, “Coherent transport of electron spin in a ferromagnetically contacted carbon nanotube,” *Nature*, vol. 401, no. 6753, pp. 572–574, Oct. 1999.

[211] S. Sahoo, T. Kontos, J. Furer, C. Hoffmann, M. Gräber, A. Cottet, and C. Schönenberger, “Electric field control of spin transport,” *Nature Physics*, vol. 1, no. 2, pp. 99–102, 2005.

[212] L. E. Hueso, J. M. Pruneda, V. Ferrari, G. Burnell, J. P. Valdés-Herrera, B. D. Simons, P. B. Littlewood, E. Artacho, A. Fert, and N. D. Mathur, “Transformation of spin information into large electrical signals using carbon nanotubes,” *Nature*, vol. 445, no. 7126, pp. 410–413, Jan. 2007.

[213] H. Yang, M. E. Itkis, R. Moriya, C. Rettner, J.-S. Jeong, D. S. Pickard, R. C. Haddon, and S. S. P. Parkin, “Nonlocal spin transport in single-walled carbon nanotube networks,” *Phys. Rev. B*, vol. 85, no. 5, p. 052401, Feb. 2012.